

Computer simulations of the structure and dynamics of elongated colloidal particles

Citation for published version (APA):

Oshima Menegon, M. (2019). *Computer simulations of the structure and dynamics of elongated colloidal particles*. [Phd Thesis 1 (Research TU/e / Graduation TU/e), Applied Physics and Science Education]. Technische Universiteit Eindhoven.

Document status and date:

Published: 13/11/2019

Document Version:

Publisher's PDF, also known as Version of Record (includes final page, issue and volume numbers)

Please check the document version of this publication:

- A submitted manuscript is the version of the article upon submission and before peer-review. There can be important differences between the submitted version and the official published version of record. People interested in the research are advised to contact the author for the final version of the publication, or visit the DOI to the publisher's website.
- The final author version and the galley proof are versions of the publication after peer review.
- The final published version features the final layout of the paper including the volume, issue and page numbers.

[Link to publication](#)

General rights

Copyright and moral rights for the publications made accessible in the public portal are retained by the authors and/or other copyright owners and it is a condition of accessing publications that users recognise and abide by the legal requirements associated with these rights.

- Users may download and print one copy of any publication from the public portal for the purpose of private study or research.
- You may not further distribute the material or use it for any profit-making activity or commercial gain
- You may freely distribute the URL identifying the publication in the public portal.

If the publication is distributed under the terms of Article 25fa of the Dutch Copyright Act, indicated by the "Taverne" license above, please follow below link for the End User Agreement:

www.tue.nl/taverne

Take down policy

If you believe that this document breaches copyright please contact us at:

openaccess@tue.nl

providing details and we will investigate your claim.

Computer simulations of the structure and dynamics of elongated colloidal particles

Mariana Oshima Menegon

Computer simulations of the structure and dynamics of elongated colloidal particles

Mariana Oshima Menegon

A catalogue record is available from the Eindhoven
University of Technology Library

ISBN **978-90-386-4871-2**

Cover design by **Mariana Oshima Menegon**
Printed by **Ipskamp Printing**



This project has received funding from the European Union's
Horizon 2020 research and innovation programme under the
Marie Skłodowska-Curie Grant Agreement No 641839.

Computer simulations of the structure and dynamics of elongated colloidal particles

PROEFSCHRIFT

ter verkrijging van de graad van doctor aan de Technische Universiteit Eindhoven, op gezag van de rector magnificus prof.dr.ir. F.P.T. Baaijens, voor een commissie aangewezen door het College voor Promoties, in het openbaar te verdedigen op woensdag 13 november 2019 om 16:00 uur

door

Mariana Oshima Menegon

geboren te São Paulo, Brazilië

Dit proefschrift is goedgekeurd door de promotoren en de samenstelling van de promotiecommissie is als volgt:

voorzitter	prof.dr.ir. G.M.W Kroesen
promotoren	prof.dr.ir. P.P.A.M. van der Schoot prof.dr. C. Storm
leden	prof.dr.ir. R. Tuinier prof.dr.ir. M. Dijkstra (Utrecht University) Dr. E. Grelet (Centre National de la Recherche Scientifique)

Het onderzoek of ontwerp dat in dit proefschrift wordt beschreven is uitgevoerd in overeenstemming met de TU/e Gedragscode Wetenschapsbeoefening.

Summary

Our aim is to investigate, by means of molecular dynamics computer simulation, the structural and dynamical properties of elongated colloidal particles in dense dispersions. Colloidal particles are present in many industrial processes and almost everywhere in our everyday life, as they may be found in paints, cosmetics, and food. In particular, the interest in elongated colloidal particles has recently increased due to applications in high-performance materials, such as strong fibres and responsive films, and as a result of the development of well-defined experimental model particles, such as filamentous virus particles. At sufficiently high concentrations, elongated particles form a plethora of liquid-crystalline phases in between the well-known isotropic fluid and crystalline phases. The self-organisation into these symmetry-broken phases is primarily driven by excluded-volume interactions (entropy). Due to their anisotropy, particles tend to align along a preferential direction and give up a maximum of two positional degrees of freedom to optimise the volume accessible to each particle.

Several filamentous and rod-like viruses have shown to exhibit in aqueous solution a uniaxial nematic, a layered smectic A, a smectic B with in-layer quasi long-range hexatic order, and a columnar liquid-crystalline phase. The phase sequence of filamentous viruses encountered with increasing concentration is different from that predicted for a system of infinitely stiff, hard spherocylinders, which do not support the smectic B and columnar phases. The existence of these phases has been speculated to be due to the bending flexibility of the particles. In our research we investigate how flexibility affects the stability and the structure of the liquid-crystalline phases of elongated colloidal particles. Using coarse-grained bead-spring models, we find that the stability of the smectic A and B phases depends crucially on the bending flexibility of the particles, and on their aspect ratio. The smectic A phase becomes less stable and the smectic B phase more stable with increasing particle bending flexibility. The former finding had been predicted theoretically, the latter is a novel insight.

Even if harshly repulsive interactions are thought to dominate in stable dispersion of rod-like particles, weakly attractive interactions may still have a large effect on the stability of liquid-crystalline phases. We investigate this in collab-

oration with an experimental research group at Centre de Recherche Paul Pascal (CRPP) in Bordeaux, France. The group engineered a single type of protein on one of the two tips of a filamentous virus, allowing them to graft a controlled number of fluorescent dye molecules and create particles with a polar interaction. As the dyes are hydrophobic, this results in a controllable, attractive, single-ended and highly localised interaction between the particles. The surface modification was found to stabilise the smectic A phase at lower concentrations, at the expense of the nematic phase, while not affecting any of the other phases. For this reason we investigate how a weakly attractive tip has such a strong impact upon the phase behaviour of elongated colloidal particles. Our computer simulations show that the sticky ends drive the formation of flat, membrane-like aggregates that destabilise the nematic phase in favour of the smectic A phase. We also discover a transition to an anti-ferroelectric phase that destroys the nematic at sufficiently large but still rather modest sticking energies. Our findings may contribute to the rational design of self-assembled structures, for example, for battery applications.

Dispersions of elongated colloidal particles not only have remarkable structural properties, diffusion of such particles has also interesting and sometimes counterintuitive features, depending on the underlying symmetry of the phase. For example, experiments at CRPP in Bordeaux and simulations show that in the smectic A phase the particles engage mostly in a layer-to-layer, hopping-type diffusion that is strongly affected by their bending flexibility and aspect ratio. In our work, we investigate how the anisotropy and flexibility of elongated tracer particles affect their diffusion in a smectic A host phase. Simulations and experiments show that guest particles that are longer than the host particles diffuse faster in the host smectic A phase than the host particles do. Our simulations show that also shorter particles diffuse faster than the guest particles. The bending flexibility of guest particles, in this case, does not seem to play an important rôle. Our simulations may help to elucidate the transport mechanisms of macromolecules through cellular or other biological membranes, which is of interest to cell biology as well as drug delivery applications.

Finally, in order to make headway in the field of dynamical percolation, relevant in the context of carbon nanotube nanocomposites, we initiate the first study of the dynamics of geometric percolation of hard particles, taking as starting point spheres rather than tubes for reasons of simplicity. The question we specifically address, is whether geometric percolation exhibits critical slowing down because of the critical nature of the percolation transition. We find that the connectivity length and concentration both impact on the survival dynamics of pre-critical clusters. Surprisingly, we do not observe any critical slowing down upon approach of the percolation transition.

Contents

Summary	i
1 Introduction	1
1.1 Elongated colloidal particles	2
1.2 Motivation and research questions	4
1.3 Outline of the thesis	7
2 Our approach	9
2.1 Computer simulations	10
2.2 Model particles	11
2.3 Phase behaviour and microstructure	13
2.4 Diffusion	16
3 Self-organisation of semi-flexible elongated particles	19
3.1 Introduction	20
3.2 Methods and analysis	21
3.3 Phase behaviour	26
3.4 Microstructure	29
3.5 Discussion and conclusions	33
3.A Onsager theory of linearly compressible hard rods	34
4 Self-organisation of tip-functionalised elongated particles	39
4.1 Introduction	40
4.2 Methods and analysis	41
4.3 Phase behaviour	46
4.4 Microstructure	50
4.5 Comparison with experiments	61
4.6 Discussion and conclusions	67
4.A The anti-ferroelectric phase transition within a Maier-Saupe-McMillan type theory	68

5	Dynamics of elongated guest particles in the smectic A phase	75
5.1	Introduction	76
5.2	Methods and Analysis	77
5.3	Characterisation of the dynamics	84
5.4	Hopping-type diffusion	87
5.5	Deflection length	94
5.6	Discussion and conclusions	96
6	Dynamics of clusters and percolation in the isotropic phase	99
6.1	Introduction	100
6.2	Methods and analysis	102
6.3	Percolation threshold	104
6.4	Cluster dynamics	106
6.5	Discussion and conclusions	113
6.A	Estimate of the cluster renewal time	116
7	Conclusion	119
7.1	Aim of the thesis	120
7.2	Summary and conclusions	120
7.3	Outlook	123
	Bibliography	125
	Acknowledgments	iii
	Curriculum Vitae	iv
	Publication list	v

Chapter 1

Introduction

The thesis describes results of computer simulation studies concerning the structural and dynamical properties of elongated colloidal particles in suspension. Colloidal particles are present in many industrial processes and almost everywhere in our everyday life, as they may be found in paints, cosmetics, and food. Furthermore, the interest in elongated colloidal particles has recently increased due to applications in high-performance materials and due to the development of well-controlled experimental model particles. At sufficiently high concentrations, such particles may exhibit various liquid-crystalline phases in which one or more degrees of freedom of these particles are frozen in. In this chapter, we provide more details about our work, the aim of which is to investigate the self-organisation of rodlike colloidal particles. In particular, we are interested in how this is affected by the particles' properties and interactions. We present the context and pose specific questions that motivate our research. Based on that, we also provide the outline for the thesis.

1.1 Elongated colloidal particles

Our studies focus on computer simulations of the structure and dynamics of elongated colloidal particles in suspension. These particles are not only present all around but also inside of us. Examples range from inorganic particles (such as silica rods [1]), through filamentous viruses (tobacco mosaic virus [2]), to biological fibres (actin filaments [3]). At the macroscopic level, suspensions of such particles may show complex optical properties such as birefringence and iridescence that are of interest to industry for the fabrication of optical devices such as polarisers and gratings [4, 5]. Elongated colloidal particles may also show superior mechanical properties. For this reason, they have been applied in the production of strong fibres and other high-performance materials [4, 6]. They have also been explored in the synthesis of functional materials such as nanowires and batteries [7–10], and in the investigation of the self-assembly of specific structures such as multipods and tubes [11–13]. As these particles might be directly visualised using optical microscopy techniques, they are employed as model systems of atoms and molecules in the investigation of phase transitions [14]. In this section, we illuminate what elongated colloidal particles are from the point of view of physics. For this purpose, we introduce some features of colloidal particles as well as of the symmetry-broken configurations formed by these anisotropic particles in fluid dispersions.

A suspensions of colloidal particles form a highly heterogeneous liquid-solid or liquid-liquid mixture. Colloidal particles are in the size range from about 10 nm to 1 μm [15]. Therefore, they are sufficiently small to have their movement influenced by the many collisions with the molecules constituting the dispersion medium. The time scale of the movement of solvent molecules is fast compared to the time scale of the colloidal particles. For this reason, as well as for the large difference in the length scales involved, the movement of the colloidal particles is governed by Brownian dynamics, which is well described by irreversible Langevin equations [16]. The description is simplified because the degrees of freedom of the molecules forming the dispersion medium are replaced by a friction and a random force that mimic their overall effect [16]. In addition to these forces, the motion of colloidal particles is also described in terms the effective interactions between them. A very important one is the *excluded volume* interaction, which can be understood as the unaccessible volume to a particle due to the presence of another particle. A hard-core potential, which is zero for non-overlapping particles and infinity for overlapping ones, is usually used to describe a system in which excluded-volume interactions dominate. In this case, the Boltzmann weight of the configurations is independent of the temperature. As a consequence, there is no energy scale associated to a system of hard par-

ticles. Such a system is then *athermal* and, as a consequence, entropy alone is sufficient to describe its thermodynamic state [17].

In addition to that, if these colloidal particles are elongated, as their concentration increases, they may form additional phases in between the well-known (disordered) isotropic and (ordered) crystalline phases. In these phases, known as *liquid-crystalline phases*¹, the particles have a preferential orientation, which is described by the unit vector $\hat{\mathbf{n}}$, known as the *director*. The particles also have short- or quasi long-range translational order. For example, in the *nematic* phase, particles have liquid-like, short-range translational order. In the *smectic* phase, particles are organised in layers along the director (one-dimensional quasi long-range order) with a well defined *interlayer distance* (or *layer spacing*). There are many types of smectic phase, depending on the particles' configuration and organisation in the layers. For example, particles aligned perpendicularly to the layers are disordered in the smectic A phase, while they exhibit in addition quasi long-range bond-orientational order and short-range translational order also known as *hexatic* order in the layers of the smectic B phase. It is also possible that the particles are tilted in relation to the layer, as it is the case in the smectic C phase. There are many more smectic phases of which the total number cannot be specified [18]. The smectic and nematic phase can also exhibit *chirality* if containing chiral particles or dopants. In the *columnar* phase, particles are organised in the plane perpendicular to the director (quasi long-range bond-orientational order), while there is no order along the direction parallel to the director. There are two types of columnar phase depending if the two-dimensional translational order is long-range (hexagonal) or short-range (hexatic). See Figure 1.1.

In 1949, Lars Onsager provided the first theoretical, purely entropic explanation for the isotropic-to-nematic phase transition [19]. The theory is based on the second virial approximation, which means that it includes only the interaction between pairs of particle. These are represented by hard cylinders of diameter D and length L . In this case, their excluded volume is equal to $2DL^2|\sin \gamma|$ at least if they are slender and $L \gg D$, where γ is the angle between the main axes of the particles. In the nematic phase, in order to optimise the volume accessible to each particle (reduce the excluded volume), the particles tend to align along the director. In other words, the orientational entropy is reduced in order to increase the translational entropy. The isotropic-to-nematic phase transition is said to be of the *first order*, as these phases may coexist under appropriate conditions.

¹Liquid crystals of elongated colloidal particles belong to the class of *lyotropic* liquid crystals. The concentration is the relevant thermodynamic quantity in determining their state. There are also the *thermotropic* liquid crystals, usually a single component fluid composed of low molecular weight elongated or flat particles. In this case, the temperature is the relevant thermodynamic property [4].

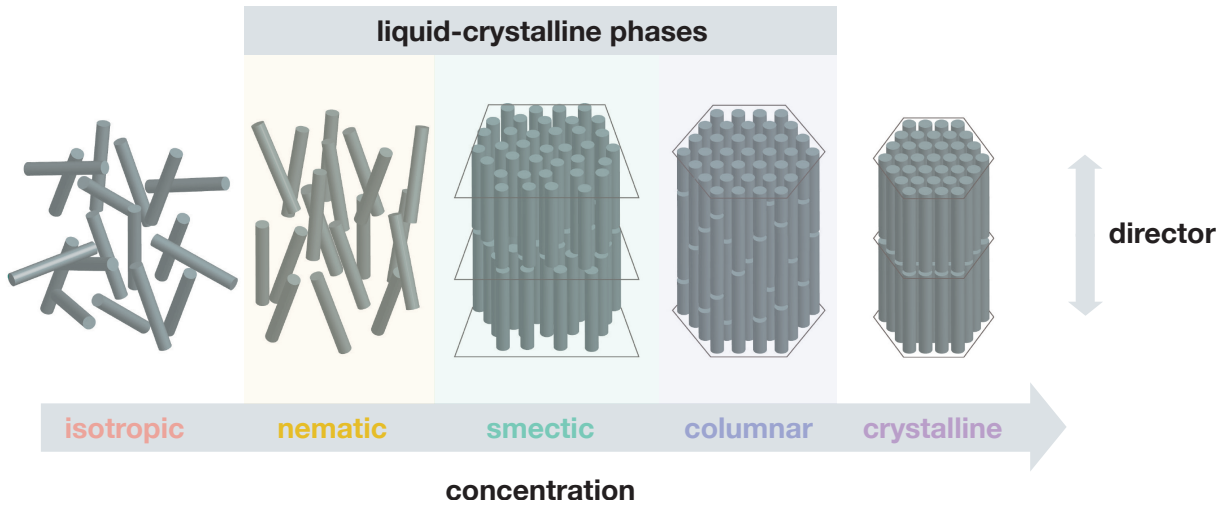


Figure 1.1: Schematic illustration of the phases of elongated particles (pictured as hard cylinders). Between the isotropic and crystalline phases, from left to right, the liquid crystalline nematic, smectic, and columnar phases are represented. The director gives the preferential orientation of the particles.

Since then, experiments, simulations, and theory have shown that the excluded-volume interaction alone is sufficient to explain the formation of the phases described above as well as other possible mesophases [20–28]. Nevertheless, there are many more nuances and possibilities to be explored, as these colloidal particles might have different sizes, shapes, or localised *patchy* interactions. Real particles always present some of these properties at some degree, which are not captured by the hard cylinder model. We explore a number of them using computer simulations. In the next section, we introduce some more specific findings related to the structure and dynamics of elongated colloidal particles that instigated questions and inspired our present work.

1.2 Motivation and research questions

Our studies are inspired by experiments performed on the filamentous bacteriophages M13 and fd, either wild type (wt) or mutants [29, 30]. They are highly monodispersed model particles of 7 nm in diameter and about 1 μm in length. In Table 1.1, these values are specified for different types of filamentous viruses. Their persistence length is large and can be modified by genetic modifications of their DNA. In polymer physics, the persistence length L_p is a measure of the bending flexibility or stiffness of a polymer chain. It is defined through the correlation between the tangent vector $\hat{\mathbf{t}}(l)$ along the contour of the chain described by the contour distance l . It obeys the relation $\langle \hat{\mathbf{t}}(l) \cdot \hat{\mathbf{t}}(l') \rangle = e^{-|l-l'|/L_p}$, where the an-

gular brackets represent the average over all configurations and e is the Euler’s constant. Due to the large persistence length and monodispersity, filamentous viruses are a good model system of hard rods and support the isotropic, chiral nematic, smectic A, smectic B, columnar and crystalline phases in aqueous solutions [27]. Hence, they exhibit the liquid-crystalline smectic B and columnar phases in addition to the phases formed by a system of hard spherocylinders [25]. It is possible that the bending flexibility of the elongated particles or the combination of this and the aspect ratio are the important elements for the formation of these phases. As a matter of fact, the stability of the columnar phase is probably linked to this combination as indicated by a recent experiment [28] and suggested theoretically [31]. This is one example that shows how important the role of particles anisotropy and bending flexibility is to the existence and stability range of any liquid-crystalline phase. Actually, the first question of *how the aspect ratio and flexibility changes the stability and structure of the liquid-crystalline phases* has been explored in experiments [26–28, 32, 33], simulations [34–40], and theory [20–23]. However, the topic is not exhaustively investigated and our contribution is to expand on the range of bending flexibilities and aspect ratios investigated previously in computer simulations. Importantly, we investigate the complete phase sequences employing the same simulation approach for all phases.

	D [nm]	L [μm]	L_p [nm]
fd-wt	6.6	0.88	2.8 ± 0.7
fdY21M	7	0.91	9.9 ± 1.6
M13K07	7	1.2	2.8

Table 1.1: Particle characteristics of the M13 and fd viruses (and mutants). The diameter D , contour length L , and persistence length L_p are presented for the fd-wt virus [30] and the fdY21M [30, 41] and M13K07 mutants [41].

Even if excluded volume interactions dominate, weak and highly local interactions may also have a large effect on liquid-crystalline phases. This is the main finding of our second study, which is inspired by experiments performed by our collaborators from the *Centre de Recherche Paul Pascal* (CRPP) in Bordeaux, France [42]. In their experiments, the filamentous M13 virus has its terminal (P3) protein modified, allowing the attachment of red dye molecules to one of the two tips of the virus particle. The procedure results in a controllable, attractive, single-end localised interaction. Such surface modification stabilises the smectic A phase at much lower concentrations, leading to our second research question: *what is the effect of a weakly attractive tip on the phase behaviour of elongated colloidal particles?* The stabilisation of the smectic A phase that we find in both

experiments and simulations might be of interest to industrial and scientific applications due to its optical and mechanical properties [43, 44]. In particular, to have it formed at lower concentrations might facilitate processing and reduce the use of material. Our results may also contribute to the rational design of self-assembled structures [45, 46].

Our first two studies show that elongated colloidal particles have singular structural properties. Nevertheless, the diffusion of elongated particles also has interesting and sometimes counterintuitive features [38, 47–49]. The long-time diffusion of the particles is different in each phase due to translation-rotation coupling and the broken symmetry. An example is the fast diffusion along the main axis in the nematic phase as compared to that of the isotropic phase, and another one the hopping-type diffusion found in both the smectic phase as well as in the columnar phase. In the smectic phase, the hops correspond to the layer size which are approximately equal to the particle contour length [49]. This is due to the molecular field created by the surrounding particles or *smectic ordering potential* whose minima correspond to the centres of the smectic layers. In the columnar phase, the hops correspond to both half and full particle contour length. These two types of particle motions may indicate events in which particles re-equilibrate after another particle leaves the column and in which particles swap positions in the same column [38, 48].

In our work, we are also interested in diffusion of particles in the smectic phase. In particular, in the diffusion of short and long guest particles in the smectic A phase formed by host particles of fixed contour length. This study is also inspired by experiments performed on M13 and fd viruses [41]. The experiments show that long, non-commensurate elongated guest particles diffuse faster in the smectic phase formed by elongated host particles. Nevertheless, the experiment is limited to a few ratios between guest and host contour lengths and fixed values of the particles persistence length. Simulations may contribute to find an optimal combination for, perhaps, finding the *fastest* guest. They even may help us understand if the relevant parameter is really the ratio or the actual contour lengths of both guest and host particles. The third research question in our study is then *how do the anisotropy and the flexibility of elongated particles affect their diffusion in a lamellar background phase?* As pointed out in Reference [41], the answer to this question may help to elucidate the transport mechanisms of macromolecules (such as proteins) through cellular or other biological membranes, which is of interest to cell biology and drug delivery applications [4].

Our three previous research questions are about structural and dynamical aspects considered separately. To conclude our work, we combine them in the study of the dynamics of clusters and percolation in the isotropic phase of hard particles. Percolation of elongated colloidal particles is a very interesting topic

that is not completely understood. Despite that, unlike our previous studies, here we focus on spherical colloidal particles for reasons of simplicity as, in this case, there is no rotational diffusion involved. Our fourth question is *how long does it take clusters to substitute all particles that initially form it?* We are also interested in whether geometric percolation exhibits critical slowing down, because of the critical nature of the percolation transition. We find that the connectivity length and concentration both impact on the survival dynamics of pre-critical clusters. Surprisingly, we do not observe any critical slowing down upon approach of the percolation transition.

1.3 Outline of the thesis

The remainder of this thesis contains six chapters. Chapter 2 contains a general introduction to the methods employed in our work. Additional procedures that are specific to one of our studies are presented in the methods and analysis section in the respective chapter. These are the remainder five chapters, each of them addressing one of the research questions presented in Section 1.2. Hence, in Chapter 3, we describe how the aspect ratio and bending flexibility affect the phase behaviour of rod-like particles and analyse the particle conformation in various phases. In Chapter 4, we investigate the effect a weakly attractive tip has on the stability of the phases previously described and discuss their microscopic structure. The chapter has attached to it two appendices. In the first one, we present a Maier-Saupe-McMillan type theory to describe the anti-ferroelectric phase transition found in the simulations. In the second appendix, we present the comparison between our results and experimental findings obtained by collaborators from the CRPP in Bordeaux. In Chapter 5, we describe the dynamics of short and long guest particles in the smectic A phase formed by elongated host particles. We also discuss the effect of the persistence length and the flexibility of the particles studied. In Chapter 6, we present results relative to the dynamics of clusters and percolation in the isotropic phase. In this chapter, unlike the others, we focus on repulsive spheres. Finally, in Chapter 7, we present our general conclusions and outlook.

Chapter 2

Our approach

We employ coarse-grained computer simulations to study the structure and dynamics of elongated colloidal particles in suspension. In this chapter, we provide a general introduction to the simulation methods. We also describe the specific interactions we employ to model elongated colloidal particles. Finally, we provide details about the methodology procedures that are common to our studies. In particular, we explain the analysis that we employ to classify the various liquid-crystalline phases and study the diffusion of particles.

2.1 Computer simulations

The aim of our work is to investigate how the particles' properties and interactions affect self-organised structures of elongated colloidal particles from the thermodynamic and dynamical point of view. For this purpose, we use the simulation package LAMMPS [50] to perform coarse-grained computer simulations: Molecular Dynamics (MD) simulations for the measurement of stationary properties and Langevin Dynamics (LD) simulations for the measurement of time dependent properties [51]. MD and LD simulations are computational methods usually employed to obtain equilibrium and transport properties of classical many-particle systems. In a system of n particles, the i -th particle is characterised by its position $\mathbf{r}_i = (x_i, y_i, z_i)$ and mass m_i . The particles have their movement dictated by the interaction potential (presumed pair-wise additive) and the external potential energies (electric or magnetic fields, for example). The potential energy U combines both potential energies and is a function of all particle positions, $U = U(\mathbf{r}_1, \mathbf{r}_2, \dots, \mathbf{r}_i, \dots, \mathbf{r}_n)$. The equation of motion of each particle then depends on the simulation method considered.

In MD simulations, the movement is described by the Newton's equations of motion, $\mathbf{F}_i^t = m_i \ddot{\mathbf{r}}_i$, where the total force \mathbf{F}_i^t corresponds to the total conservative force \mathbf{F}_i^c acting on the particle i , $\mathbf{F}_i^t = \mathbf{F}_i^c$, and the dots indicate time derivatives. The conservative force is obtained from the potential energy by the relation $\mathbf{F}_i^c = -\nabla_i U$, where ∇_i is the gradient with respect to the position of the particle i , $\nabla_i = (\partial/\partial x_i, \partial/\partial y_i, \partial/\partial z_i)$. In LD simulations, a friction force \mathbf{F}_i^f and a stochastic force \mathbf{F}_i^s are also included to the total force, $\mathbf{F}_i^t = \mathbf{F}_i^c + \mathbf{F}_i^f + \mathbf{F}_i^s$. The friction force emulates the viscosity of the fluid. This term is given by $\mathbf{F}_i^f = -\gamma_i \dot{\mathbf{r}}_i$, where γ_i is the friction constant between the fluid and the particle i . The stochastic force represents the net forces resulting from the many collisions with the fluid particles. It has the property $\langle \mathbf{F}_i^s(t + \Delta t) \cdot \mathbf{F}_j^s(t) \rangle = 2\gamma_i k_B T \delta_{ij} \delta(\Delta t)$, where the angular brackets indicate an ensemble average, k_B is the Boltzmann constant, T is the absolute temperature, δ_{ij} is the Kronecker delta, and $\delta(\Delta t)$ is the Dirac delta function.

The simulations are based on the simultaneous numerical time integration of the equations of motion of each particle. In the method, time is discretised into small time steps, the forces on each particle are calculated at each time step, new positions are calculated and then the procedure is repeated for the next time step. Final result is the time evolution of the positions of all particles. For this purpose, a simple Verlet algorithm is the most commonly employed one [51]. It can be obtained from the Taylor expansion of the particle position \mathbf{r}_i around time t . The position of each particle is updated according to the relation $\mathbf{r}_i(t + \Delta t) = 2\mathbf{r}_i(t) - \mathbf{r}_i(t - \Delta t) + (\mathbf{F}_i^t/m_i)\Delta t^2 + \mathcal{O}(\Delta t^4)$, which means that the new positions are an estimate with an error of order Δt^4 .

2.2 Model particles

We model elongated colloidal particles as semi-flexible bead-spring chains of b overlapping beads of same mass m and diameter D . The beads correspond to the particles we described in the previous section. From now on, we refer to them as beads to avoid confusion with the elongated colloidal particles modelled by the bead-spring chains. The i -th particle form bonds of length s_i in units of D and angles of measure θ_i in radians with the consecutive beads in a chain. We characterise the bond by the distance to the neighbour bead $i + 1$, $\mathbf{s}_i = \mathbf{r}_{i+1} - \mathbf{r}_i$. Therefore the bond length is $s_i = \|\mathbf{s}_i\|$, and the normalised \mathbf{s}_i represents the direction of the bond, $\hat{\mathbf{s}}_i = \mathbf{s}_i/s_i$. The angle is defined as $\theta_i = \arcsin\left(\|\hat{\mathbf{s}}_i \wedge \hat{\mathbf{s}}_{i-1}\|\right)$. The distance s_{ij} between any two beads i and j that are not bonded is defined as $s_{ij} = \|\mathbf{s}_j - \mathbf{s}_i\|$. See Figure 2.1. The centre of mass of the beads within the k -th chain corresponds to its position, that is $\mathbf{R}_k = \sum_i \mathbf{r}_i/b$ as the mass $m_i = m$ is the same for all beads. The orientation of each particle is described by the normalised, average direction of the $b - 1$ vectors described by the distances between the centres of consecutive beads in the same chain, $\hat{\mathbf{S}}_k = \sum_i \mathbf{s}_i/(b - 1)$.

Interactions

The pairs of bead that form a bond interact via a harmonic potential

$$U_i^s = \frac{1}{2}\kappa_s \left(s_i - \frac{D}{2}\right)^2, \quad (2.1)$$

which means that the beads overlap by a half diameter distance. Here, κ_s is the harmonic bond stretch constant, which we fix to a reasonably large value of $100 k_B T/D^2$ to ensure minimal entropic stretching of the bonds. In other words, the average bond length is very close to the rest bond length of one-half D . This merged-sphere rod configuration provides a smoother particle surface. This way, our particle approaches the spherocylinder rod, facilitating the comparison with other works and preventing a biased stacking between the chains in highly congested phases. A harmonic bending potential

$$U_i^\theta = \frac{1}{2}\kappa_\theta (\theta_i - \pi)^2, \quad (2.2)$$

where κ_θ is the bending constant, is assigned to consecutive bonds between beads to model bending stiffness.

Except for the nearest neighbour beads along the same chain, all beads interact via a purely repulsive, truncated and shifted Lennard-Jones (LJ) potential,

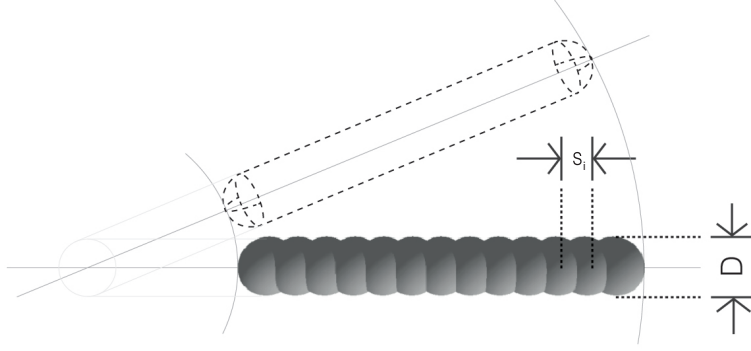


Figure 2.1: Schematic representation of our model particles. Elongated colloidal particles are modelled as a bead-spring chains with diameter D . The length of the i -th bond s_i is such that the beads partially overlap for a smoother surface, allowing closer comparison with spherocylinders (dashed lines). The rest distance of the harmonic bond potential corresponds to half of the bead diameter.

also known as the Weeks-Chandler-Anderson (WCA) potential:

$$U_{ij}^{WCA} = \begin{cases} 4\epsilon \left[\left(\frac{s_{ij}}{D} \right)^{-12} - \left(\frac{s_{ij}}{D} \right)^{-6} \right] + \epsilon, & \text{if } s_{ij} \leq 2^{1/6} D \\ 0, & \text{if } s_{ij} > 2^{1/6} D \end{cases}. \quad (2.3)$$

Here, the potential energies and ϵ are given in units of thermal energy $k_B T$. As we are not using the hard-core potential, the effective hard sphere diameter of a bead along the chain D_{eff} is slightly larger than D : $D_{\text{eff}} \sim 1.017D$. This estimate can be obtained by comparing the second virial coefficient for our purely repulsive soft potential to the second virial coefficient for the hard sphere potential.

Particle properties

Due to the harmonic bond stretch, the contour length of the particles, L , and, consequently, their aspect ratio, $L/D = (b-1)\langle s \rangle/2$, $\langle s \rangle$ denoting the average bond length of all chains, are not fixed but slightly variable. Hence, we refer to the aspect ratio as that at very low densities L_0/D to characterise our particles. The actual contour length of the particles is somewhat smaller than this, in particular in the more congested phases due to the high ambient pressure that compresses the particles somewhat. See Reference [52] for a discussion. The persistence length L_p of the particle depends on the harmonic bend constant. We have the simple relation $L_p = \kappa_\theta s / k_B T$, valid for an infinitely large number of beads and $\kappa_\theta s^2 / k_B T \gg 1$ [39]. The value obtained in our simulations for the end-to-end distance of particles of various persistence lengths calculated by the previous

relation in the isotropic phase compares well with the value of the end-to-end distance predicted by the worm-like chain model, showing that the relation is indeed appropriate to describe the persistence length of our particles. See Chapter 3. We measure the particles flexibility by the ratio between the contour length over persistence length, L_0/L_p .

2.3 Phase behaviour and microstructure

In our MD simulations we insist on using the NPT (or isothermal-isobaric) ensemble when pressure and temperature are fixed with the aid of the Nosé-Hoover baro- and thermostat. In other words, the number of particles (or chains) N , pressure P , and temperature T are constant. The particles are initially parallel to the z -axis and organised in a hexagonal lattice and divided in 16 AAA staked layers, which means that the layers are identical copies shifted along the director, and in each layer there is perfect hexagonal ordering. We used a simulation box with periodic boundary conditions and dimensions L_x , L_y , and L_z . The barostat can adjust the rectangular simulation box dimensions independently, which allows relaxation to the correct layers spacings in the smectic and crystalline phases. Therefore the changes in the box shape are anisotropic. The system is equilibrated when its volume V no longer changes with time. Unless specified in the subsequent chapters, each simulation runs for 20000 time units. Our time unit is set by the LJ timescale $(m/k_B T)^{1/2} D$ and we use time steps of 10^{-3} in these units in our simulations, implying that our simulations run 2×10^7 time steps. The relaxation times for temperature and pressure are 0.01 and 0.1 time units corresponding to about 10 and 100 time steps, respectively. Once equilibrated, we obtain the particle configurations from the positions of all beads. Approximately 100 configurations of every run are stored, in other words, one in every 200 time units. Once equilibrated, we obtain the particle configurations from the positions of all beads.

The reason why we take the crystal phase as our initial configuration is that starting from an ordered structure we are unlikely to end up in a jammed state. Arguably, the lower the symmetry of the configuration of particles the more likely it jams on account of the associated decrease in free volume. Of course, one could argue that this procedure might give rise to metastable layered phases, that is, the smectic A and B phases and the crystalline phase. To verify that this is not the case, we performed compression simulations for one particular aspect ratio and one degree of flexibility near all phase transitions that we find in our simulations starting off the crystalline state. For this purpose, we use a configuration from the highest concentration of the less ordered phase and increase the pressure to a

value at which the more ordered phase should appear. From the evaluation of the order parameters (see below), we find that the order in which the transitions appear are consistent with the expansion simulations and the largest disagreement in the concentration at which the transitions occur is 0.5%. Hence, we believe that the results our simulations starting off the crystal configuration are robust. Next we calculate order parameters and correlation functions in order to classify the state of aggregation and build phase diagrams. Refer to References [53–55] for a detailed discussion.

In order to study the phase behaviour, the MD simulations are performed at various pressures. The corresponding volume fraction ϕ of any given configuration is defined as $\phi = Nv_0/V$, where v_0 is the volume of a chain we approximate by taking a spherocylinder with volume $v_0 = \pi D^3/6 + \pi D^2 L_0/4$. That means that the actual volume fraction is slightly lower than the value we adopt to represent it. This choice is made in order to keep most of the parameters of our simulation fixed. In Figure 2.2, our methods and analysis for the phase classification are schematically represented.

Order parameters

An order parameter is a normalised parameter indicating the degree of order of a system. The system is in a disordered state if its value is 0 and in an ordered state if its value is 1. The first order parameter employed is the nematic order parameter, which quantifies the alignment with a preferential direction. For each equilibrium configuration considered, the global nematic order parameter can be obtained from the following tensor

$$Q_{vw} = \frac{1}{N} \sum_{j=1}^N \left(S_{jv} S_{jw} - \frac{1}{3} \delta_{vw} \right), \quad (2.4)$$

where v, w correspond to the components of the vector in the Cartesian coordinate system and δ_{vw} is the Kronecker delta. S is the orientation of the particle, as previously defined in this section. The nematic order parameter S_2 and the director $\hat{\mathbf{n}}$ are the largest eigenvalue and the respective eigenvector of this tensor. The nematic order parameter S_2 for one configuration is proportional to the average angle between the director and the direction of each molecule ϑ , $S_2 = \langle P_2(\cos \vartheta) \rangle = \frac{3}{2} \langle \cos^2 \vartheta \rangle - \frac{1}{2}$, where P_2 is the second Legendre polynomial, $P_2(q) = (3q^2 - 1)/2$.

Once we obtain the director $\hat{\mathbf{n}}$ from the procedure described above, we quantify the organisation in layers and determine their size using the function

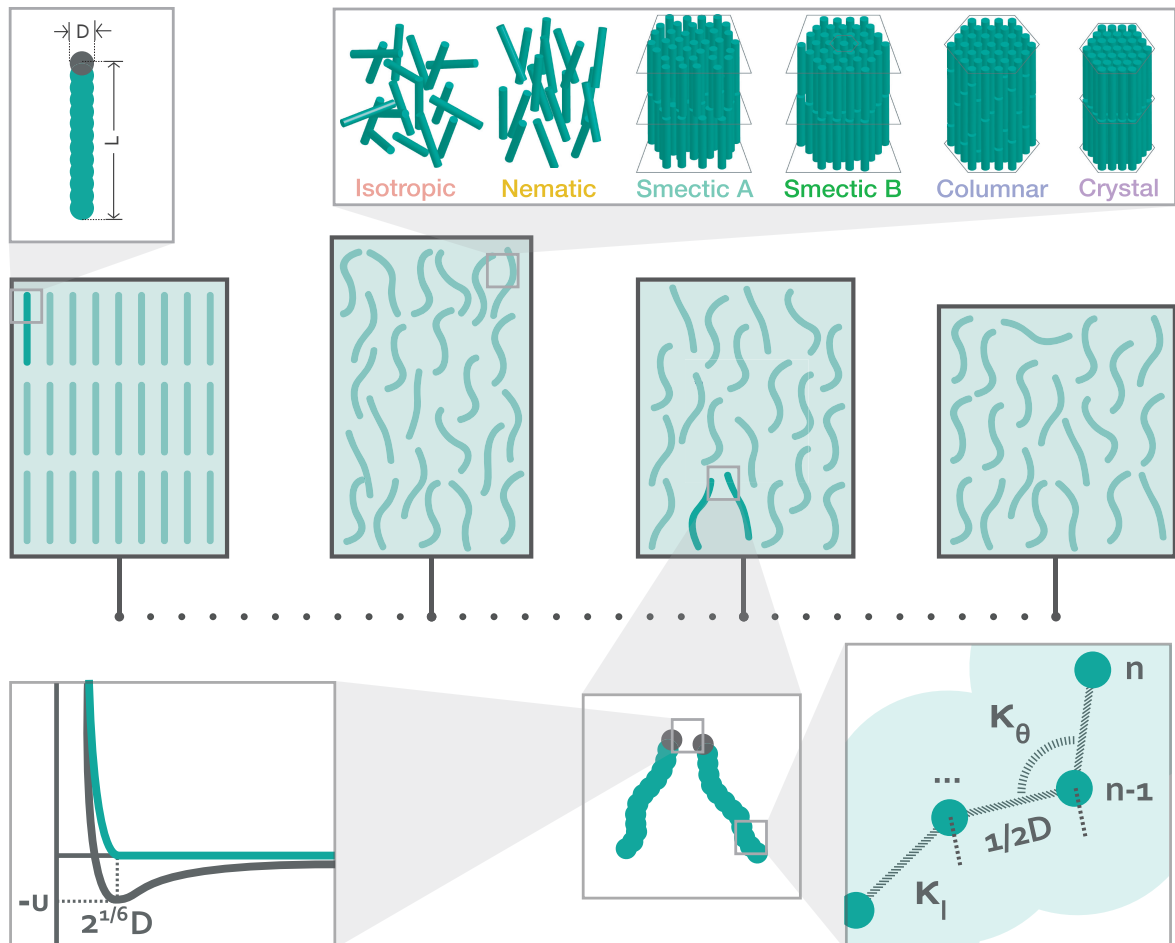


Figure 2.2: Schematic representation of our methods and analysis. Model particles are overlapping, purely repulsive bead-spring chains. Nearest neighbours interact by a harmonic elastic and bending potential. Except for the nearest neighbour beads along the same chain, all beads interact via the WCA potential. We calculate order parameters and correlation functions in order to classify the phases. We are able to distinguish between the isotropic, nematic, smectic A, smectic B, columnar, and crystalline phases.

defined as follows:

$$f(q) = \left| \frac{1}{N} \sum_{k=1}^N \exp \left(2\pi i \frac{\mathbf{R}_k \cdot \hat{\mathbf{n}}}{q} \right) \right|, \quad (2.5)$$

where N is the total number of particles and the imaginary number i is defined as $\sqrt{-1}$. This function presents several local maxima depending on the type of order. From the set of arguments of the maxima, $\arg \max f$, we are interested in the value nearest to the particle length $L+D$, because the smectic layers are expected to be comparable to the size of the particles. This value corresponds to the interlayer distance λ . From the interlayer distance λ , we obtain the smectic order parameter τ given by $\tau = f(\lambda)$. Figure 2.3 represents the function f calculated for several example configurations indicated in the figure.

The bond order parameter ψ_6 is defined as

$$\psi_6 = \left| \frac{1}{N} \sum_{k=1}^N \frac{1}{\mathcal{N}} \sum_{l=1}^{\mathcal{N}} \exp(6i\vartheta_{kl}) \right|, \quad (2.6)$$

where \mathcal{N} is the number of particles near to the reference particle k and ϑ is the angle between the director and the direction of each molecule, as previously defined in this section. These nearest neighbour particles are within the volume defined by a cylinder parallel to the director and centred in the reference particle the radius $1.7D$. The height of the cylinder is the average particle size $L + D$.

Pair correlation function

We employ the in-layer pair correlation function g to distinguish between the smectic B and crystalline phases. Details about the procedure is presented in Chapter 3.

$$g(q) = \frac{1}{N} \left\langle \frac{1}{\rho} \sum_{k=1}^N \sum_{l=k+1}^N \delta(q - \|\mathbf{R}_{kl} \wedge \hat{\mathbf{n}}\|) \Theta \left(\frac{\lambda}{2} - |\mathbf{S}_{kl} \cdot \hat{\mathbf{n}}| \right) \right\rangle, \quad (2.7)$$

where $\rho = N/V$ is the number density of particles and Θ is the Heaviside step function, which filters the particles that are in the same layer.

2.4 Diffusion

The LD simulations are performed in the NVT (or canonical) ensemble using the Langevin thermostat [50, 56]. In this case, the volume V is constant with fixed L_x ,

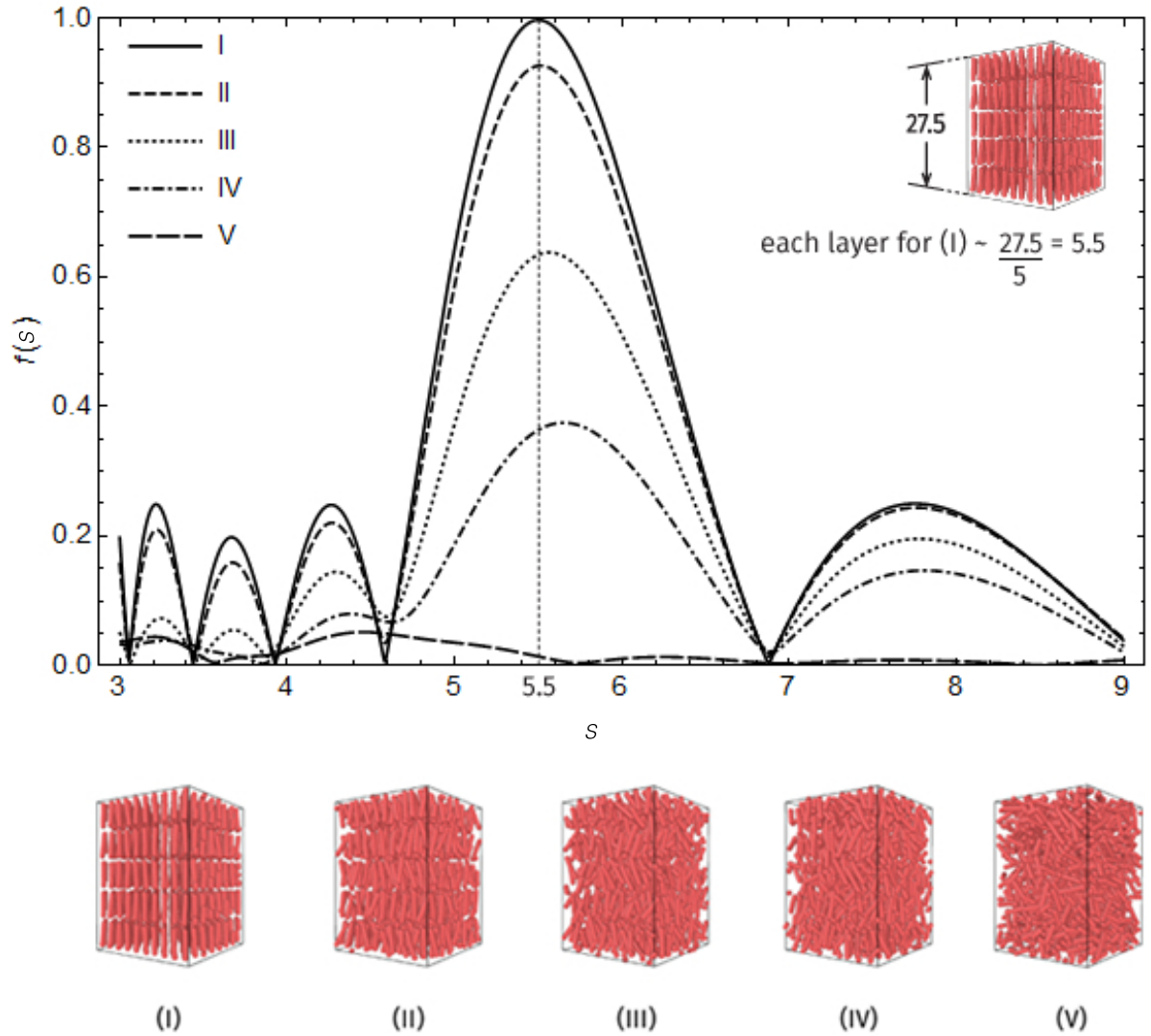


Figure 2.3: The full and the various types of dashed line correspond to the function from Equation 4.5 calculated for the particle configurations I through V represented below the graph. Configurations are obtained from the melting of bead-spring chains initially organised in a AAA crystal-like phase (configuration I) to the isotropic phase (configuration V) at same concentration for the purpose of illustration. The value of the function at the local maxima nearest to the particle length $L + D$ corresponds to the smectic order parameter τ . The illustration on the right top we show that the distance in which the function is maximum in fact corresponds to the interlayer distance λ in units of the particle diameter D , which we estimate dividing the box size along the director, L_z , by the total number of layers inside the simulation box.

L_y , and L_z dimensions, as specified by the initial configuration. The initial configuration is obtained from the set of equilibrium configurations obtained from MD simulations performed as described in the previous section (in the NPT ensemble). From the configurations obtained from the LD simulations, we study such diffusion in the various liquid-crystalline phases. Diffusion is a process caused by the molecular motion of the particles in the fluid, which is represented by the stochastic force previously described. It is usually measured by the diffusion coefficient \mathcal{D} , which we obtain from the mean squared displacement (MSD) by the relation $\langle \|\mathbf{R}(t + \Delta t) - \mathbf{R}(t)\|^2 \rangle = 6\mathcal{D}t$. For particles in liquid-crystalline phases, we separate the diffusion coefficient \mathcal{D} into the components parallel and perpendicular to the director $\hat{\mathbf{n}}$, \mathcal{D}_\perp and \mathcal{D}_\parallel .

In the smectic phase, as discussed in the Chapter 1, the elongated particles engage in a non-Gaussian hopping-type diffusion in smectic phases. We quantify it by calculating the self-van Hove function G_s , that is defined as [57] and following [58]:

$$G_s(Z, \Delta t) = \frac{1}{N} \left\langle \sum_{k=1}^N \delta(Z - Z_k(t + \Delta t) + Z_k(t)) \right\rangle, \quad (2.8)$$

where Δt defines the time span between the configurations and Z_k is the component position of the particle centre of mass along the director. The van Hove function measures the time-dependent probability distribution of particles that, for the displacement along the director, shows peaks at integer multiples of the smectic layer thickness [58].

Chapter 3

Self-organisation of semi-flexible elongated particles

In this chapter, we present a comprehensive computer simulation study of the liquid-crystalline phase behaviour of purely repulsive, semi-flexible rod-like particles. For the four aspect ratios we consider, the particles form five distinct phases depending on their packing fraction and bending flexibility: the isotropic, nematic, smectic A, smectic B and crystalline phase. Upon increasing the particle bending flexibility, the various phase transitions shift to larger packing fractions. Increasing the aspect ratio achieves the opposite effect. We find two different ways in which the layer spacing of the particles in the smectic A phase may respond to an increase in concentration. The layer spacing may either decrease or increase depending on the aspect ratio and flexibility. For the smectic B and the crystalline phases, increasing the concentration always decreases the layer spacing. Finally, we find that the layer spacing jumps to a larger value on transitioning from the smectic A to the smectic B phase and we explain this in terms of the gain in free volume due to the increased ordering of the phase.

3.1 Introduction

Rod-like colloidal particles, DNA strands, carbon nanotubes, and filamentous viruses have in common that, if dispersed in a fluid at sufficiently high concentrations, they exhibit various kinds of liquid-crystalline phase [2, 59–61]. This is because with increasing concentration, the dispersion runs out of free volume leading to increasingly ordered states. This class of material is usually referred to as lyotropic liquid crystals, which sets it apart from that of thermotropic liquid crystal, because the driving force is not energy but, in essence, entropy. This was first recognised by Lars Onsager in his seminal paper describing the isotropic-to-nematic phase transition of cylindrical particles interacting via a hard-core repulsive interaction [19]. In agreement with experiment and computer simulations, the theory predicts the transition to occur at a volume fraction that decreases inversely proportional to the aspect ratio of the particles. The impact of particle bending flexibility on the isotropic-nematic transition was first investigated theoretically by Khokhlov and Semenov more than thirty years later [62, 63], and a decade after that others investigated how flexibility impacts upon the nematic-columnar and the nematic-smectic A transition [31, 64–66].

Over the past few decades, interest in lyotropic liquid crystals has increased significantly, in part because of potential applications and in part because of the development of well-controlled model particles [1, 67]. Indeed, lyotropic liquid crystals have been intensively investigated experimentally [26–28, 32, 33], theoretically [20–24] and with the aid of computer simulations [34, 36–40, 68]. In spite of this, our understanding of the isotropic and nematic phases is most comprehensive, whilst that of the others remains much less detailed. In particular, how flexibility and aspect ratio impact upon the other liquid crystal transitions have received much less attention. Here, we aim to fill in this gap from the perspective of computer simulations, in particular because these are much more difficult to address theoretically. One reason is that the second virial approximation, which allowed Onsager to accurately describe the isotropic-nematic transition, no longer holds at densities where the smectic and columnar phases appear. Another reason is translation-rotation coupling, which makes density functional and integral equation theories virtually intractable [23, 31, 69].

We extend earlier simulation studies on semi-flexible chains by covering a larger range in persistence length, aspect ratio, and particle numbers, and investigate more comprehensively the microscopic structure of the liquid crystalline and crystalline phases. In agreement with theory and simulation, we find that particles with longer aspect ratio support over a larger concentration range and a broader range of bending flexibilities liquid-crystalline states. This is particularly true for the nematic and the smectic A phase. We find that the stability of

the smectic B and crystalline phases, recently both found experimentally in colloidal systems [26, 27], to be less sensitive to both aspect ratio and flexibility, at least for the ranges investigated. The aspect ratio of our particles vary between 6 and 11 while the ratio of the bare contour length and persistence length vary between 0.05 and 0.5. For these aspect ratios and persistence lengths all phase transitions are either second or weakly first order, except the transition between smectic A and smectic B that clearly is first order. The difference in behaviour of the smectic A and B phases expresses itself most clearly in how the layer spacing responds to increases in density. For the smectic B phase, the layer spacing always decreases with increasing density. This is not so for the smectic A phase, where depending on aspect ratio and persistence length it may in- or decrease, in truth depending on whether the increase of the particles density is translated into reduced layer spacing and/or increased in-layer density.

The remainder of this chapter is structured as follows. In Section 3.2 we describe our model particles that we construct from overlapping, mutually repulsive bead-spring chains. We also make explicit our simulation protocol and explain how we identify the various liquid crystal phases in our simulation data. In Section 3.3 we present the phase diagrams we obtain and show how the aspect ratio and flexibility influence the phase transitions. In Section 3.4 we describe the influence of the phase transitions on the individual particle structure and smectic layer thickness. We furthermore present a simple model based on Onsager theory that explains the changes in the particle length as a function of density in the isotropic and nematic phases in Appendix 3.5. Finally, in Section 3.5, we present our most important conclusions.

3.2 Methods and analysis

To study the equilibrium properties of semi-flexible rod-like particles, we perform MD simulations on 4608 particles modelled according to the description provided in Section 2.2. In our simulations we allow for chains consisting of $n = 13, 15, 17,$ and 21 beads per chain. The corresponding aspect ratios L_0/D in the limit of zero pressure we find to be equal to $L_0/D = 6.46, 7.54, 8.62,$ and 10.77. For every aspect ratio we vary the bending stiffness κ_θ to obtain a series of ratios of the base contour length L_0 and the persistence length L_p , $L_0/L_p = 0.05, 0.1, 0.2, 0.3, 0.4,$ and 0.5. We perform isobaric-isothermal (NPT) simulations at various pressures as described in Section 2.3. Each simulation runs for 20000 time units. Our time unit is set by the LJ timescale $(m/k_B T)^{1/2} D$ and we use time steps of 10^{-3} in these units in our simulations, implying that our simulations run 2×10^7 time steps. The relaxation times for temperature and pressure are 0.01 and 0.1 time

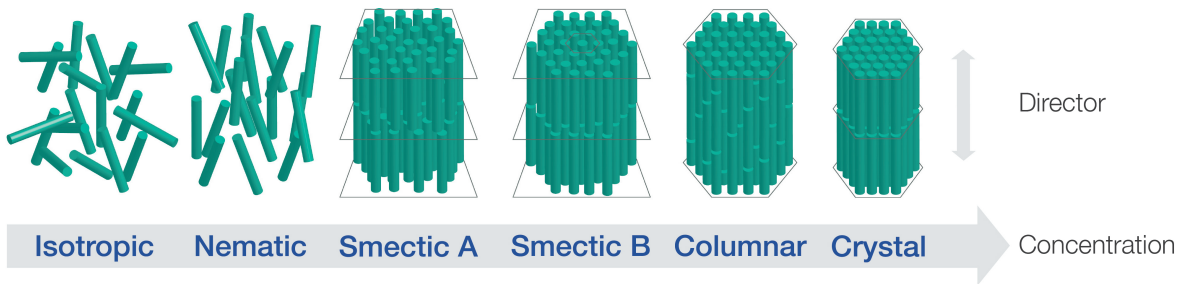


Figure 3.1: Schematic representation of the liquid crystal phases found in aqueous dispersions of the rod-like fd virus [27]. The phase sequence with increasing concentration is isotropic, nematic, smectic A, smectic B, columnar, and crystal. The double pointed arrow indicates the preferential direction of the aligned particles, the director. We note that the precise structure of the crystal phase is unknown.

units corresponding to about 10 and 100 time steps, respectively. Approximately 200 configurations of every run are stored, in other words, one in every 100 time units.

The initial configuration is that of the crystal phase, with all rod-like particles perfectly aligned, AAA stacked in 16 layers of 18×16 particles each. That the initial box is very elongated is sensible because it is approximately the 16 layers times the length of the particles that themselves have a large aspect ratio. In the isotropic phase the box elongation relaxes and on average becomes isotropic albeit that the box shape fluctuates considerably, in particular near the isotropic-to-nematic phase transition. In the nematic phase the box can become very much more elongated than the initial elongation. In the smectic and crystalline phase the box anisometry remains roughly equal to the initial one. If in our simulations one box dimension drops below about one particle length we discard the run.

The equilibrium configurations stored are used to calculate the usual order parameters and the pair correlation functions of the collection of particles. The order parameters quantify (i) the degree of orientation of the chains, given by the nematic order parameter S_2 ; (ii) the organisation in layers perpendicular to the director, given by the smectic order parameter τ ; and (iii) the hexagonal ordering of the closest neighbours within the same layer, which is described by the bond order parameter ψ_6 . See Section 2.3 for details. With these order parameters, the isotropic, nematic, smectic A, columnar, and smectic-B or crystal phases can be identified and distinguished. All these phases are schematically represented in Figure 3.1.

In the isotropic phase there is only short-range correlation between the po-

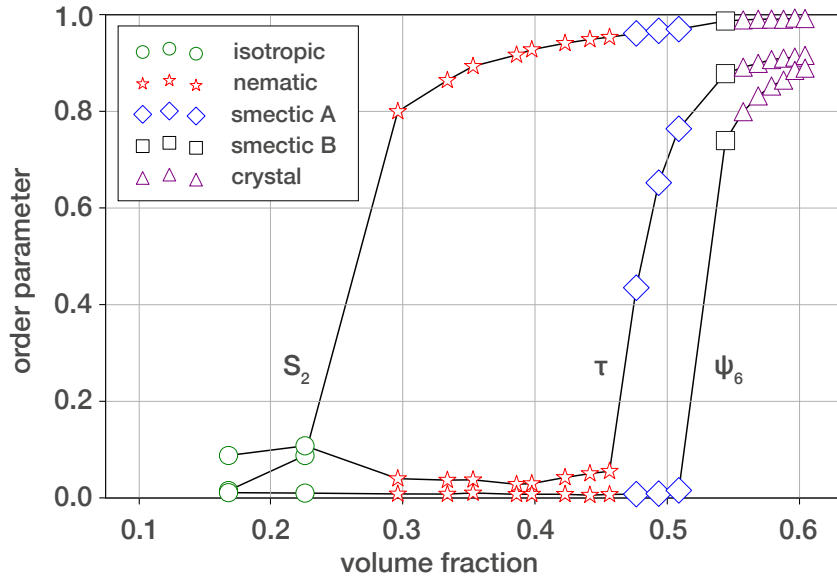


Figure 3.2: Order parameters as a function of the volume fraction ϕ for aspect ratio $L_0/D = 10.77$, and flexibility $L_0/L_p = 0.05$. Indicated are, respectively the nematic order parameter S_2 (degree of alignment along the director), the smectic order parameter (organisation in layers) τ , and the bond order parameter ψ_6 (in-plane hexagonal organisation)

sitions and between the orientations of the chains, and S_2 should be zero, but need not be exactly that on account of finite size effects [70]. With the alignment of the particles in the nematic phase, the order parameter S_2 increases abruptly when crossing the phase boundary, so it can be readily identified. The same is true for the smectic and bond order parameters τ and ψ_6 , allowing us to identify the smectic A phase and the smectic B or crystal phase. See Figure 3.2. Snapshots of the various phases are given in Figure 3.3. The smectic B phase differs from the smectic A and crystal phases in that it does have (quasi) long-range in-plane bond order but no actual long range positional order. The smectic A phase has neither and the crystal phase has both long-range bond and positional order. We cannot distinguish between the smectic B and crystal phase based only on calculating the correlation function g_6^{lay} of the order parameter ψ_6 due to the finite size of the system. See Figure 3.3. However, we can distinguish between them by considering the in-layer pair correlation function g_{lay} of the centres of mass of the chains [39, 71].

As can be seen in Figure 3.4 (a) and (b), there is a clear difference in $g_{\text{lay}}(r)$ between two states at different pressures with equal magnitude of the order parameters S_2 , τ , and ψ_6 . Figure 3.4 (a) exhibits a split second peak in $g_{\text{lay}}(r)$, a characteristic of a crystalline phase that the system with the pressure shown in (b) does not have. We therefore associate the absence of peak splitting with the

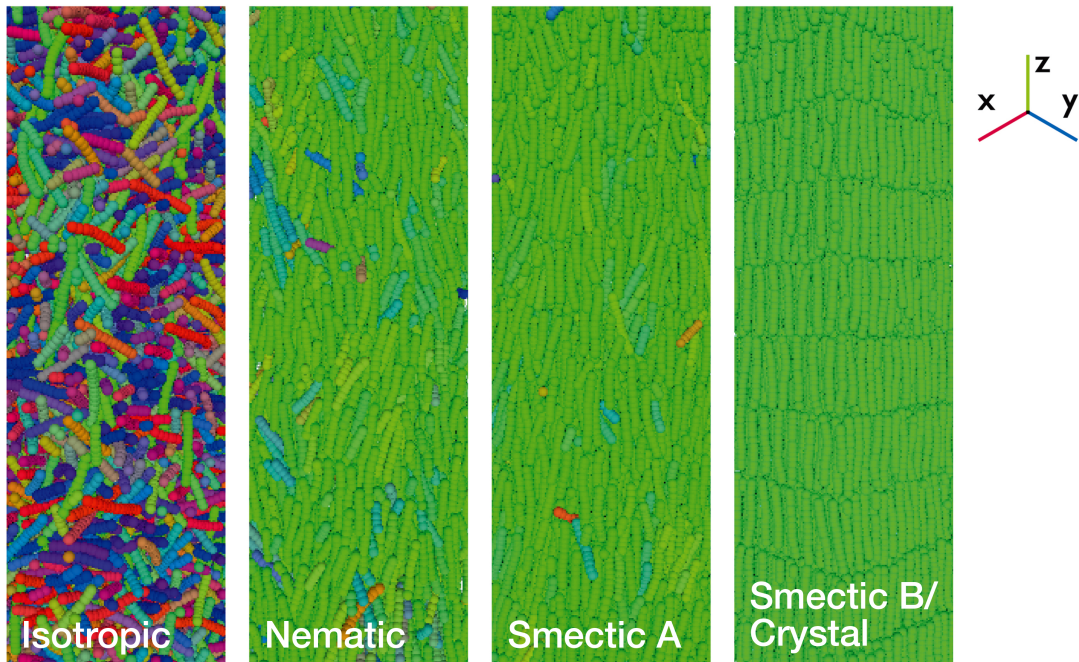


Figure 3.3: Snapshots representing the arrangement of particles along the director for the different phases observed in our simulations for aspect ratio $L_0/D = 6.46$ and ratio of contour length and persistence length of $L_0/L_p = 0.1$. From left to right with increasing density: isotropic, nematic, smectic A, smectic B, and crystal. The colour of the particle is a combination of red, blue, and green, whose intensities are respectively proportional to the x , y , and z components of the orientation of the particle.

smectic B phase and assume the phase transition takes place when the second peak in the pair correlation function splits. So, we use the splitting of the second peak in $g_{\text{lay}}(r)$ as a proxy for distinguishing between the smectic B and the crystal phase. Note that the smectic B phase that we identify in (b) has a much noisier g_6^{lay} than that of the crystal phase of (a). The difference in structure of the crystal and smectic B phase is also evident from the snapshots also presented in Figure 3.4.

In order to determine the crystal symmetry, we compare the pair correlation function g_{lay} of the centers of mass of the particles. We distinguish four cases. In the first, we calculate the pair correlation function for particles in the same layer. In the second, we consider pairs of particle in consecutive layers. In the third and fourth, the pair correlation function considers pairs of particle separated by one and two layers. We expect that all pair correlation functions must be similar for the AAA crystal structure, whilst the first and fourth should be similar for the ABC structure. We observe neither of these patterns, implying that we cannot pinpoint the exact crystal structure. A possible explanation for this is that the

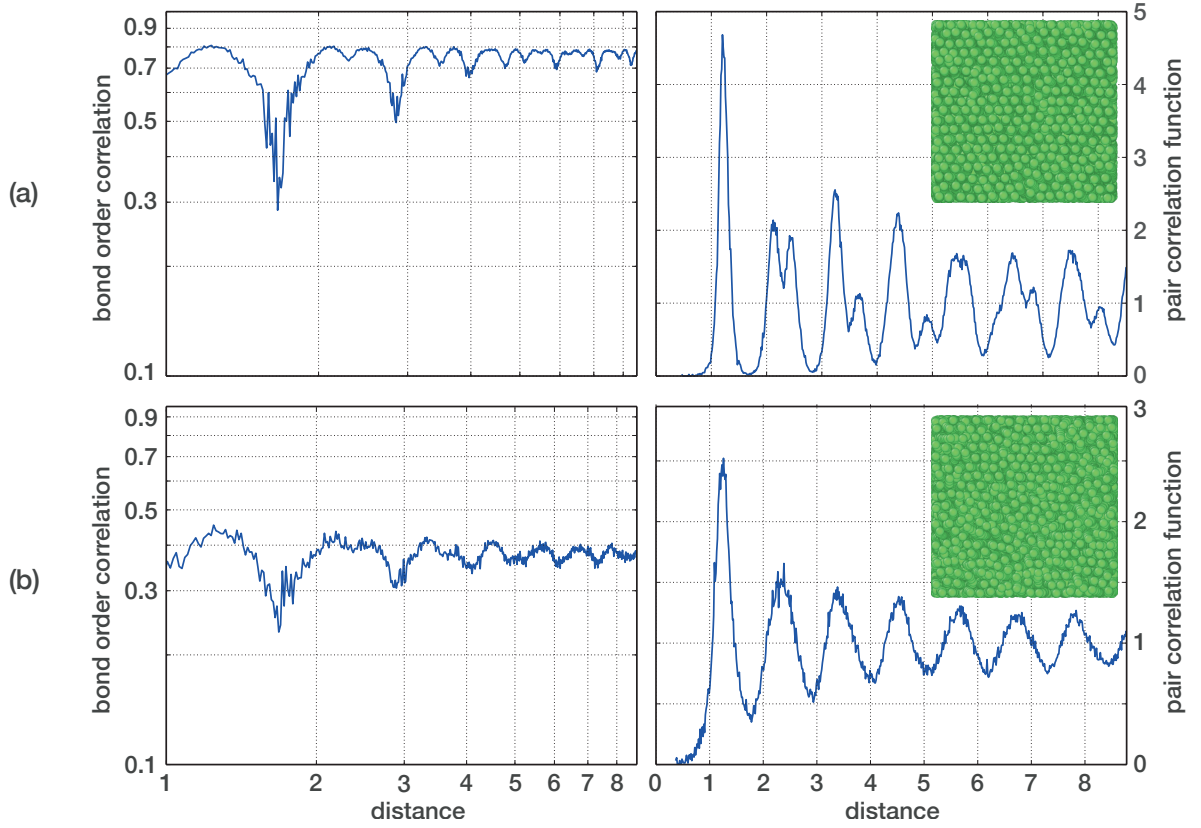


Figure 3.4: (a) The bond order ψ_6 correlation function $g_6^{\text{lay}}(r)$ (left) and the pair correlation function $g_{\text{lay}}(r)$ (right) as a function of the reference particle distance in units of D for particles with aspect ratio $L_0/D = 10.77$, flexibility $L_0/L_p = 0.5$ and volume fraction $\phi = 0.63$. The pair correlation function exhibits peaks characteristic for a crystal phase and hence we identify it as such. (b) The same for a volume fraction of $\phi = 0.57$. The pair correlation function does not show the characteristic crystal peaks. Hence at a volume fraction of $\phi = 0.57$ the particles must be in the smectic B phase. Note that the bond order correlation shows a weaker decay in the crystal phase in comparison to the smectic B. See also the main text.

ordering between layers is not so well defined for semi-flexible particles. The fact that we start off from an initial AAA structure that does not seem to survive, we conclude that our simulations are not kinetically trapped.

3.3 Phase behaviour

The phase diagrams of our particles are presented in Figure 3.5. Recall that our particles are semi-flexible, rod-like chains interacting via a soft-core, repulsive potential. We present phase diagrams as a function of volume fraction and bending flexibility, ranging from $L_0/L_p = 0.05$ to 0.5 covering particles from near the rigid-rod limit to semi-flexible chains, for four aspect ratios, $L_0/D = 6.46, 7.54, 8.62,$ and 10.77. We distinguish between the following phases: isotropic, nematic, smectic A, smectic B and crystal (Figure 3.3). For our set of parameters, we did not encounter any evidence for the occurrence of a columnar phase. Based on what we know on the phase behaviour of the fd virus, which does support a columnar phase, we must conclude that our particles do not have a large enough aspect ratio for this phase to appear in the phase diagram [28].

Focusing on the aspect ratio $L_0/D = 6.46$ first, representing the trends observed for the other aspect ratios, Figure 3.5 tells us that all phase transitions shift to larger volume fractions with increasing flexibility. The isotropic-nematic transition increases approximately linearly with increasing degree of flexibility, which for large persistence lengths is consistent with theory and Monte Carlo simulations [34]. Both the isotropic-nematic and the nematic-smectic A transition are significantly impacted upon by any bending flexibility. Theoretically this has been predicted to be the case albeit that these theories are typically valid in the long-chain and/or large persistence length limits relative to the width of the particles [20–22, 31, 62, 63, 66]. The result also agrees with previous simulation by Bladon and Frenkel [36]. We find that the smectic A phase is strongly destabilised by decreasing the chain stiffness, in line with results from earlier computer simulations by Cinacchi and Gaetani on shorter rods and for smaller box sizes [37].

For values of $L_0/L_p > 0.1$ we find a direct transition from the nematic to the smectic B phase, *i.e.*, the smectic A phase disappears for large enough flexibilities. We notice that the transitions between the nematic and the smectic B, the smectic A and the smectic B, and the smectic B and the crystal phase are much less sensitive to changes in particle flexibility, and in fact also to variations in the aspect ratio. The smectic A phase is more stable for larger aspect ratios and present in the phase diagram all flexibilities probed for the aspect ratio $L_0/D = 10.77$. The transition from the smectic A or nematic to the smectic B, and that from

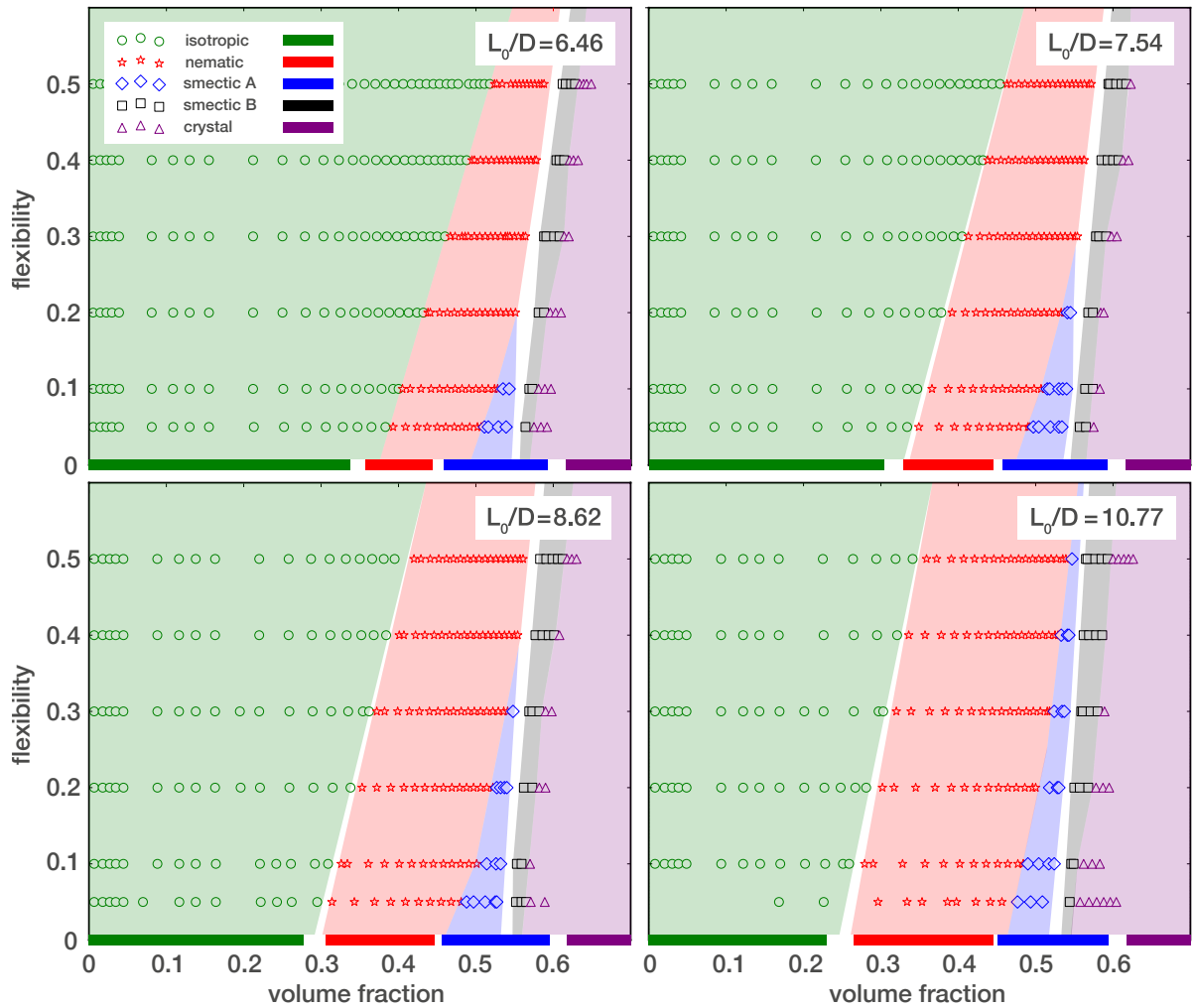


Figure 3.5: Phase diagrams as a function of the volume fraction ϕ and flexibility L_0/L_p for rods with aspect ratios $L_0/D = 6.46, 7.54, 8.62,$ and 10.77 . Indicated are the isotropic phase (green circles), the nematic phase (red stars), the smectic A phase (blue diamonds), the smectic B phase (black squares), and the crystal phase (purple triangles). Corresponding background colours are added to aid identifying the various phases. The isotropic-nematic and the nematic-smectic A phase transitions shift to higher volume fractions with increasing degree of flexibility. Furthermore, the smectic A phase disappears above a critical aspect-ratio, dependent degree of flexibility. The smectic A-smectic B or nematic-smectic B and smectic B-crystal phase transitions shift to larger volume fractions with increasing degree of flexibility albeit that the effect is relatively weak. The bars placed at zero flexibility indicate the simulation results of Bolhuis and Frenkel for infinitely rigid, hard spherocylinders for comparison [25].

the smectic B to the crystal phase, are only very weakly dependent on the aspect ratio and bending flexibility of the particles. This is not entirely unexpected, on the one hand because the particles in these dense phases are almost perfectly aligned, and on the other hand because the Odijk deflection length $\lambda_{\text{Odijk}} = L_p \langle \theta^2 \rangle$ turns out to be of the order the width of the particles in those phases. This implies that bending modes with smaller wavelengths cannot be suppressed and that in this limit bending flexibility should be unimportant [20]. Practically, this is true if the degree of alignment of particles, given by the nematic order parameter S , is larger than $1-(3D)/(2L_p)$. This happens to be the case for the smectic B and crystal phases for the range of flexibilities that we cover.

Our simulation results are consistent with those of Bolhuis and Frenkel for rigid, hard spherocylinders [25], represented in Figure 3.5 by the bars placed at zero flexibility ($L_0/L_p \rightarrow 0$). The agreement is even quantitative for less ordered phases whilst for the highly ordered phases the phase transitions in Bolhuis and Frenkel's simulations shift to larger concentrations compared to ours. There are several explanations for this. First, our rod-like chains are slightly compressible. As we shall see in the next section, excluded-volume interactions cause the chains to compress in particular in the phases where free volume become scarce, so in the denser phases. Second, our particles interact through a soft-core interaction while the rigid rods of Ref. [25] interact via a hard-core potential. Third, our simulation box is much larger than that of 1997 study of Bolhuis and Frenkel. Their particle number was at most 600 whilst in our case it is 4608, suggesting that finite size effects might also play a role in discrepancy.

Regarding the order of the transitions, we can only confirm that the transition from the nematic or the smectic A to the smectic B phase is most definitely of first order: we observe a clear jump in the density at the pressure where the transition takes place (results not shown). We find the isotropic-to-nematic transition to be weakly first order, if at all, but it seems to become more strongly first order with increasing aspect ratio, to shift to lower concentrations and generally to become more stable. This is in line with the computer simulations of Bolhuis and Frenkel [25]. For the other transitions, we find that, if there are jumps, we do not have the resolution to observe them. The experiments of, *e.g.*, Grelet *et al.* on aqueous dispersions of fd virus particles, which have a base aspect ratio of 130 and an effective one of about 30, accounting for the electric double layer of the particles, indicate that the nematic-to-smectic A transition is first order [26, 27, 33]. The order of the transition from smectic A to smectic B for fd virus remains unclear. Fd virus does not transition from smectic B to crystal but to a columnar phase [26, 27]. We hypothesise that the large aspect ratio of the viruses particles somehow stabilises the columnar phase. Indeed, end grafted polymers onto the surface of the viruses make the effective aspect ratio smaller and these

do not seem to support columnar phase [28].

Having discussed the macroscopic (thermodynamic) properties of our particles, we next investigate in more depth how the particles and the structure of the more ordered phases respond to particle length and flexibility. Interestingly, we find that the layer spacing in the smectic A phase may increase or decrease with increasing concentration depending on flexibility and aspect ratio of the chain. This increase of the layer spacing with increasing density is counter intuitive but, as we shall see next, is somehow connected with the layer spacing.

3.4 Microstructure

Our first probe of the microscopic structure of the various phases is the actual contour length of the chains relative to the unperturbed contour length. This is important because our particles are not only flexible but also slightly compressible. Hence, we expect that with increasing particle density they should become shorter in order to accommodate a decreasing free volume. This can be seen as a drawback of our model particles but in fact allows us to address the question to what extent particle flexibility impacts upon the excluded volume in the isotropic phase, and, *vice versa* if and how excluded volume interactions impact upon the effective particle bending flexibility.

In Figure 3.6a, the contour length $\langle L \rangle$ is scaled to the reference contour length L_0 for the aspect ratio $L_0/D = 8.62$ as a function of the volume fraction and the flexibility. The contour length decreases with increasing volume fraction in the isotropic phase. This decrease does not depend on particle flexibility, suggesting that volume exclusion in the isotropic phase is an invariant of the particle flexibility, as has been presumed in the past [1, 22, 62, 63, 67]. We observe a small but sudden increase of the contour length at the isotropic-nematic transition, except for the most flexible chains for which the transition seems to become either second or very weakly first order. (We note that both the insensitivity of the excluded volume to chain flexibility in the isotropic phase and the lengthening of the rods in crossing over to the nematic phase was observed by Wilson, using a very different flexibility model in his simulations [35].)

Arguably, the reason for this jump is an increased free volume caused by the alignment of the particles in the nematic phase [1]. This confirms that the transition is first order albeit more weakly so for the more flexible chains. In the nematic phase, the contour length decreases with increasing concentration, again because of the decrease in free volume with increasing concentration. A much stronger jump we find on going from the nematic or smectic A to the smectic B phase. Simple second virial calculations presented in the Appendix 3.5 confirms

the observed trends for the isotropic and nematic phases, explaining also the jump in length.

In Figure 3.6b, the end-to-end length $\langle L_{\text{ete}} \rangle$ is scaled to the measured contour length $\langle L \rangle$ for aspect ratio $L_0/D = 8.62$ as a function of the volume fraction and the flexibility. In the isotropic phase, this end-to-end length apparently depends only on the ratio L_0/L_p . It depends weakly on the concentration except for the most flexible chains and then only near the isotropic-to-nematic phase transition. This we argue is again caused by the excluded-volume interactions not being affected by particle flexibility. Our measured values for the relative end-to-end length are in very good agreement with prediction given by the worm-like chain model, also indicated in the figure. This confirms that our estimate of the persistence length for our model chains is accurate. In the liquid crystalline phases the end-to-end distance does depend on the concentration and more so the more flexible the particles. This can straightforwardly be understood by realising that a combination of persistence and the molecular ordering field attenuates the bending fluctuations [20, 35]. The latter becomes stronger the larger the particle density. The same is true for the remaining phase transitions as in fact we already alluded to in the previous section.

Perhaps the most interesting structural feature is how the average smectic layer thickness depends on the contour length and persistence length of the particles, that we calculate from the recipe of Ref [54]. In practice, the layer thickness corresponds to the layer height (approximately the rod length) plus the spacing between layers. This is shown in Figure 3.7. For all cases, we find that transitioning from the smectic A to the smectic B phase, the layer spacing *increases*. We speculate that this is due to the larger degree of in-layer packing possible in the more strongly ordered smectic B phase. In essence, this is caused by an increase in free volume. Depending on the aspect ratio and flexibility, we observe that the layer spacing in the smectic A phase itself may in- or decrease with increasing concentration. This is not so for the smectic B and crystalline phases. It seems that in the smectic A phase, increasing the particle density may translate into a more or less proportional increase in in-layer density. If the in-layer density increases more strongly than the average density, then the layer spacing must increase. Because of the appreciable scatter in the data, we have not been able to find a clear trend. We also have no explanation for this phenomenon.

We notice that measurements of the concentration dependence of the layer thickness of smectic A and smectic B phases of the fd virus show approximately linear decrease of the layer spacing with increasing concentration [27]. This indeed is what we obtain for our longest particles. The jumps in layer spacing that we find at the smectic A-to-smectic B phase transition are not observed in the experiments on fd viruses. In addition, the actual layer spacings scaled to particle

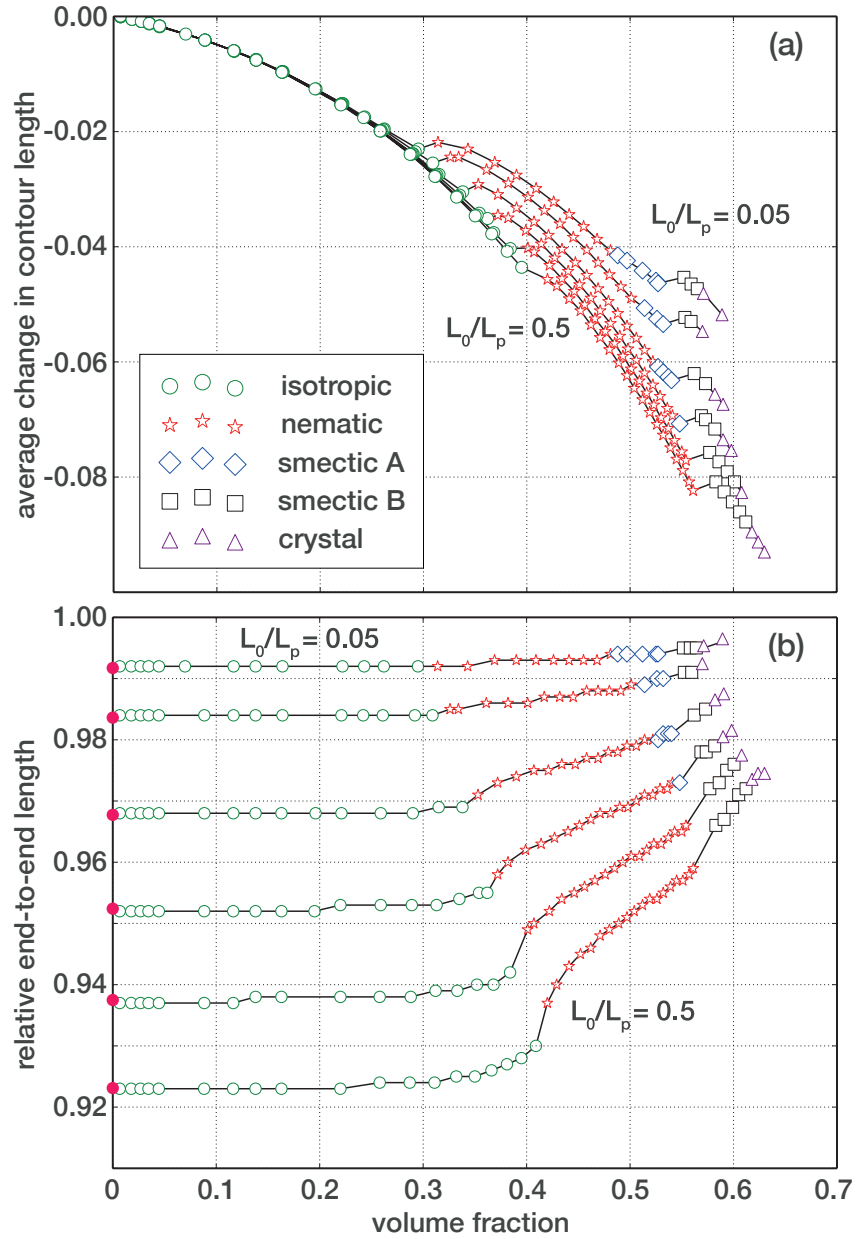


Figure 3.6: (a) The average change in contour length of the chains $(\langle L \rangle - L_0)/L_0$ as a function of the volume fraction ϕ for various aspect ratio $L_0/D = 8.62$. The symbols are defined in Figure 3.5. (b) The compression and jumps in length are explained in the main text. The relative end-to-end length $\langle L_{ete} \rangle / \langle L \rangle$ as a function of the volume fraction ϕ for aspect ratio $L_0/D = 8.62$. Filled circles in magenta represent the prediction for the worm-like chain model.

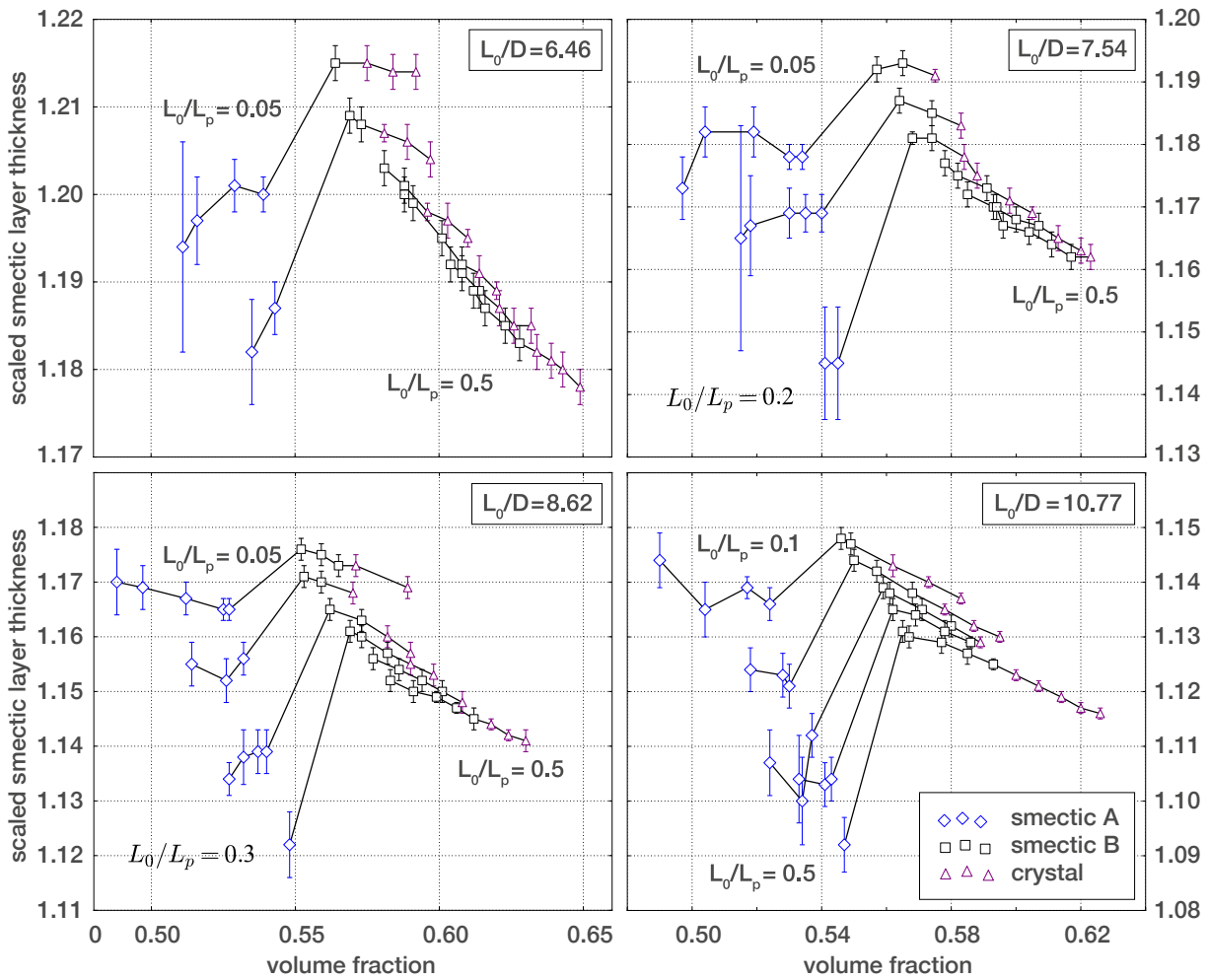


Figure 3.7: The scaled smectic layer thickness $d/\langle L \rangle$ versus density ϕ for various aspect ratios L_0/D . We calculate the layer thickness using the recipe of Ref [54]. In practice, the layer thickness corresponds to the layer height (rod length) plus to the spacing between layers. The symbols are introduced in Figure 3.5. The smectic layer thickness is scaled to the measured average contour length of the particles $\langle L \rangle$ at that volume fraction. Note the sizeable jump in the layer thickness at the smectic A-to-smectic B phase transition. Furthermore, the layer thickness decreases as a function of the volume fraction in for the smectic B and crystal phases. For the smectic A phase, the relation between layer thickness behaviour and particle density depending on the aspect ratio and flexibility.

lengths are also smaller for fd viruses than for the particles in our simulations. On the other hand, we should not expect quantitative agreement with measurements on fd virus solutions on account of their much larger aspect ratio.

3.5 Discussion and conclusions

We perform molecular dynamics simulations to study the influence of flexibility and aspect ratio on the phase behaviour of purely repulsive, rod-like particles. Our particles have aspect ratios between 6 and 11, and ratios of the contour length over the persistence length between 0.05 and 0.5, *i.e.*, we cover the range from very stiff to slightly flexible particles. By measuring the nematic, smectic and bond-order parameters and analysing correlation functions, we are able to distinguish five different phases. In order of increasing volume fraction these include isotropic, nematic, smectic A and B, and crystal phases. Of those phases we probe the structure of the particles and their arrangement, in particular in the smectic and crystalline phases.

In agreement with theoretical predictions and previous simulations, we conclude that the isotropic-nematic and nematic-smectic A phase transitions are sensitive functions of the aspect ratio and the flexibility of the particles. For the former, the larger the aspect ratio, the lower the volume fraction at the transition. For the former and the latter, the larger the flexibility, the larger the volume fraction at the transition. In fact, the smectic A phase disappears for sufficiently large ratio of the contour length over the persistence length, which is a measure for the bending flexibility of the particles. The transitions to the other, more highly ordered phases we find to be much less influenced by both the aspect ratio and the flexibility of the particles.

On increasing the concentration and going from the isotropic phase through the various liquid-crystalline phases to the crystal phase, we find that the end-to-end distance of the particles increasingly approaches their contour length. This is not entirely surprising because the more strongly ordered the phase, the more bending fluctuations are suppressed. In fact, we find, at least for our model bead-chain particles, that bending fluctuations are essentially completely suppressed in smectic B and crystalline phases, explaining the insensitivity of their stability to the persistence length. In other words, the particles in those phases are stretched to their contour length and resemble rigid rods.

The layer spacings that we find in the smectic A, smectic B, and crystal phases exceed the contour length of the particles. Interestingly and counter intuitively, these layer spacings need not decrease with increasing concentration of particles, at least not in the smectic A phase. We find that depending on aspect ratio

and flexibility the spacing may actually increase. This is possible provided the increasing concentration is more than compensated for by an in-layer density increase. We verified this and, not surprisingly, this turns out to be the case in our simulations. We have not been able to pinpoint under what conditions this happens and also do not have an explanation for this phenomenon. Connected to this, we also find that the layer spacing increases upon going from the smectic A to the smectic B phase. This, arguably, is caused by the increase in free volume across the transition. The layer spacing in the smectic B and crystalline phases does behave as expected, that is decrease with increasing concentration.

If we compare our phase diagrams with that of fd viruses in aqueous solution then all phases are reproduced, except for the columnar phase that for fd viruses occurs for concentrations in between the smectic B and crystal phases are stable. Of course, our particles are much shorter and perhaps it is this that suppresses the columnar phase in our simulations. The existence of the columnar phase in dispersions of monodisperse rod-like particles remains somewhat enigmatic and has been subject of a lot of debate in the literature [72]. It has been suggested that explicit modelling of electrostatic interactions stabilises that phase albeit that we cannot exclude the possibility that it is a question of a combination of flexibility and large-enough aspect ratio [31]. The challenge is to reach aspect ratios large enough to investigate this hypothesis.

3.A Onsager theory of linearly compressible hard rods

We observe in our simulations the contraction of the average contour length of the chains for increasing volume fractions on account of their finite extensional compressibility. At the isotropic-nematic phase transition there is also a discontinuity in their contour length, with the particles in the nematic phase being slightly longer. A similar discontinuity occurs at the phase transition towards the smectic-B-crystal phase. These two observations can be rationalised with theoretical predictions we obtain by applying Onsager theory to extensible rods, extending earlier work describing the impact of a compressible polymer grafted to the surface of the rods [24].

To this end we consider a system of N bead-spring chains in a volume V at temperature T . Each rod consists of n beads connected with $n - 1$ harmonic bonds with elastic constant κ and rest length r . Each chain has total rest length $L_0 = (n - 1)r$ and diameter D . The contour length L changes with the concentration of the dimensionless concentration $c = B_2^{\text{iso}}\rho$ with $\rho = N/V$ the number density of particles and $B_2^{\text{iso}} \simeq (\pi/4)L^2D$ the second virial coefficient of the rods in the isotropic phase. The free energy F can be written as a function of

the orientational distribution function $f(\Omega)$ and the compression of the chain $x = L/L_0$:

$$\frac{F[f]}{Nk_B T} = A + \ln c + \sigma[f] + c\rho[f]x^2 + K(x-1)^2, \quad (3.1)$$

where A is a constant, $\ln c$ is the ideal gas distribution, $\sigma[f]$ is the orientation entropy, $c\rho[f]x^2$ is the packing entropy, and $K(x-1)^2$ is related with the potential energy of the harmonic springs with

$$K = \frac{\kappa L_0^2}{2(n-1)k_B T}. \quad (3.2)$$

The third and fourth terms mentioned previously are given by the expressions

$$\sigma[f] = \int f(\Omega) \ln(4\pi f(\Omega)) d\Omega \quad (3.3)$$

and

$$\rho[f] = \frac{4}{\pi} \int |\sin \gamma| f(\Omega) f(\Omega') d\Omega d\Omega', \quad (3.4)$$

where $|\sin \gamma|$ is the angle between the rods with orientation Ω and Ω' .

In the isotropic phase, the normalised distribution function is $f(\Omega) = 1/4\pi$, resulting in an orientational entropy $\sigma[f] = 0$ and a packing entropy $\rho[f] = 1$. The free energy for the isotropic state becomes

$$\frac{F^{\text{iso}}}{Nk_B T} = A + \ln c + cx^2 + K(x-1)^2. \quad (3.5)$$

The equilibrium condition for x , $\frac{\partial}{\partial x} \left[\frac{F^{\text{iso}}}{Nk_B T} \right] = 0$, leads to the compression in the isotropic phase

$$x^{\text{iso}} = \frac{K}{c + K}. \quad (3.6)$$

For the nematic phase, we follow a similar procedure as Odijk [21]. We assume the orientational distribution function to be Gaussian and obey cylindrical and inversion symmetry:

$$f(\theta) = \begin{cases} \alpha/4\pi \exp(-\alpha\theta^2/2), & \text{if } 0 \leq \theta \leq \pi/2 \\ \alpha/4\pi \exp(-\alpha(\pi-\theta)^2/2), & \text{if } \pi/2 < \theta \leq \pi \end{cases}, \quad (3.7)$$

where the normalisation is only accurate for $\alpha \gg 1$. For this distribution we have for the orientational entropy $\sigma[f] \sim \ln \alpha - 1$ and for packing entropy $\rho[f] \sim 4/\sqrt{\alpha\pi}$ [67]. The free energy for the nematic state is then

$$\frac{F^{\text{nem}}}{Nk_B T} = A + \ln c + \ln \alpha - 1 + \frac{4cx^2}{\sqrt{\alpha\pi}} + K(x-1)^2. \quad (3.8)$$

From this expression we find equilibrium values $\alpha = 4c^2 x^4/\pi$ and

$$x^{\text{nem}} = \frac{1}{2} + \sqrt{\frac{1}{4} - \frac{2}{K}}. \quad (3.9)$$

For x^{nem} there is also a negative root solution that we ignore for it being physically unrealistic. For $K \rightarrow \infty$, $x^{\text{nem}} = 1$. For $K < 8$, the compression becomes imaginary, meaning that the nematic phase becomes unstable.

Equations 3.6 and 3.9 describe the behaviour of the mean length of our chains in the isotropic and nematic phases. We now calculate the coexistence concentration. Coexistence between two phases occurs when the osmotic pressure $\Pi = -(\partial F/\partial V)_{N,T}$ and chemical potential $\mu = (\partial F/\partial N)_{V,T}$ are equal for both states, $\mu^{\text{iso}} = \mu^{\text{nem}}$ and $\Pi^{\text{iso}} = \Pi^{\text{nem}}$. From these equations we calculate the coexistence concentrations for the isotropic c^{iso} and the nematic phase c^{nem} .

We now add flexibility to our model to study how it affects the discontinuity in the average length of the chains at the isotropic-nematic phase transition. Our starting point is the expression derived by Odijk [20, 21] are inspired by the work by Khokhlov and Semenov [62, 63] describing the orientational entropy for semi-flexible particles, $L/L_p \ll 1$. For the isotropic phase there is no change of the orientational entropy. For the nematic phase there is the extra term $L_0 \alpha x/4L_p$, then the orientational entropy is

$$\sigma = \ln \alpha - 1 + \frac{L_0 \alpha x}{4L_p}. \quad (3.10)$$

With this new orientational entropy, the free energy for the nematic phase becomes

$$\frac{F^{\text{nem}}}{Nk_B T} = A + \ln c + \ln \alpha - 1 + \frac{L_0 \alpha x}{4L_p} + \frac{4cx^2}{\sqrt{\alpha\pi}} + K(x-1)^2. \quad (3.11)$$

Solving the equilibrium value for α and x we obtain the compression of the chain as a function of the dimensionless concentration. These and the coexistence concentrations are calculated numerically.

Finally, we compare the simulations with the model calculations. We specifically perform the calculations for $K = 150$ and for flexibilities $L_0/L_p = 0, 0.05, 0.1, 0.2, 0.3, 0.4$ and 0.5 , as can be seen in Figure 3.8. These values coincide with the simulated values, except $L_0/L_p = 0$, the rigid rod limit that we did not simulate. We find similarities between these results and our simulation results. First, the decrease of the average length of the chain with increasing concentration for both isotropic and nematic phase. Second, the discontinuity in an average length decreases with the increase of the flexibility. There are some differences though, such as the curvature of the lines, straight for our calculations but curved for our simulations. This may be due to one second virial approximation which is not expected to be accurate for rods of aspect ratio below 100 [67].

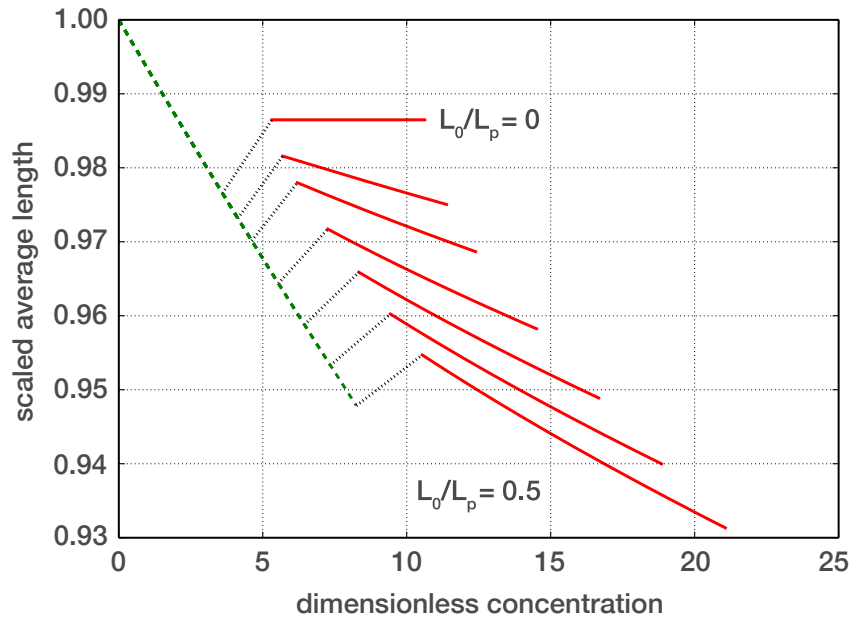


Figure 3.8: Scaled average length of the chains $x = L/L_0$ as a function of the dimensionless concentration c , for $K = 150$ and flexibilities $L_0/L_P = 0, 0.05, 0.1, 0.2, 0.3, 0.4$ and 0.5 . The green dashed line represents the isotropic phase, the red lines represent the nematic phase, and the black dots connect the points of coexistence.

Acknowledgments

We thank Eric Grelet for critical reading of the manuscript of the article that is the base for this chapter.

Chapter 4

Self-organisation of tip-functionalised elongated particles

Weakly attractive interactions between the tips of rod-like colloidal particles affect their liquid-crystal phase behaviour due to a subtle interplay between enthalpy and entropy. In this chapter, we employ molecular dynamics simulations on semi-flexible, repulsive bead-spring chains of which one of the two end beads attract each other. We calculate the phase diagram as a function of both the volume fraction of the chains and the strength of the attractive potential. We identify a large number of phases that include isotropic, nematic, smectic A, smectic B and crystalline states. For tip attraction energies lower than the thermal energy, our results are qualitatively consistent with experimental findings: we find that an increase of the attraction strength shifts the nematic to smectic A phase transition to lower volume fractions, with only minor effect on the stability of the other phases. For sufficiently strong tip attraction, the nematic phase disappears completely, in addition leading to the destabilisation of the isotropic phase. In order to better understand the underlying physics of these phenomena, we also investigate the clustering of the particles at their attractive tips and the effective molecular field experienced by the particles in the smectic A phase. Based on these results, we argue that the clustering of the tips only affects the phase stability if lamellar structures (“micelles”) are formed. We find that an increase of the attraction strength increases the degree of order in the layered phases. Interestingly, we also find evidence for the existence of an anti-ferroelectric smectic A phase transition induced by the interaction between the tips. A simple Maier-Saupe-McMillan model confirms our findings.

4.1 Introduction

Elongated colloidal particles form additional phases under conditions in between those where the well-known isotropic (disordered) and crystalline (ordered) phases are found [1–3]. The particles are invariably aligned but have no or only partial (short-range or quasi long-range) positional order in these phases and, for this reason, are called liquid-crystalline phases. The phase transitions are driven primarily by entropy, as theoretical, simulation, and experimental studies have shown [20–24, 26–28]. More recently, the use of selective surface functionalisation of elongated colloidal particles has opened up an interesting novel path of investigation, allowing us to modify the self-assembled liquid-crystalline phases and/or to manipulate their stabilities [73]. For example, such particles have been explored in the synthesis of functional materials including nanowires and batteries [7–10], and in the investigation of specific structure formation such as multipods, tubes, and bottle brushes [11–13, 74]. Nevertheless, studies concerning how a relatively weak and highly local surface modification affects the phase sequences for a wide range of concentrations, as well as particles characteristics such as aspect ratio and bending flexibility, remain scarce.

A good example of functionalised elongated colloids is the recent work by Repula *et al.* using filamentous M13 virus particles [42], which measure 1 μm in length, 7 nm in width and which have persistence length of about 3 μm . In their experiments, the M13 virus has its terminal (P3) protein modified, allowing for the attachment of red dye molecules to one of the tips of these polar particles. The procedure results in a controllable, attractive, single-end local interaction in what was previously a purely repulsive rod. From previous work, we know that the complete phase sequence of suspensions of such viruses comprises isotropic, nematic, smectic A, smectic B, columnar, and crystalline phases [27]. Interestingly, the surface modification seems to affect only one of various phase transitions: the nematic-smectic A phase transition is influenced by the number of red dye molecules grafted to the virus tip, stabilising the latter phase. For the purpose of understanding the reason for this, we investigate how a weakly attractive tip modifies the liquid crystalline behaviour of repulsive, semi-flexible rod-like particles using computer simulations.

In this chapter, we present the calculated phase diagram of such particles as a function of both the concentration and the attraction strength between tips, demarcating two regimes. In the first regime, in which the strength of the tip-tip interaction corresponds to energies lower than or comparable to the thermal energy, our results are qualitatively consistent with the experimental findings [42]. In the second regime, corresponding to slightly stronger attractive energies, we find interesting effects including the complete suppression of the nematic

phase and the destabilisation of the isotropic phase. Additionally, we address in this paper several other topics regarding the microstructure of the phases, such as: (1) qualitative and quantitative aspects of the supramolecular aggregation due to the presence of the attractive tips in the various phases; (2) the response of the interlayer distance and the molecular field for the various concentrations and attraction strengths between the tips in the smectic and crystalline phases; (3) evidence for the existence of an anti-ferroelectric smectic A phase induced by the interaction between the ends.

Related to the anti-ferroelectric smectic A phase, note that the bilayer structure is anti-ferroelectric in 1-dimension. In 2-dimensions or, in other words, within a smectic layer, the structure is ferroelectric. We make an analogy with ferroelectricity instead of ferromagnetism for historical reasons. The term was previously employed in the literature of liquid crystals, referring to compounds that form bilayer structures in the smectic A phase [75]. The term (anti-)ferromagnetism is usually restricted to magnetic phenomena, while (anti-)ferroelectricity is more liberally used, referring to various types of polar phenomena [76]. We note in this context that the existence of an anti-ferroelectric phase of end-functionalised hard rods with double periodicity was anticipated long ago by Jackson and co-workers by means of density functional theoretical calculations [77]. We also present a simple model based on the Maier-Saupe-McMillan theory that describes the phase transition within the smectic A phase and that qualitatively explains our simulation results.

The remainder of this paper is structured as follows. We describe the methods and model particle employed in our computer simulations as well as the data analysis procedure in Section 4.2. In Sections 4.3 and 4.4, we present the results followed by a discussion. These sections are devoted to the phase behaviour and the microstructure of the phases. In Section 4.5, we compare our results with experimental findings. In Section 4.6, we present our most important conclusions. Finally, in the Appendix 4.6, we present our Maier-Saupe-McMillan theory for end-functionalised, perfectly parallel rods.

4.2 Methods and analysis

Model particles - We model the semi-flexible rod-like particles as the bead-spring chains of b overlapping beads of diameter D and mass m , similarly to the particles described in details in Chapter 2. Nevertheless, here, the b -th bead in a chain is not identical to the other beads. The single-end attractive interaction is modelled using a second type of bead at one of the ends of every chain, represented in red in the snapshots of our simulations (Figure 4.3). These beads interact with

each other via the full Lennard-Jones potential, $U_{LJ} = 4\epsilon[(R/D)^{-12} - (R/D)^{-6}]$, with various values of $\epsilon \geq 0$. Notice that because only one end of every chain is sticky, the chains are polar and lack inversion symmetry. Also for the particles employed in this study, we refer to the mean aspect ratio at very low densities, L_0/D , to characterise our particles. We quantify the particles' flexibility by the ratio of the dilute-solution contour length and the persistence length, L_0/L_p . Simulations are performed for chains of aspect ratio $L_0/D = 10.77$ and flexibility $L_0/L_p = 0.3$. The aspect ratio chosen gives us a reasonable compromise between equilibration time and particle number in simulations at high concentrations. The flexibility matches the one of the experimental model particles mentioned earlier [42]. More details are given in Section 4.3. We perform preliminary simulations on somewhat shorter and stiffer chains of $L_0/D = 6.46$ and $L_0/L_p = 0.1$ (results not shown). The only impact aspect ratio seems to have is that the volume fractions at which the various phase transitions take place decreases as the aspect ratio increases, as in fact expected from the previous study presented in Chapter 3. The same is true for the effect of bending flexibility, which increases the volume fraction at which the various phase transitions occur. Hence, we focus our presentation in this work on results for the longer particles.

Molecular dynamics (MD) - We perform MD computer simulations using the Nosé-Hoover thermo- and barostat on 4608 bead-spring chains in a box in order to obtain structural properties of the tip attractive rod-like particles, also as described in Chapter 2. Our simulations run for 20000 time units that, in physical quantities, correspond to $\sqrt{mD^2/\epsilon_0}$. We employ time steps of 10^{-3} in these units, in other words, a total of 2×10^7 time steps. We save configurations every 2×10^5 time steps. The results we present in this paper are from expansion simulation runs starting from a crystal-like configuration, which we describe in more detail in the paragraph below. The discussion relative to the compression runs for the particles without attractive end tips for all phase transitions identified is presented in the previous Chapter.

Initial configurations - For the expansion simulation runs, we consider diverse variations of the crystal-like initial configurations corresponding to how our polar particles are oriented. In all configurations, the particles are organised in 16 AAA stacked layers. In each layer, particles are organised in a hexagonal lattice and aligned parallel to z-direction. For this reason, if particles in our simulations have a preferential direction, which is described by the director \mathbf{n} , this is usually approximately parallel to the z-direction, $\mathbf{n} \parallel \hat{\mathbf{z}}$. In the first type of initial configuration, all attractive beads are in the upper tip of the particle. Even though our simulation time is relatively long, it is not sufficiently long to equilibrate the system at all concentrations. In other words, in the more condensed phases, we do not reach 1:1 chains up and down relative to the director. In the second type

of initial configuration investigated, the attractive beads alternate between the upper and the bottom tip within the same layer. In the third type of initial configuration tested, half of the layers have the attractive groups in the upper tip and the other half have the particles' attractive bead in the bottom tip. These layers alternate in a way that this third configuration has a bilayer type of structure. The latter two initial configurations result in structures with fewer or no defects at all. Hence, in the following sections, we present the results from the simulations in which the third type of initial configuration is used. See in Figure 4.1 the schematic representation of the three initial configurations followed of a snapshot from the preliminary simulations (in which our particles have an aspect ratio $L_0/D = 6.46$ and a flexibility $L_0/L_p = 0.1$) after 20 000 000 timesteps at approximately constant volume fraction $\phi = 0.52$ (at a fixed pressure $1.7 \epsilon/D^3$) for the attraction strength of $0.6 k_B T$.

Phase classification - Our equilibrium configurations are classified using order parameters and correlation functions. The liquid-crystalline phases we first distinguish from the isotropic phase by quantifying the degree of alignment of the particles through the usual nematic order parameter. A second order parameter quantifies the organisation of the particles in layers. If layers are not formed, we have either a nematic or a columnar phase. If layers are formed, we have either smectic or crystalline phases. A third order parameter quantifies the hexagonal bond order. This procedure, described in detail in Chapter 2, allows us to distinguish between nematic and columnar, and between the smectic A and the smectic B and crystal phases. This final classification is possible by studying the correlation of the bond order (measuring two-dimensional hexagonal order) and the pair correlation function (probing radial in-plane positional order). Using this procedure, we are able to distinguish between all known phases of the fd virus suspensions, mentioned in Section 4.1. We also identify two distinct smectic and crystalline phases due to the attraction between the functionalised tips. The procedure to distinguish between them we describe below in the paragraph dealing with the anti-ferroelectric phase transition.

Aggregation statistics - Further analysis is required in order to study the structure of supramolecular assemblies in all phases, in particular in the layered phases where the spacing is expected to be influenced by (i) the attraction strength between tip beads and (ii) the concentration of the particles. We quantify the aggregation of the particles by focusing on cluster sizes. By *cluster* we refer to groups of attractive tip beads that are spatially close or connected by a bead satisfying this criterion. We arbitrarily choose a distance r_c . The first choice for r_c is $1.24 D$. This value corresponds to the second root of a parabola, whose minimum is at the minimum of the Lennard-Jones potential and the first root coincides with the root of this potential. If pairs of attractive tip bead are closer

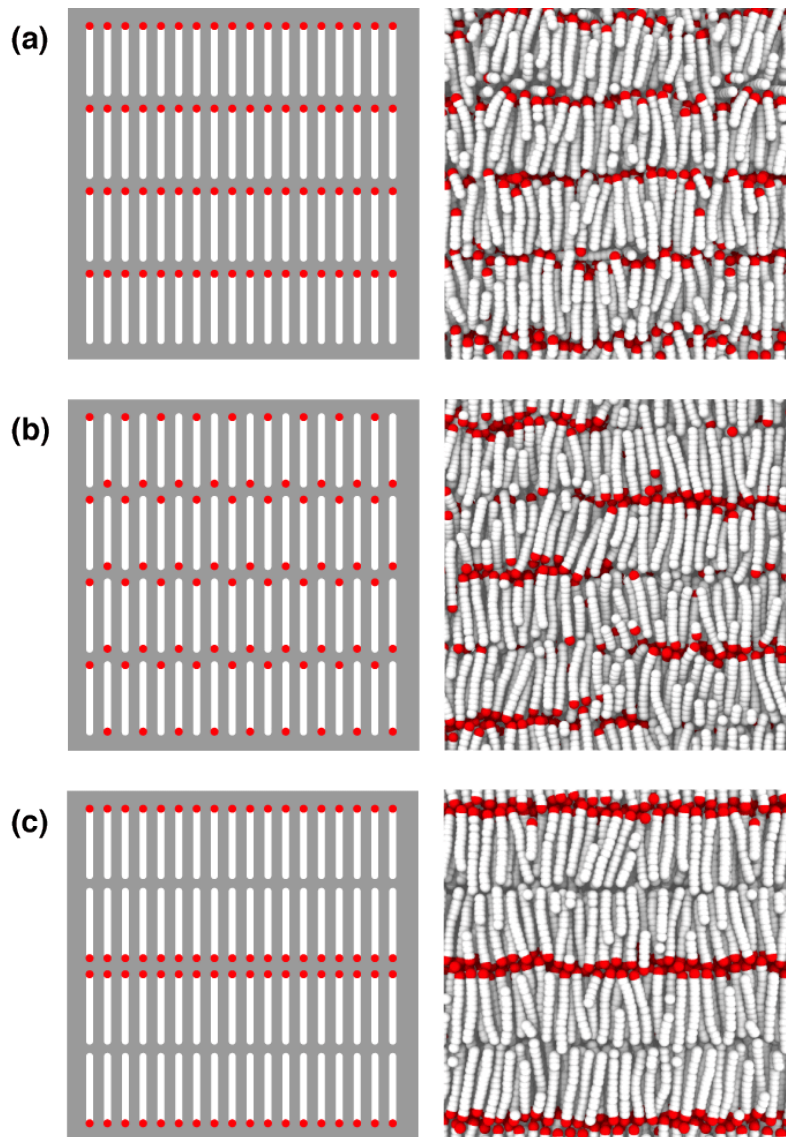


Figure 4.1: Schematic representation of the initial configurations and snapshots of resulting configurations after 20 000 000 timesteps of simulations starting from each of them at approximately constant volume fraction $\phi = 0.52$ (at a fixed pressure $1.7 \epsilon / D^3$) for the attraction strength of $0.6 k_B T$. In the initial configuration in (a), all particles have the same orientations, in (b), particles alternate orientation within the same layer, and in (c), all particles have the same orientation within the layer, but the orientation alternate from consecutive layers.

than this distance, we consider them as belonging to the same group. Note that not all beads in a group need to be closer than r_c , as some can be connected indirectly via other attractive beads, as represented in the inset of Figure 4.4, in Section 4.4.

Anti-ferroelectric phases - Due to the polarity of our molecules, we identify two types of organisation in the layered phases: one in which the attractive tip beads are present in roughly equal numbers in every interlayer spacing and another in which the attractive tip beads are mostly present in every other interlayer spacing, creating a bilayer structure with double the periodicity of that of the layers. In order to pinpoint the transition between these two states within our phase diagram, we project the particle orientations on a vector along the director. We define the orientation vector of the particles connecting the repulsive end bead to the attractive end bead. The two extreme situations are: (1) the rods are in a bilayer type of configuration and, as a result, all particles within a layer are either parallel or anti-parallel to a vector along the director; (2) the ratio between parallel and anti-parallel particles to the same vector within a layer is 1:1. For these cases, if the fractions of particles in a particular orientation in even and odd layers are respectively $f = 0$ and 0.5, then the anti-ferroelectric order parameter is defined as $\delta = 1-2f$. We choose the value $\delta = 0.5$ as a criterion to classify the phases as the usual smectic A ($\delta < 0.5$) or the anti-ferroelectric smectic A_2 ($\delta \geq 0.5$). The same procedure is applicable to the smectic B and crystalline phases, whose corresponding anti-ferroelectric phases are denoted smectic B_2 and crystalline₂ phases. From snapshots of our simulations, we find that even at the lowest attraction strength investigated, the smectic B and crystalline phases are anti-ferroelectric.

Layer thickness - We utilise two different procedures to calculate the inter-layer distance in the layered phases. As a first procedure, we take the value that maximises the Fourier component of the normalised distribution of centre of masses along the director [54]. This does not differentiate between the layers regarding the fraction of particles pointing up. Because there are two types of smectic A phase, we expect that the interlayer distance is different if in their interface there are mostly attractive or repulsive tips. In order to measure this difference in the bi-layered phase, we plot the histogram of counts of the centre of mass for each (arbitrary) interval of positions along the director. In the layered phases, the distribution of the centres of mass of the particles along the director is peaked around the centres of the layers. Hence, we fit a Gaussian function to each counting of the centre of mass divided by the maximum count, $g_j(z) = e^{-b_j(z-a_j)^2}$, where e is the usual Euler constant. The parameter b_j is related to the standard deviation s of the Gaussian function by $b_j = 1/2s^2$ and describes how well-ordered the layers are. The centre of the Gaussian distribution

a_j corresponds to the position of the j -th layer along the director. The distance between two consecutive layers is then calculated as $\lambda_j = a_{j+1} - a_j$. Beyond the anti-ferroelectric transition, the values of λ_j with odd j correspond to the distance between layers in which there are more attractive tips than tails facing each other. For this reason, the average value λ_{odd} is expected to be lower than λ_{even} beyond the anti-ferroelectric transition; λ_{even} is then the average over the values λ_j with even j and over the equilibrium configurations for a given pressure.

Smectic ordering potential - The smectic ordering potential $\Delta U(z)$ describes the molecular field experienced by each individual particle in the smectic A phase. It is obtained from the distribution of the particles' centres of mass along the z -direction, which corresponds approximately to the director \mathbf{n} , $\rho(z)$. More specifically, the relation $\rho(z) \propto e^{-\Delta U(z)/k_B T}$ holds by virtue of assuming a Boltzmann distribution. We fit this relation to the simulation data to extract $\Delta U(z)$. From the smectic ordering potential, we compare between various attraction strengths and volume fractions how well-defined the layers are and how difficult it is for a particle to hop from layer to layer. We quantify it by measuring the difference between the highest and lowest value of the smectic ordering potential ΔU , which defines the height of the smectic ordering potential $h_{\Delta U}$, for several values of the attraction strength and volume fraction. We also estimate the width of the smectic ordering potential $w_{\Delta U}$ by calculating the full width at half maximum of $\rho(z)$, using the standard deviation s of the gaussian function described in the previous paragraph, giving $w_{\Delta U} = 2\sqrt{2 \ln 2} s$.

4.3 Phase behaviour

We focus attention on the phase behaviour of semi-flexible rod-like particles that have an aspect ratio of $L_0/D = 10.77$ and a flexibility of $L_0/L_p = 0.3$. The flexibility of our model particles matches that of the M13 virus investigated in Reference [42] albeit that the aspect ratio of our particles is considerably shorter by a factor of 10. Actually, the effective aspect ratio of the viruses, accounting for the electric double layer of the M13 particles, is about three times our aspect ratio. We choose to simulate shorter particles, because it enables us to investigate them for a wide range of concentrations, keeping the same number of particles in our simulation box and the total simulation time. In general, as the aspect ratio of the particles is reduced, the phase transitions of their suspensions are shifted to larger volume fractions because the excluded volume interaction is less anisotropic. Still, both experimental and simulation particle models support the same phases except for the columnar phase, which has not yet been observed in particle-based simulations involving monodisperse particles [25, 35, 37, 52]. Therefore, we are

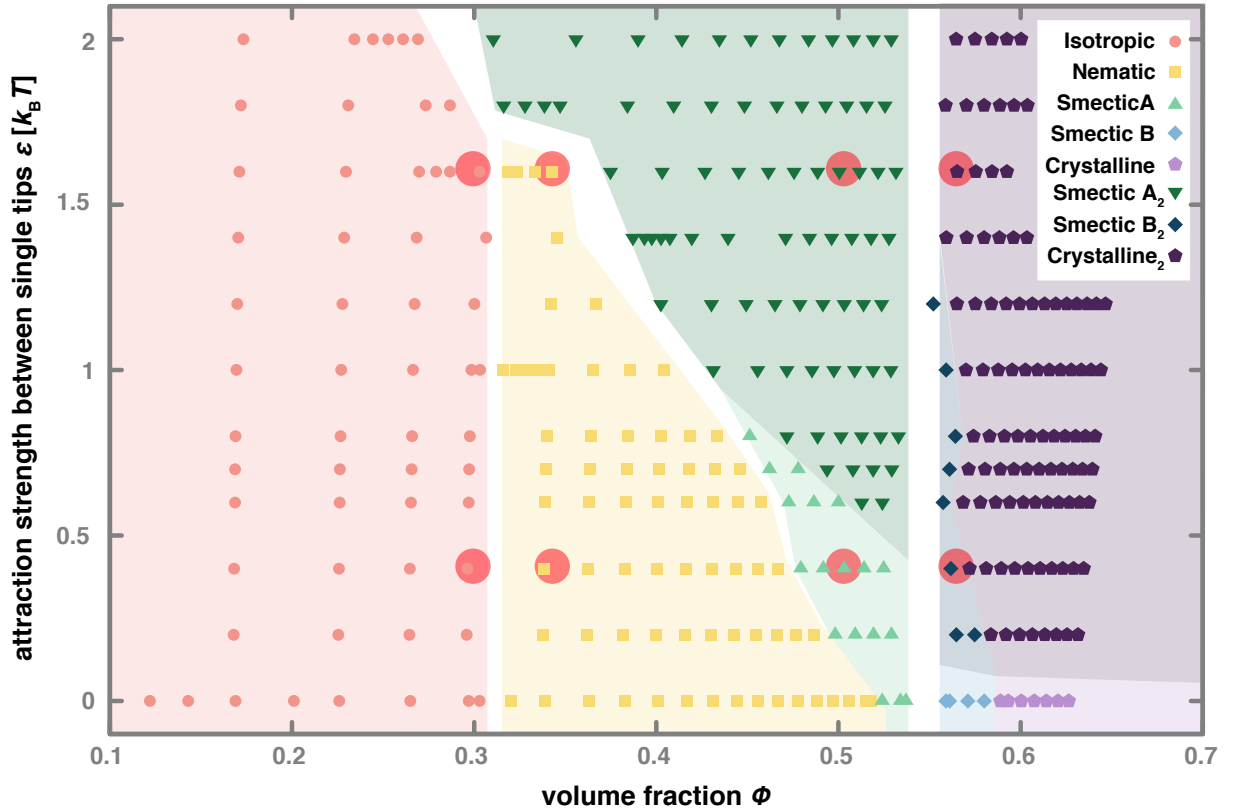


Figure 4.2: Calculated phase diagram of repulsive, rod-like particles that have a single attractive tip as a function of the attraction strength between the end tips (in units of thermal energy) and the volume fraction ϕ . The particles have a base aspect ratio $L_0/D = 10.77$ and flexibility of $L/L_p = 0.3$. (See main text.) The following phases are identified: isotropic (orange circle), nematic (yellow square), smectic A (green triangle up), smectic A₂ (dark green triangle down), smectic B (blue diamond), smectic B₂ (dark blue diamond), crystalline (purple pentagon) and crystalline₂ (dark purple pentagon). Snapshots of the data points highlighted by red circles in the phase diagram are presented in Figure 4.3.

able to compare them in what is our main interest in this paper: the increase of the stability of the smectic A phase at the expense of the nematic phase.

In the phase diagram presented in Figure 4.2, the phase sequence at the zero attraction strength, $\epsilon = 0 k_B T$, is taken from our previous work [52]. See also Chapter 3. In this case, the particles are purely repulsive and have the same total number of beads as the particles with an attractive tip. Note that as they are not equipped with the attractive bead these rods are not polar. For these purely repulsive particles, the phase sequence consists of the following phases from lower to higher volume fractions: isotropic, nematic, smectic A, smectic B, and crystalline phases. From these simulations, we find that the isotropic-to-nematic and the smectic A-to-smectic B phase transitions seem to be of the first order. The smectic B-to-crystalline phase transition appears to be continuous, while the nematic-to-smectic A phase transition is either continuous or weakly first order. In the recent work of Milchev *et al.*, in which very large-scale simulations of semi-flexible particles are performed, the latter transition is continuous [78]. For the model particles described in the methods section, we vary the depth of the attraction well ϵ of the Lennard-Jones potential between the beads representing the functionalised tips of the viruses, that is, the *attraction strength*, from 0.2 to $2 k_B T$. The calculated volume fraction is within the range of approximately 0.1 to 0.7. In order to obtain more resolution in volume fraction near the isotropic-nematic transition, we perform additional simulations for the attraction strengths 1 and $1.6 k_B T$ near the transition. We do likewise for the nematic-smectic A and isotropic-smectic A phase transitions for the attraction strengths 1.4 and $1.8 k_B T$. We separate our discussion of the phase diagram in the next two paragraphs, related to the low- and a medium-energy regime of the single-end, attractive interaction on account of the qualitative difference in behaviour.

Lower attraction strengths - For values of the attraction strength up to about $1 k_B T$, our simulations show that there is no significant change in the isotropic-to-nematic phase transition. Comparing the sequences at 0 and $1 k_B T$, which is the one with more resolution in volume fraction in this regime of attraction strengths, we find that the largest and lowest volume fractions in which these phases are stable in our simulations (corresponding to the coexistence concentrations) coincide. For this reason, the isotropic-to-nematic phase transition remains first order. We find that the nematic phase is destabilised in favour of the smectic A phase and that this phase transition becomes more strongly first order as the strength of the attraction interaction is increased. These findings are consistent with the recent experimental observations on aqueous suspensions of M13 virus [42]. Our most remarkable finding is an anti-ferroelectric phase transition within the smectic A phase. We identify the new smectic A_2 phase, characterised by a bi-layer type structure, in our phase diagram at $0.4 k_B T$ and higher attraction

strengths, depending on the density. Section 4.4 provides more details about the anti-ferroelectric transition, which in our simulations is continuous. There are also anti-ferroelectric smectic B and crystalline phases. In fact, even at the lowest attraction strength investigated, we find only the anti-ferroelectric smectic B₂ and crystalline₂ phase, suggesting that only tiny interaction energies are required to stabilise these. We did not attempt to pinpoint at what low value of ϵ the transition happens for these phases. As for the other phase transitions, we find that there is no significant change in the smectic A or smectic A₂ to smectic B₂ phase transition. Furthermore, the smectic B₂ phase destabilises with increasing value of ϵ and the crystalline₂ phase becomes more stable at lower volume fractions. We understand that the suppression of the smectic B₂ phase is due to the increased ordering of particles due to the sticky end groups, as we shall see below when discussing the changes in the microstructure of the phases with increasing attraction between the tips. Note that, despite the distinct polarity caused by single sticky end, this fundamentally does not allow for macroscopically polar phases as the sticky ends attract each other.

Higher attraction strengths - In order to investigate the effect of larger attraction energies between the end groups, we performed simulations for attraction strengths up to $2 k_B T$. The phase sequence at $1.2 k_B T$ follows the trends described in the previous paragraph. For this reason, the coexistence concentrations (volume fractions) of the nematic and smectic A₂ phases are even lower and the difference between them (the phase gap) becomes larger. For stronger attraction, the smectic B₂ disappears, and as a result the smectic A₂-to-smectic B₂ phase transition is replaced by a smectic A₂-to-crystalline₂ transition. This transition seems to be independent of the attraction strength and the phases have similar coexistence volume fractions as the transition at lower values of the attraction strength. Between attraction strengths 1.6 and $1.8 k_B T$, we find that the nematic phase is completely suppressed in favour of the smectic A₂, thus also affecting the stability of the isotropic phase. Therefore, the phase sequence at the highest attraction strengths 1.8 and $2 k_B T$ consist of only three phases: isotropic, smectic A₂, and crystalline₂. From these results, we find that the isotropic phase may also be further destabilised with increasing attraction strength between the tips. A similar transition between an isotropic and a smectic A phase with additional double periodicity was found in simulations of hinged rods for a model of gapped DNA complexes [79]. These authors dubbed this phase the Sm-fA, where the f stands for folded because the rods are folded at the hinge, creating this additional double periodicity of the position of the hinges in the structure. From the simulations at increased resolution, we are able to conclude that the isotropic-nematic phase gap in volume fraction is about 0.02 for the attraction strength of $1 k_B T$ and only slightly larger than that for $1.6 k_B T$, corresponding to approximately 0.03. There-

fore, the order of this phase transition does not seem to be strongly affected by the attractive end aggregation. On the other hand, the nematic-smectic A_2 , as previously discussed, and isotropic-smectic A phase transitions become more strongly first order with an increase of the attraction strength, as we find from the more detailed sequences at the attraction strengths of 1.4 and $1.8 k_B T$.

The phase diagram presented here compares reasonably well with the phase diagram obtained from the numerical solving of our simple Maier-Saupe-McMillan model for end-functionalized, perfectly parallel rods (Figure 4.15 b). See the Appendix for a discussion. Next, we discuss in more detail the microscopic structure of the various phases. See Section 4.5 for the comparison of our phase diagram with experimental findings.

4.4 Microstructure

In this section, we present the most salient features of the microstructure of the various phases, focusing in particular on those of the smectic A and smectic A_2 phases in order to better understand what drives the anti-ferroelectric phase transition. First, we discuss the qualitative and quantitative changes in the aggregation of the particles with attractive tips. For this purpose, we investigate snapshots as well as the aggregation statistics of the particles in the various phases. Second, we discuss the behaviour of the interlayer distance for the smectic and crystalline phases, as well as their anti-ferroelectric version based on results from the two different analysis procedures described in Section 4.2. Next, we provide more details about the order of the anti-ferroelectric phase transition, presenting the order parameter used for the classification of the smectic A and smectic A_2 phases. Finally, we analyse the stability of the smectic A and smectic A_2 at a constant volume fraction, using the smectic ordering potential for various attraction strengths. For the different phases, we identify the following features.

Clustering of particles - In the next paragraphs, we describe how the aggregation of elongated particles is influenced by the strength of the attractive tips in the various phases. The snapshots in Figure 4.3 represent the aggregation patterns at approximately constant volume fraction ϕ in the isotropic phase at $\phi \sim 0.30$ (a), nematic phase at $\phi \sim 0.38$ (b), smectic A and smectic A_2 phases at $\phi \sim 0.51$ (c), smectic B and crystal phases at $\phi \sim 0.56$ (d). Left to right, each pair of snapshots shows examples of configurations of particles with attraction strengths of 0.4 and $1.6 k_B T$. The snapshots show that the aggregation pattern of the tips is clearly distinct, depending on the attraction strength for particles in the same phase and at the same volume fraction, as we describe in detail in the paragraph below.

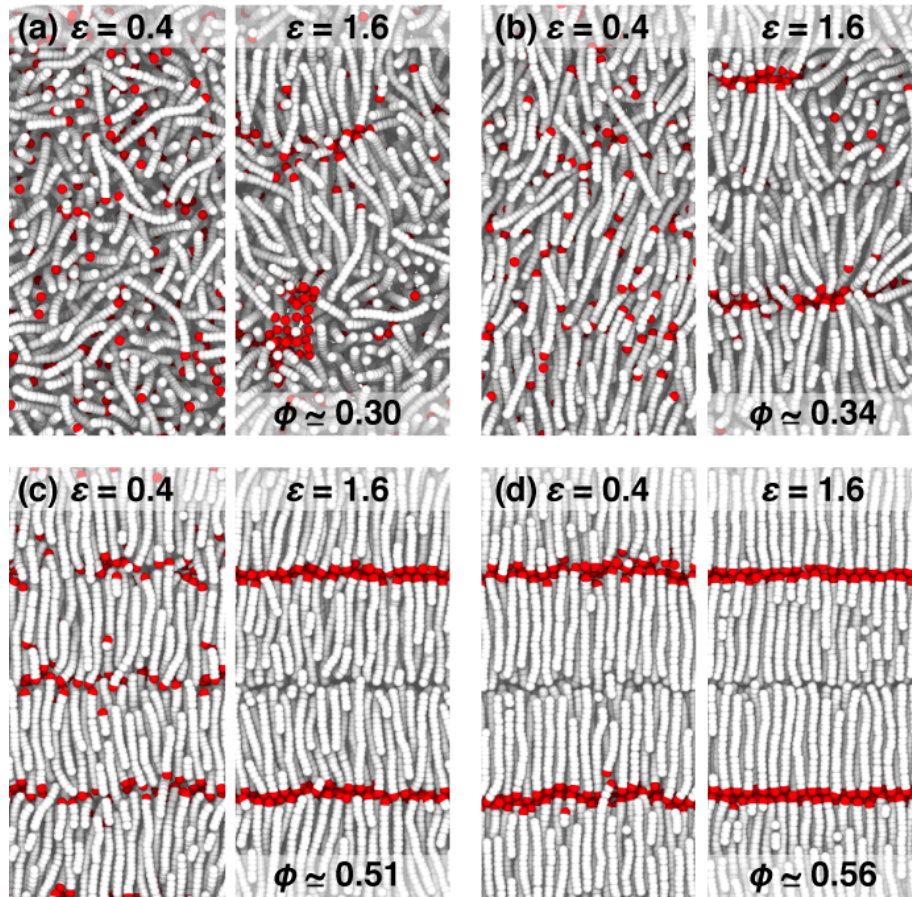


Figure 4.3: Snapshots of the simulations at approximately constant volume fraction ϕ in the (a) isotropic phase at $\phi \simeq 0.30$, (b) nematic phase at $\phi \simeq 0.38$, (c) smectic A and smectic A₂ phases at $\phi \simeq 0.51$, (d) smectic B (left) and crystal phases (right) at $\phi \simeq 0.56$. From left to right, pair of snapshots for each value of the volume fraction are given for attractions strengths of 0.4 and 1.6 $k_B T$. The corresponding data points are highlighted by red circles in the phase diagram in Figure 4.2.

From our phase diagram in Figure 4.2, we find that the isotropic-to-nematic transition is only affected for $\epsilon \geq 1.6 k_B T$. At this attraction strength, lamellar, disk- or inverted-micelle-like structures are formed. These two different aggregation patterns are represented in the snapshots on the right in Figure 4.3 (a) and (b). In Figure 4.3 (a), we find that, overall, the particles have random orientations, as expected for the isotropic phase. The particles aggregated in lamellar structures have similar orientation but the structures themselves have diverse orientations. In Figure 4.3 (b), at attraction strength 1.6 $k_B T$ (right), we note that the alignment of the particles in the nematic phase results in a structure that resembles a highly disordered smectic phase. In view of that we conclude that the formation of such lamellar structures must be the reason that there is a suppression of the nematic phase in favour of the smectic phase. In the snapshots

of Figure 4.3 (c), we compare how particles are organised along the director in the smectic A (left) and the smectic A_2 (right) phases at the same volume fraction. We find that the layers become more well-defined with increasing attraction strength. This is confirmed comparing the snapshots of Figure 4.3 (d) for the smectic B_2 and crystalline₂ phases. The attraction between the tips increases the degree of order of the particles, reducing the stability range of the smectic B_2 phase in favour of the crystalline phase.

We compare these patterns with the corresponding aggregation statistics as a function of the volume fraction in Figure 4.4, where we present (a) the average tip aggregation number for various attraction strengths and (b) the fraction of particles in monomers, dimers, and trimers or larger aggregates for an attraction strength of $0.2 k_B T$. Figure 4.4 (a) shows, as expected, that the average aggregation number increases with increasing attraction strength and with increasing concentration due to mass action [80]. The microstructure therefore changes even in the isotropic phase, although, surprisingly, the isotropic-nematic phase transition is not affected at all. As we infer from the inset in Figure 4.4, the tip clustering is weak at attraction strengths up to $1 k_B T$ in both the isotropic and the nematic phases. For these phases and attraction strengths, the aggregation numbers remain modest even though growth is stronger than a linear increase with the volume fraction. Actually, in these phases the average aggregation number is not larger than 1.3, which means that the tips are mostly monomers. Figure 4.4 (b) confirms this: in both the isotropic and the nematic phases, the fraction of monomers and dimers predominate. The fraction of trimers or larger aggregates surpasses the fraction of dimers only in the smectic A phase and the fraction of monomers in the smectic B_2 phase. This indicates that larger aggregates are formed due to the inherent structure of the phase rather than due to the attraction strength alone. Indeed, part of the clustering is due to the change in the contact value of the pair distribution function with increasing of pressure [81]. For this reason, there is aggregation of tips even for $\epsilon = 0 k_B T$ and the aggregation becomes much more prominent in the smectic and crystalline phases, and their anti-ferroelectric versions on account of the strongly increased pressures. Note the abrupt increase in size in going from the the isotropic or nematic to the smectic A_2 phase for stronger attractions and from smectic A or smectic A_2 to smectic B_2 for weaker attractions in Figure 4.4 (a). This in all likelihood is connected with the transition appearing strongly first order.

Figure 4.5 corresponds to another version of the inset of Figure 4.4(a). In this figure, we present the average aggregation number divided by the pressure P in the isotropic and nematic phases for the attraction strengths between 0 and $2 k_B T$, presented as a function of the volume fraction ϕ . The overlapping of the curves for the attraction strengths between 0 and $1 k_B T$ indicates that, at this

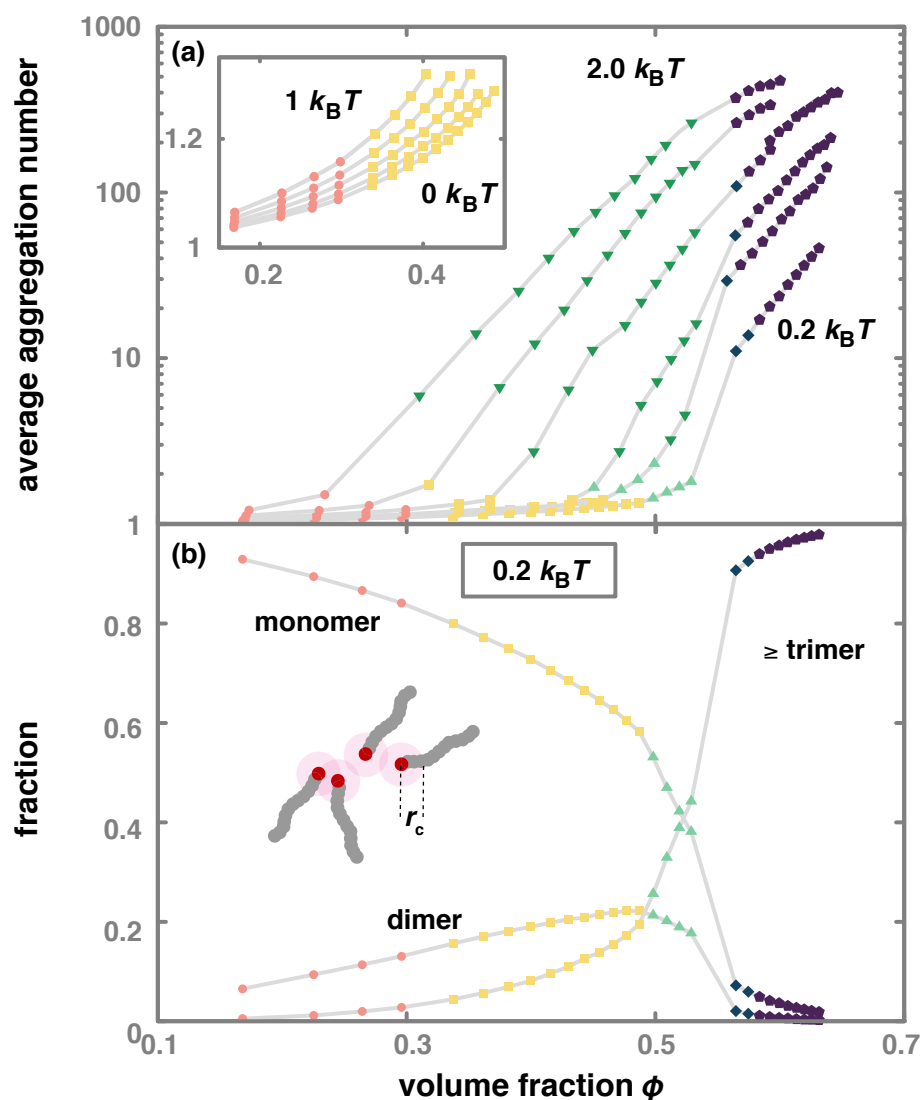


Figure 4.4: (a) Average aggregate size for various attraction strengths between the end groups as a function of the volume fraction of particles. Attraction strengths 0.2, 0.6, 0.8, 1.2, 1.6, and 2.0 $k_B T$ from right to left. The inset is an enlarged view of the graph for lower volume fractions for attractive strength equally spaced between 0 and 1 $k_B T$. (b) Fraction of monomers, dimers, trimers or larger aggregates, which are connected via the attractive ends for attraction strength 0.2 $k_B T$. The particles have aspect ratio $L_0/D = 10.77$ and a flexibility of $L_0/L_P = 0.3$. The following phases are identified: isotropic (orange circle), nematic (yellow square), smectic A (green triangle up), smectic A₂ (dark green triangle down), smectic B₂ (dark blue diamond), and crystalline₂ (dark purple pentagon). In the illustration, r_c represents the distance criterion that determines if beads are directly connected.

interval of attraction energies, the aggregation of the attractive tips is mainly due to the mass action [81].

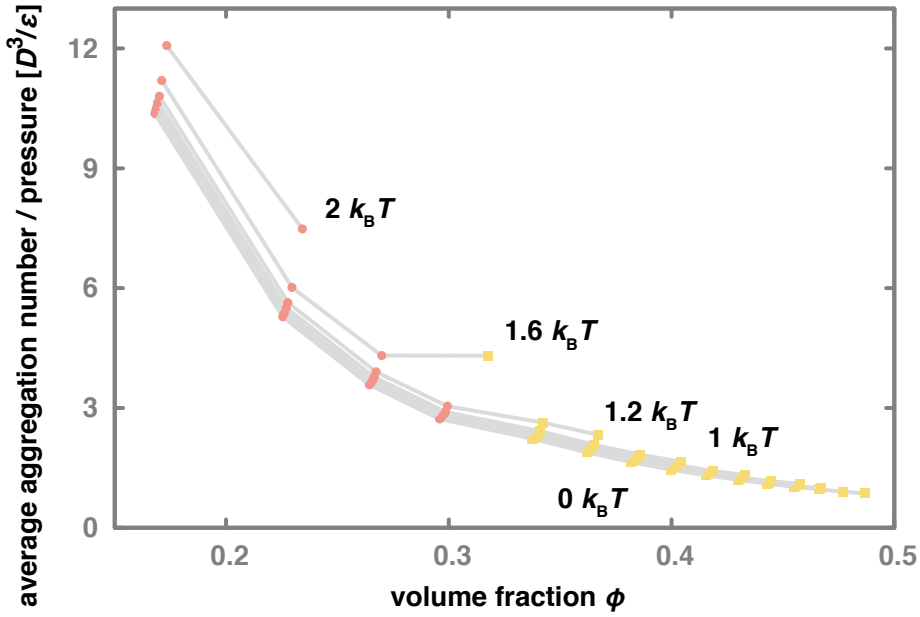


Figure 4.5: Average aggregation number for the attraction strengths between 0 and $2 k_B T$ divided by pressure and presented as a function of the volume fraction ϕ in the isotropic (orange circle), and nematic (yellow square) phases. The particles have a base aspect ratio $L_0/D = 10.77$ and flexibility of $L/L_p = 0.3$.

Interlayer distance - The interlayer distance λ corresponds to the average distance between the centre of masses of consecutive layers. This quantity comprises the average layer size added to the average interlayer gap, as represented in the inset of Figure 4.6, and depends on the characteristics and interactions of the particles. As described in the methods section, we apply two different analysis procedures to our data in order to investigate the interlayer distance. We refer to the results relative to the standard procedure as the *averaged* interlayer distance and to the results relative to the second procedure as the *differentiated* interlayer distance. The main difference is that in the second procedure we differentiate between odd and even layer numbers. In Figure 4.6, we present the averaged interlayer distance λ relative to the average particle length $L + D$, as a function of the volume fraction ϕ for attraction strengths between the end groups ranging in strength from 0 to $2 k_B T$. In Figure 4.7, we present the values of the differentiated interlayer distance for even λ_{even} and odd λ_{odd} over the particle length $L + D$ as a function of the volume fraction ϕ for attraction strengths 0.2, 0.6, and $1.0 k_B T$. Note that the length L is not the bare length but the actual, measured value, somewhat compressed by the ambient pressure.

In Figure 4.6, we find that the scaled interlayer distance $\lambda/(L + D)$ exhibits

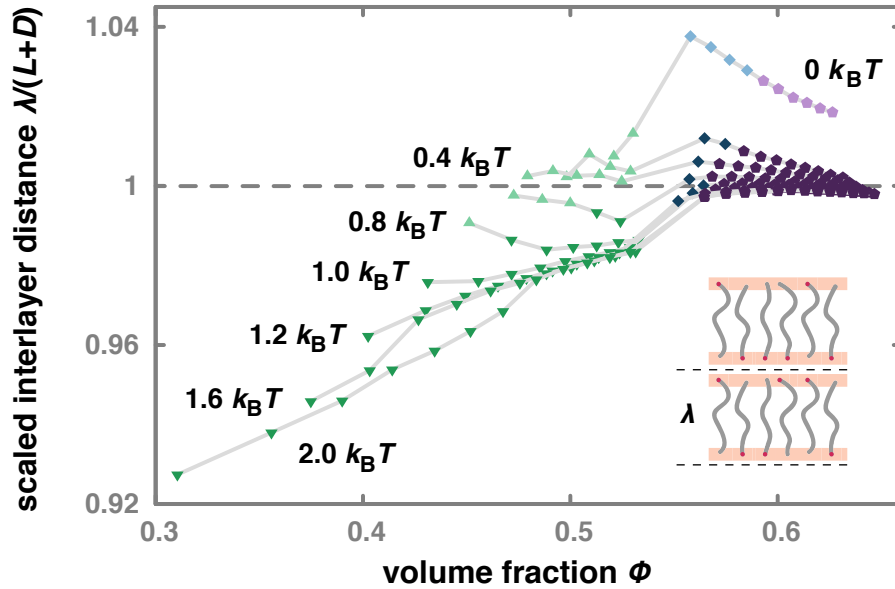


Figure 4.6: Scaled interlayer distance $\lambda/(L + D)$ of repulsive, rod-like particles with a single attractive tip as a function of the volume fraction ϕ for attraction strengths between the end groups ranging from 0 to $2 k_B T$ from top to bottom in the smectic A (green triangle up), smectic A_2 (dark green triangle down), smectic B (blue diamond), smectic B_2 (dark blue diamond), crystalline (purple pentagon) and crystalline₂ (dark purple pentagon) phases. Particles have aspect ratio $L_0/D = 10.77$ and a flexibility of $L_0/L_P = 0.3$. The inset is an illustration representing the interlayer distance λ .

a rich behaviour depending on the attraction strength between the tips and on the state of aggregation. In the smectic A phase and at attraction strengths larger than or equal to $1 k_B T$, the scaled interlayer distance increases with the volume fraction. Note that these values are smaller than unity, which means that the layers slightly interdigitate. This interpenetration lowers the interaction energy because it allows for a larger surface contact between the tips, which consist of an exposed attractive hemispherical cap. Between 0.8 and $0.6 k_B T$, the interlayer distance seems to decrease with increasing volume fraction. Interestingly, it is for these strengths that we identify both the smectic A and the smectic A_2 phase. For lower attraction strengths, the scaled interlayer distance is slightly larger than unity, indicating that, in this case, layers are nearly touching each other. Nevertheless, the dependence on the volume fraction is not obvious. Overall, the scaled interlayer distance seems to decrease with increasing attraction strength between tips. This effect is unambiguous if we consider volume fractions lower than 0.45 . In other words, at a fixed volume fraction, layers interpenetrate more as the attraction strength between tips increases. As a result, the inlayer density is expected to be smaller. In fact, in a previous paper, where we investigate the

semi-flexible repulsive rods, we find similar behaviour [52]. In the smectic B and the crystalline phases or the smectic B₂ and the crystalline₂ phases, we note that the scaled interlayer distance decreases with volume fraction and that the value converges to unity with increasing volume fraction for all attraction strengths.

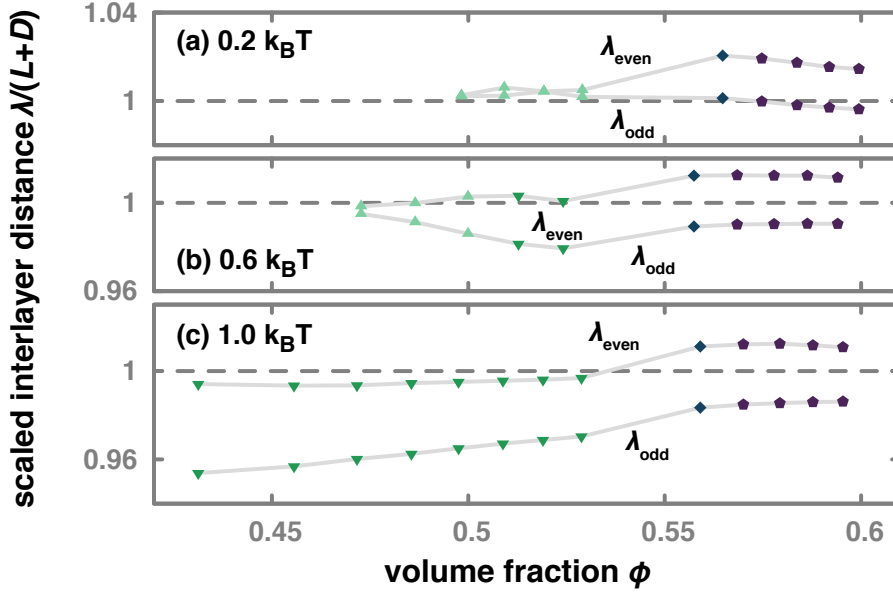


Figure 4.7: Average interlayer distance relative to the average rod length $\lambda_{\text{odd}}/(L + D)$ for odd and $\lambda_{\text{even}}/(L + D)$ for even interlayer distances of repulsive, rod-like particles that have an attractive tip in the smectic A (green triangle up), smectic A₂ (dark green triangle down), smectic B₂ (dark blue diamond), and crystalline₂ (dark purple pentagon) phases for attraction strengths of (a) $0.2 k_B T$, (b) $0.6 k_B T$, and (c) $1.0 k_B T$. Particles have aspect ratio $L_0/D = 10.77$ and flexibility of $L/L_P = 0.3$.

Figure 4.6 clarifies several features of our system but hides the distinction between layers present in the anti-ferroelectric phases. In Figure 4.7, which presents results from the differentiated analysis, there is the distinction between odd and even interlayers at three values of the attraction strength. At the first value of $0.2 k_B T$, represented in (a), we find that the interlayer distance is approximately the same for even and odd interlayers in the smectic A phase. As expected, their values are also approximately equivalent to the averaged layer thickness, once the layers are nearly indistinct in this phase. Nevertheless, in the smectic B₂ and crystalline₂ phases, the values for the even and odd interlayer distance, which respectively contain the smaller and larger fraction of attractive tips, are distinct. The former is larger than unity and the latter is approximately unity. These values slightly decrease with the volume fraction. In Figure 4.7 (b), the results are for the attraction strength of $0.6 k_B T$. In the smectic A phase, we find that for that case the values of the odd and even interlayer distances are approximately

equal only at the lowest volume fraction, and that they become distinct as the volume fraction increases. Notice that the even interlayer distances are larger than the odd ones, because even though the anti-ferroelectric order parameter δ is different from zero, it is smaller than $1/2$ and hence the phase is not classified as smectic A_2 . The even interlayer distance is approximately constant and equal to unity, while the odd interlayer distance becomes smaller, meaning that the layers in these interfaces are also interpenetrating. In the smectic A_2 phase, the even interlayer distance follows the same trend as in the smectic A phase, while the odd interlayer is slight smaller but the dependence on volume fraction is not clear due to the lack of data points available in this phase. In the smectic B_2 and crystalline₂ phases, it seems that even and odd interlayer distances do not depend on the concentration. Their values are slightly above and below unity, respectively. We find the same for an attraction strength of $1.6 k_B T$, as we see in Figure 4.7 (c). For the smectic A_2 phase, we find that the values are rather different and that, while the trend for even interlayer distance remains as described before, the odd interlayer distance, which is smaller than unity, tends to slightly increase with increasing volume fraction. This effect is probably due to the lower in-layer density of particles at lower volume fractions, which offers more space for the particles to interpenetrate.

Anti-ferroelectric phase transition - The anti-ferroelectric phase transition in the phase diagram is linked with the polarity of our single-ended attractive elongated particles. We identify this phase transition using the anti-ferroelectric order parameter δ , defined in Section 4.2, and presented in Figure 4.8 as a function of the volume fraction ϕ for various values of the attraction strength. Its value continuously increases with increasing volume fraction, which indicates a second order phase transition. As previously mentioned, we are not able to pinpoint the anti-ferroelectric phase transition in the smectic B and crystalline phases: we find the smectic B_2 and crystalline₂ even at the lowest attraction strength investigated ($0.2 k_B T$). In the inset, the anti-ferroelectric order parameter δ is represented together with the smectic σ order parameter as a function of concentration for attraction strength $0.7 k_B T$. The smectic order parameter itself does not provide a clear indication of the presence of a anti-ferroelectric transition although that it could be masked by our limited resolution in the volume fraction ϕ . For a comparison with our simple Maier-Saupe-McMillan model, where we do see much more enhanced smectic ordering beyond the transition in Figure 4.15 (a), we refer to the Appendix 4.6 and to Figure 4.9, which is another version of the inset of Figure 4.8. In the figure, we compare the smectic order parameter σ as a function of $\Delta\phi/\phi_{N-Sm}$, where $\Delta\phi$ is the difference between the volume fraction and the volume fraction at the Nematic-to-Smectic A (for $\epsilon = 0 k_B T$) or Smectic A_2 phase (for $\epsilon = 0.7 k_B T$) transition, $\Delta\phi = \phi - \phi_{N-Sm}$. The volume fraction ϕ_{N-Sm} at the

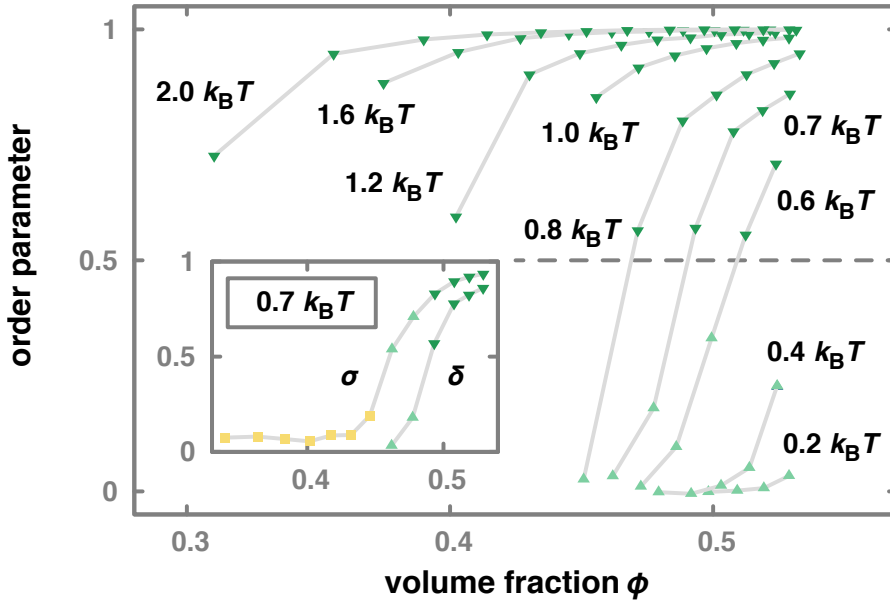


Figure 4.8: Anti-ferroelectric order parameter δ of repulsive, rod-like particles that have a single attractive tip as a function of volume fraction ϕ for various values of the attraction strength between the attractive tips. In the inset we compare the anti-ferroelectric δ and smectic σ order parameters for the attraction strength of $0.7 k_B T$. Particles have aspect ratio $L_0/D = 10.77$ and flexibility of $L_0/L_p = 0.3$. The following phases are identified: nematic (yellow square), smectic A (green triangle up), and smectic A_2 (dark green triangle down) phases.

transition is estimated by the average between the highest and lowest values of the volume fraction at which, respectively, the nematic and smectic A or smectic A_2 phases are stable. We find that the smectic order parameter σ is smaller at smaller attraction strength from the comparison of the values of ϵ between 0 and $0.7 k_B T$. Therefore, this result shows that the degree of order increases due to the attraction between single tips in the layered phases.

Smectic ordering potential - The smectic ordering potential $\Delta U(z)$ represents the molecular field that a particle experiences from the other particles within a smectic layer. We calculate it for our simulations in the smectic A phase around the anti-ferroelectric phase transition, as represented in the top inset of Figure 4.10. From the inset, we find that both the height and the width changes as we increase the attraction strength at a constant volume fraction of $\phi = 0.52$: the potential barrier increases and becomes narrower around the centre of the layer $z/L = 0.5$. In other words, the smectic layers become increasingly ordered, as we also see from the snapshots in Figure 4.3 (c). The smectic ordering potential seems to show more noise at higher attraction strengths, in particular in between the layers. This, in all likelihood, is due to the poor statistics: once the particle centres of masses are concentrated around the centre of the layer fewer parti-

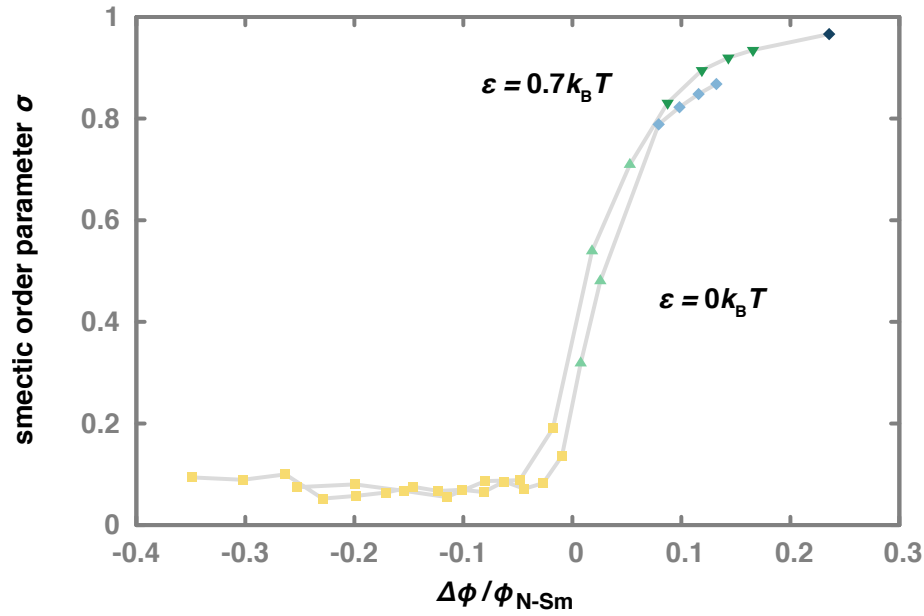


Figure 4.9: Smectic order parameter σ of repulsive, rod-like particles that have a single attractive tip as a function of $\Delta\phi/\phi_{N-Sm}$, where $\Delta\phi$ is the difference between the volume fraction and the volume fraction at the Nematic-to-Smectic A (for $\epsilon = 0$) or Smectic A₂ phase (for $\epsilon = 0.7 k_B T$) transition, $\Delta\phi = \phi - \phi_{N-Sm}$, for attraction strengths of 0 and $0.7 k_B T$. Particles have aspect ratio $L_0/D = 10.77$ and flexibility of $L_0/L_P = 0.3$. The following phases are identified: nematic (yellow square), smectic A (green triangle up), smectic A₂ (dark green triangle down), smectic B (blue diamond), and smectic B₂ (dark blue diamond) phases.

cles venture out in between the layers. From Figure 4.10, we find that the height of the smectic ordering potential linearly increases with the attraction strength at the volume fraction of $\phi = 0.52$, and the trend does not seem to be changed crossing the anti-ferroelectric phase transition. The same is true if the volume fraction is increased at constant attraction strength, as it is shown in the top inset of Figure 4.10. Therefore, our particles are more strongly attached to a layered structure and, on top of that, the layer itself is more strongly confined due to the small amplitude in the fluctuations of the particle positions around the average. This molecular field of particles in the smectic phase as well as the smectic and anti-ferroelectric order parameters, presented in the previous paragraph, are also reasonably well-described by our simple Maier-Saupe-McMillan model (see Figures 4.17 and 4.18 in the Appendix).

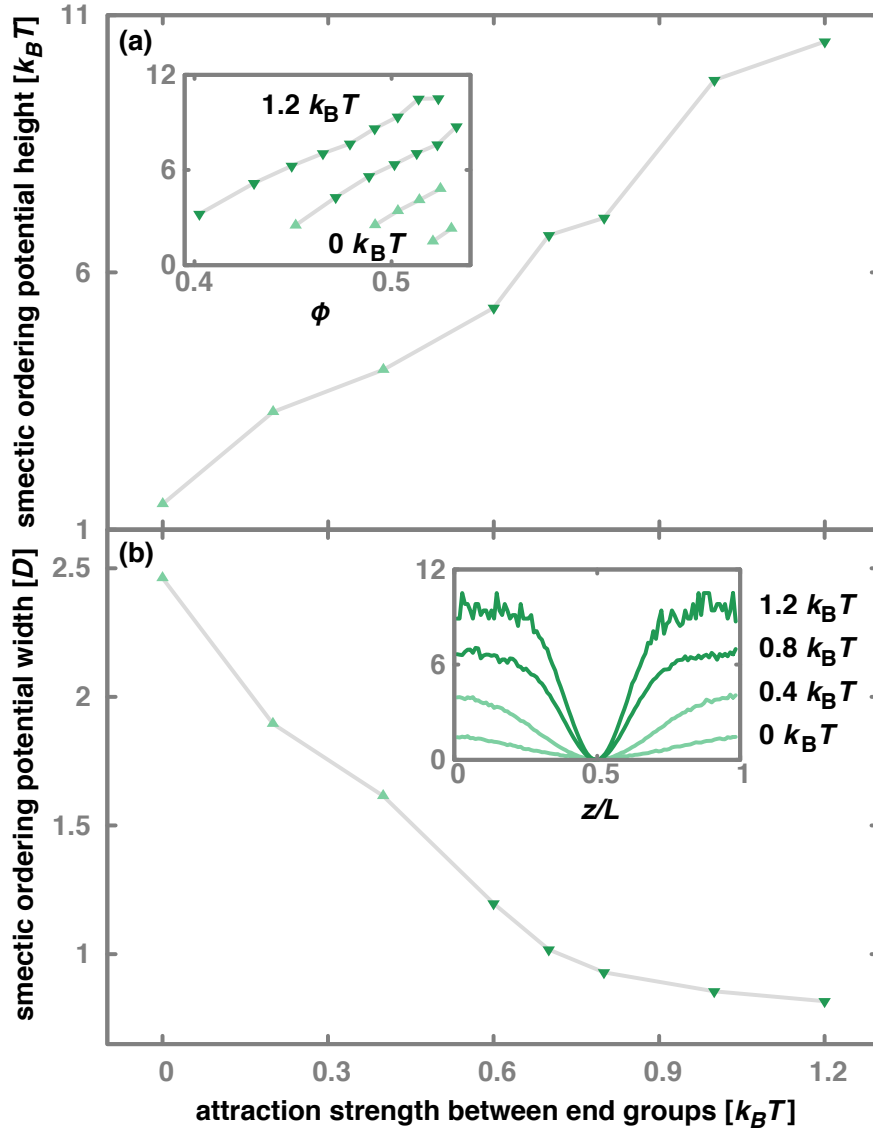


Figure 4.10: Smectic ordering potential of repulsive, rod-like particles with a single attractive tip. Particles have an aspect ratio of $L_0/D = 10.77$ and a flexibility of $L_0/L_P = 0.3$. (a) Height of the smectic ordering potential of repulsive as a function of the attraction strength between tips in the smectic A (green triangle up) or smectic A_2 (dark green triangle down) phases at a volume fraction of $\phi \cong 0.52$. In the inset, there is the same height of the smectic ordering potential of repulsive as a function of the volume fraction for attraction strengths 0, 0.4, 0.8 and 1.2 $k_B T$. (b) Width of the smectic ordering potential of repulsive as a function of the attraction strength between tips in units of $k_B T$. In the inset, the smectic ordering potential $\Delta U(z)$ is presented as a function of the position along the director, normalised by the particle length z/L . The increase of the attraction strength drives the stabilisation of the smectic A and smectic A_2 phases.

4.5 Comparison with experiments

Here, we compare our simulations with experiments on the M13 virus performed by our collaborators from the *Centre de Recherche Paul Pascal* (CRPP) in Bordeaux, France [42]. (See Chapter 2 for its dimensions and persistence length.) In Figure 4.11, we show a schematic of the structure of this chiral virus, which has different ends and hence is chemically asymmetric. Because of this, it is possible to selectively graft fluorescent dye molecules of the DyLight Fluor family onto the end exposing the P3 protein [12]. These dye molecules are hydrophobic, implying that the number of grafted dye molecules dictates the size of the hydrophobic patch on the surface of an overall hydrophilic surface of the virus. We assume here that the strength of the attraction between the patches is proportional to this area. Whether there is a linear relationship between the number of dyes and the strength of the attraction is contentious, because grafting the dyes into the proteins could potentially unfold P3 protein and expose hydrophobic moieties.

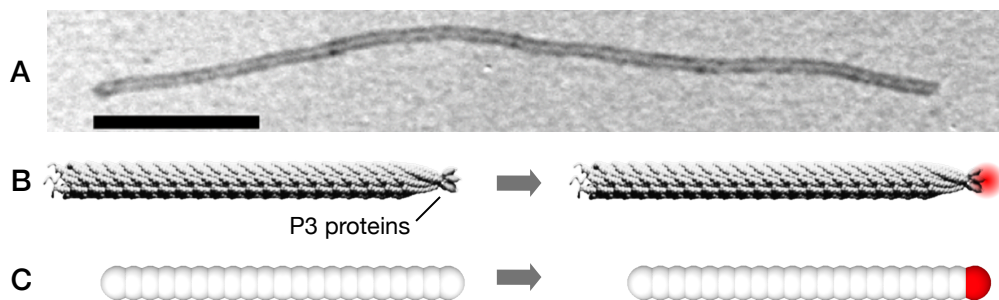


Figure 4.11: (A) Transmission electron microscopy (TEM) of the M13 virus. (B) Schematic representation of untreated (left) and functionalised (right) virus exhibiting attractive patch at its single tip. (C) Schematic representation of semi-flexible rod-like particle, modelled as a bead-spring chain. Purely repulsive particle (left) and particle with one attractive bead at a single end (right). Figure reproduced from Reference [42].

Figure 4.12 presents the phase diagrams from experiments and simulations in vertical side-by-side view and same colour code for easier comparison. For the experimental phase diagram that is shown in Figure 4.12 A, 0, 1, 3, and 10 dyes are attached to virus end for the preparation of samples with various concentrations up to around 180 mg/mL. Indicated in the phase diagram are, as a function of concentration of particles and the number of grafted dyes, the various phases that include isotropic, (chiral) nematic, smectic A and B, and columnar phases. The smectic phases are identified using differential interference contrast (DIC) and fluorescence optical microscopy. The smectic A and B phases and columnar phase are distinguished by small angle X-ray scattering (SAXS) and optical (DIC

and fluorescence) microscopy. Finally, the isotropic and (chiral) nematic phases are identified by employing polarising optical microscopy. Details of the procedure to identify the various phases can be found in references [27, 41]. The stability ranges of the isotropic phase (green area), the nematic (red), the smectic phases (blue), and columnar phase (yellow) are also indicated in Figure 4.12 A. In the nematic domain, the usual nematic and the chiral nematic are represented by the red and pink symbols. In the smectic domain we distinguish between single and coexisting phases using open and solid symbols. Insets give the nematic (a) and chiral nematic (b) textures as observed in polarisation microscopy. The lamellar texture of the smectic phases is clearly visible in a DIC image (c), but is lacking in the columnar phase (d). In Figure 4.12 B, we present the phase diagram from simulations that we explain in detail in Section 4.3. In this version of the phase diagram, we do not differentiate between the smectic A and smectic A_2 , as the experimental techniques employed do not allow to distinguish them, also for easier comparison.

From the experimental phase diagram, we find that an increasing the number of dye molecules at the tips of the virus particles strongly affects the nematic-smectic transition yet has virtually no effect on the other transitions. We clearly see that the smectic phase is stabilised at the expense of the nematic phase with increasing strength of the attraction between the tips of the particles. The phase gap between the two phases also increases with increasing strength of the attraction. Another striking feature of the phase diagram is the disappearing of the chiral nematic (cholesteric) phase in favour of the uniaxial nematic phase upon grafting even a single dye molecule to the tip of the particles. We put forward that an explanation for our observations must lie in the fact that the end functionalised rods turn out to form planar aggregates. Our simulations show qualitative agreement with the experimental data: increasing the stickiness of the tips affects only the nematic-smectic phase transition. We find that the stability of the smectic phase increases at the cost of the nematic phase with increasing the tip stickiness, as does the phase gap. There are some discrepancies too, in particular the absence of the columnar phase that is replaced by a crystalline phase, as already discussed in Section 4.3. Another discrepancy is the large phase gap between the smectic A and smectic B phases that is not seen experimentally. It is not clear if this is due to a different ways of classifying the smectic B phase, which is not trivial. Finally, Figures 4.12A and B show that there is not an one-to-one correspondence between mass concentration in the experiments and the volume fraction in the simulations.

As in the experiments, we find planar aggregates to form in the simulations. This is supported by the representative images of Figure 4.13, where we compare typical textures obtained by means of fluorescence optical microscopy and our

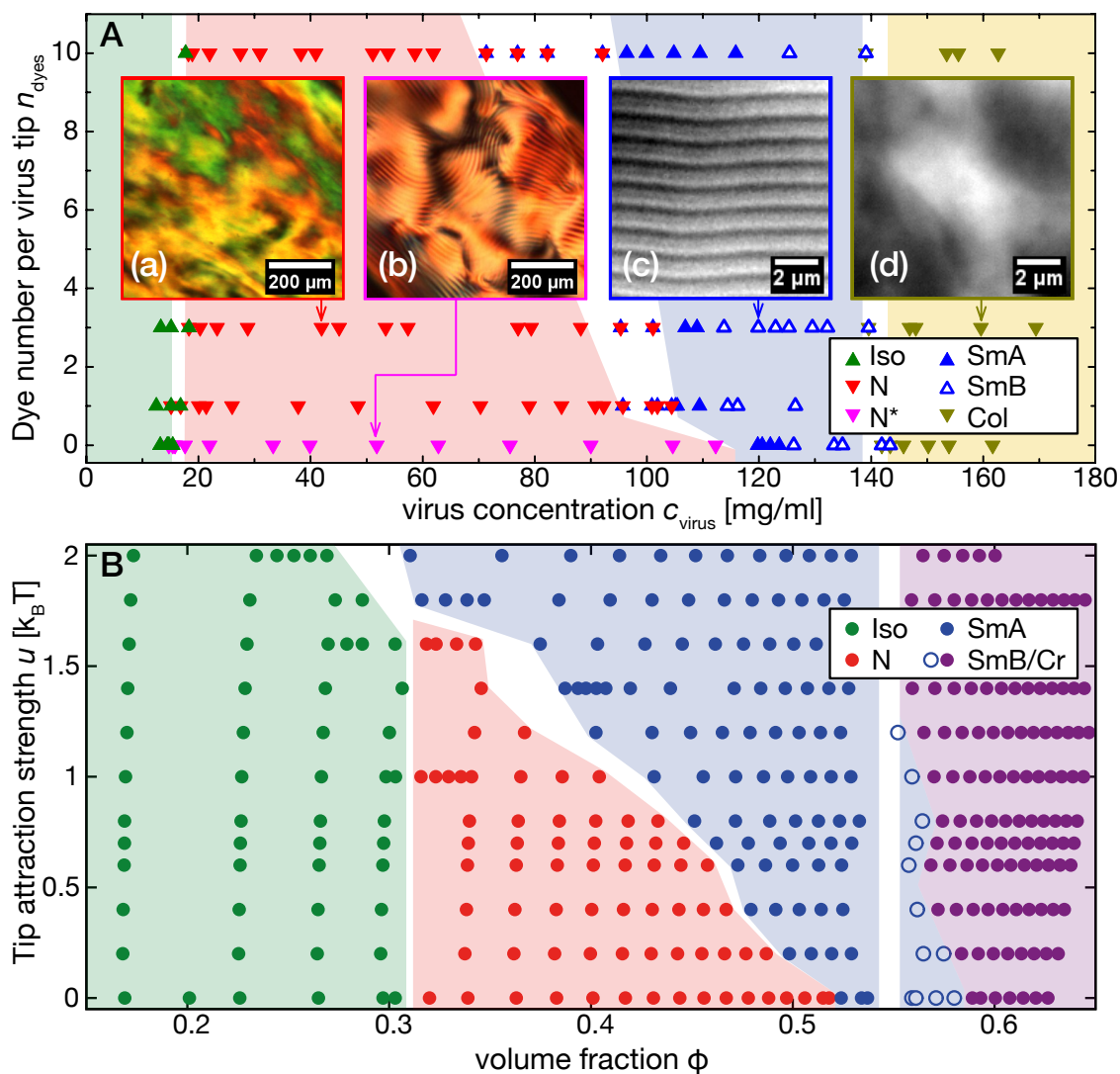


Figure 4.12: (A) Phase diagram of filamentous viruses in terms of number of grafted dyes as a function of concentration c_{virus} . System with 0 dyes represents “raw” viruses and systems with 1, 3, and 10 dyes represent the patchy viruses. The colour code for the different phases is given in the insert. We use DIC and fluorescence optical microscopy to identify the smectic phases. To distinguish between the smectic A and B phases and columnar phase we make use of SAXS and optical (DIC and fluorescence) microscopy. Polarising optical microscopy we use to identify the isotropic and (chiral) nematic phases. Insets give the nematic (a) and chiral nematic (b) textures as observed in polarisation microscopy. The lamellar texture of the smectic phases is clearly visible in a DIC image (c), which lacks in the columnar phase (d). (B) Calculated phase diagram in terms of the attraction strength u between the end groups as a function of the volume fraction ϕ of the semi-flexible particles. Aspect ratio $L_0/D = 10.77$ and length over persistence length of $L_0/L_P = 0.3$. Non-sticky end group beads interact via a repulsive soft-core potential. The phases are identified using global order parameters. Figure reproduced from Reference [42].

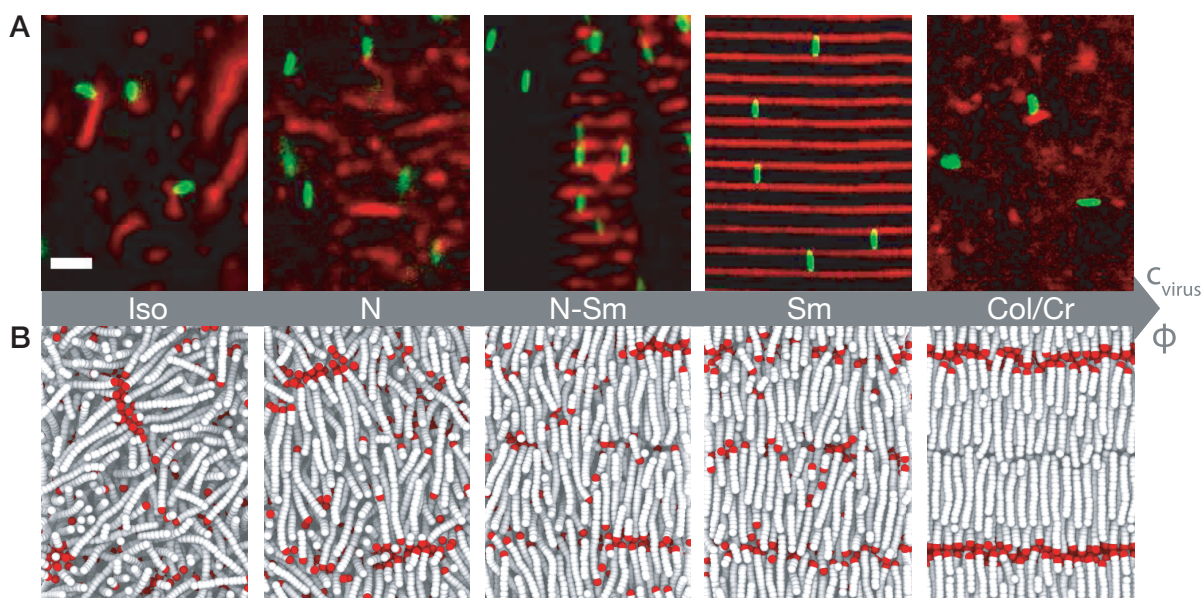


Figure 4.13: (A) Typical textures of patchy virus suspension in various liquid-crystalline phases taken with fluorescent optical microscopy. A red signal corresponds to the position of the patch. A green signal corresponds to body-functionalised viruses which are added in tracer amount to the suspension. (B) Corresponding simulation snapshots. White beads are purely repulsive and red bead are attractive. In the isotropic phase (Iso), the viruses have random orientations. In the nematic phase (N), viruses are aligned along the director but lack positional order. There are some aggregates in both phases, which are precursors of smectic layers. The first order Nematic-Smectic phase transition (N-Sm) is confirmed by the presence of sharp boundary between the phases. In the smectic phase (Sm), all patches are well localised in the interlayer space. In the columnar phase (Col), patches are uniformly distributed. Body-functionalised viruses are not aligned due to small domains size. Scale bar: $2\mu\text{m}$. Figure reproduced from Reference [42].

computer simulations. Focusing on the isotropic phase first, we find experimentally randomly oriented "lamellae": in the left most microscopic image of Figure 4.13 an elongated red objects representing the clustered tips. Also visible are the green lines which are viruses body-labeled with a different fluorescent dye. ($1:10^5$ of the virus particles are body-labeled.) In the microscopic image, these are attached to the red tip regions and nearly perpendicular to them. This shows that the aggregates are indeed planar. The planar structure is consistent with the snapshot of our computer simulations shown below it. The snapshot provides detailed information about the structure of the lamellae in which the tips form 2 dimensional structure attached to which are attached the body of the particles in both sides. They superficially resemble disk-like inverted micelles, as we discuss

in Section 4.4.

Similar lamellae can be observed in the nematic phase except that in this phase they are oriented perpendicular to the director, whereas in the isotropic phase they are randomly oriented both in the experiments and simulations (see Figure 4.13 b). Figure 4.13c shows that lamellar aggregates condensed in smectic domains in the nematic background. The particles are aligned along the director in both phases, as to be expected. In Figure 4.13 d we have the single phase smectic. The alignment of the particles is perpendicular to the layer allowing us to rule out smectic C or other types of tilted smectic. In the simulations we are able to distinguish between two types of smectic A phase, as shown in the bottom part of Figure 4.13 d. For small values of ϵ , the red tip beads occupy every interlayer spacing and for large enough values only every other interlayer spacing creating a bilayer-like structure. We speculate that because the optical images are the result of signal integration through the sample thickness, shifted bilayer domains project pattern with 1 particle length periodicity not allowing them to be experimentally discriminated.

In contrast to the smectic phases, which do exhibit an almost defect free structure, the columnar phase is characterised by finite domain sizes as a comparison between Figures 4.13 d (top images). Figure 4.13 e represents the columnar phase because lamellar structures are not observed in DIC images and, perhaps more convincingly, the SAXS profile reveals positional order consistent with hexagonal/hexatic ordering [26]. The fact that the three signals of body-labeled viruses are not parallel confirms the absence of a single domain. The absence of bright red localised signals support the absence of layering. The diffuse signals arguably do not reflect actual clustering but are a result of the integration of signal through the bulk of the sample.

We also compare the smectic ordering potential from experiments and simulations in Figure 4.14, as the main effect of the attractive tip is to widen the smectic stability range. We find that the results show the same trends: (i) the magnitude of the ordering potential increases with an increasing tip patchiness for a given particle packing fraction as shown in (a) and (b), and (ii) the potential height increases with the particle concentration, for both repulsive and attractive tips as can be observed from (c) and (d). Additionally, from Figure 4.14 (a) and (b), we find that the smectic potential also becomes narrower with an increasing concentration and the attraction between (or the number of dyes in) the tips of the viruses. This implies that the amplitude of the fluctuations of the particles around their equilibrium positions in the layers becomes weaker and, hence, that the particle positions become more localised. As the aspect ratio of the particles is smaller in our numerical simulations, we expect lower smectic potentials compared to the experimental ones, as shown in Figure 4.14. The reason is that the stability of the

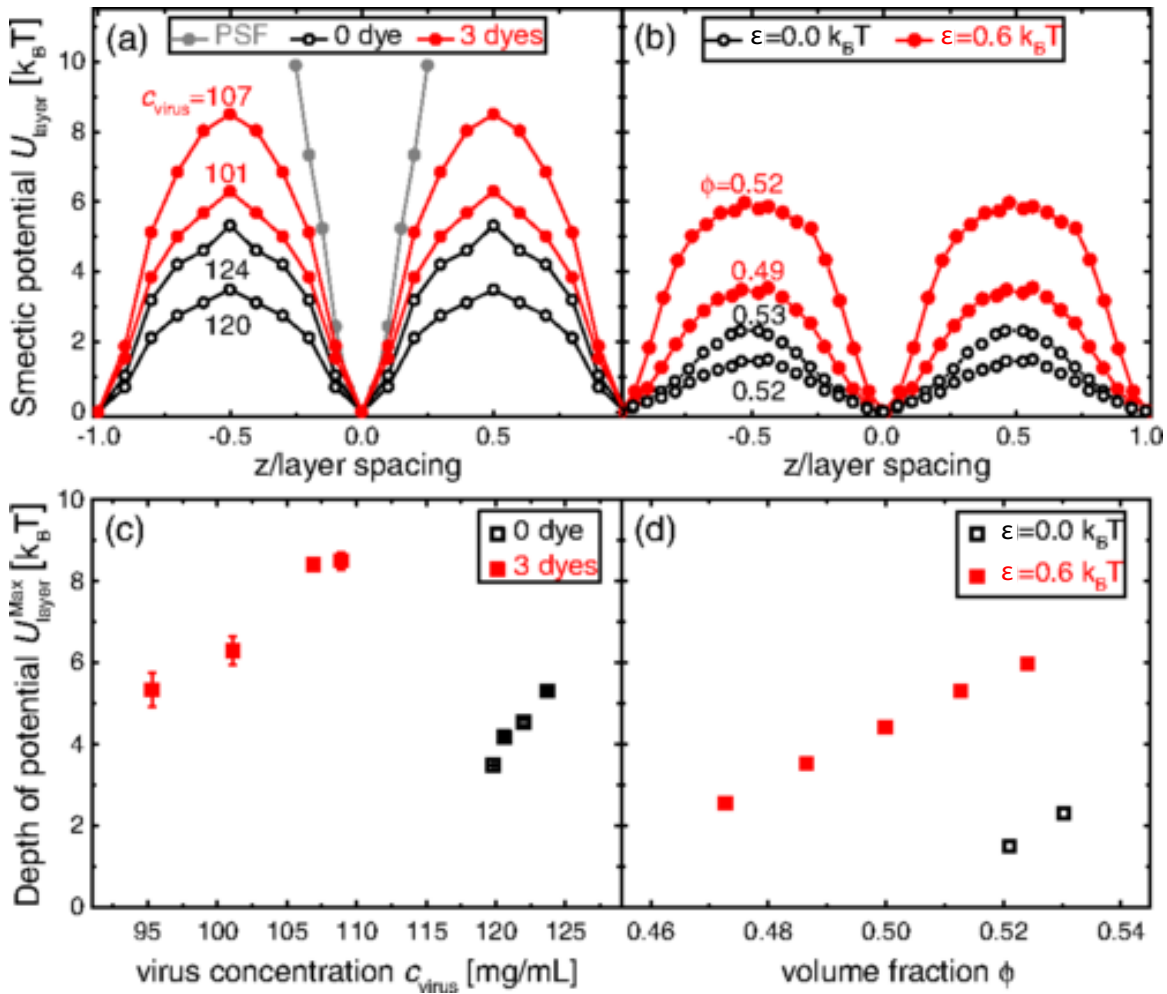


Figure 4.14: Smectic ordering potentials calculated from experimental (a) and simulated (b) distribution of particles, as a function of the particle position, normalised by the smectic layer spacing, for different particle concentrations and volume fractions. In grey, we indicate the experimentally measured potential of immobile particles, which is the equivalent for potentials of the point spread function (PSF) of the optical setup. Smectic potential barriers as a function of the virus concentration for experiments (c) and as a function of the volume fraction for simulations (d). In all graphs, open black and full red symbols correspond to “raw” repulsive and tip-functionalised rod-like particles, respectively. Figure reproduced from Reference [42].

smectic A phase of repulsive rod-like particles reduces with decreasing length [25]. Notice from Figure 4.14 (c) and (d) that, irrespective of the strength of tip attraction, we find the same slope of the ordering potential as a function of the particle concentration in both the experiments and the simulations. This is to be expected, because the molecular field a test particle experiences in a lyotropic smectic must be proportional to the average density [31]. Even though we have not been able to find a sensible mapping between our experimental and simulation results because of the large disparity between the respective aspect ratios of the particles, our simulations do account for most of the features we observe in our experimental system. This is true for both the phase behaviour and ordering potentials, suggesting that our prediction that a tip attraction strength as small as $\epsilon \sim 1 k_B T$ is sufficient to fully suppress the nematic phase and promote the smectic organisation in dispersions of otherwise mutually repelling rod-like particles is plausible. This small value is actually not surprising, considering that free energy differences between particles in coexisting liquid crystalline phases of rod-like particles are typically of the order of the thermal energy and often much smaller than that [67].

4.6 Discussion and conclusions

The aim of the present work is to study by means of molecular dynamics simulations the influence that attractive interaction between one of the two ends of a collection of otherwise mutually repulsive, elongated particles have on their phase behaviour, using computer simulations. Our work shows that their phase behaviour, and the structure of the various liquid-crystalline phases, are strongly affected even by relatively weak interaction strengths on the order of the thermal energy. The phase behaviour has two striking features: (1) the formation of bi-layered anti-ferroelectric phases and (2) the large increase of stability of smectic A at the expense of the nematic phase, and even at the expense of the isotropic phase as we increase the attraction strength between the tips beyond about $1.6 k_B T$. The key factor is the interplay between the interaction energy, polarity of the particles, and the phase microstructure. The analysis of the microstructure reveals that the stability of the isotropic and nematic phases is affected by the aggregation of the tips, only if the particles align in response to the local increase in concentration. In the layered phases, the organisation of the particles with the attractive tips results in more strongly ordered microstructures even at very weak attraction energies.

Our results concerning the shift of the nematic-to-smectic A phase transition to lower volume fractions, which also seems to become more strongly first or-

der with an increase of the attraction strength, are supported by experimental evidence. Despite the fact that the difference in the aspect ratio between simulated and experimental particles prevents us to make a quantitative comparison, we are able to qualitatively compare the smectic ordering potential of the experimental and computational model particles. We find for both of them larger values of the height and smaller values of the width as the attraction strength between tips increases. As expected, because the experimental model particles are larger in aspect ratio, their smectic potential height is also larger, due to the increase of stability of the smectic A phase with increasing aspect ratio [82]. In our theory (Appendix 4.6), the shift of the nematic-to-smectic A phase transition is independent of the volume fraction. Nevertheless, the shift to lower volume fractions is captured if the nematic-to-smectic A_2 phase transition is considered. The height and width of the effective smectic ordering potential from our Maier-Saupe-McMillan theory does not emulate the smectic ordering potential from our simulations. This might be due to our choice of representing it as a cosine function instead of a Gaussian function.

In spite of the obvious limitations, our study does contribute to the understanding of how selective surface functionalisation of colloidal liquid crystals affects their self-organisation, by providing a systematic study of the stability and structure of these phases for a wide range of both volume fractions and attraction strengths. We show that incorporating a single (enthalpic) functionalised end in elongated colloidal particles gives rise to an even more complex and rich phase behaviour than for the purely repulsive ones. In the light of this, we suggest that agreement between purely repulsive models and experiment cannot be expected because residual attractive interactions, local or global, strongly influence the phase behaviour.

4.A The anti-ferroelectric phase transition within a Maier-Saupe-McMillan type theory

Here, we describe a simplified model for the anti-ferroelectric phase transition for N perfectly parallel, rod-like particles, equipped with a single tip attractive interaction. These particles are aligned along the z -axis, forming the nematic phase if they are uniformly distributed, or smectic phases if their positions are periodically distributed along the z -axis. The periodicity in the smectic phases is d , corresponding to the spacing between the layers. The single tip attraction is the key element for the existence of the smectic A_2 phase. In this bilayered phase, the distribution of the attractive tip has the periodicity $2d$.

Our description is inspired by Maier-Saupe-McMillan theory [83, 84]. We write

the Helmholtz free energy F in one layer as the sum of the Gibbs entropy, proportional to the position density distribution along the director of both the elongated particles $\rho(z)$ and the attractive tips $f(z)$, and energy terms proportional to the molecular field or smectic ordering potential, $\Delta U_{\text{SmA}}(z)$, and the interaction energy between attractive tips, $\Delta U_{\text{SmA}_2}(z)$,

$$\frac{\beta F}{N} = \int_{-\frac{d}{2}}^{+\frac{d}{2}} dz \left[\rho(z) \ln \rho(z) + \frac{1}{2} \rho(z) \beta \Delta U_{\text{SmA}}(z) \right] + \int_{-\frac{d}{2}}^{+\frac{d}{2}} dz \left[f(z) \ln f(z) + \frac{1}{2} f(z) \beta \Delta U_{\text{SmA}_2}(z) \right].$$

The factor 1/2 in the energy terms corrects for double counting; the distribution functions $f(z)$ and $\rho(z)$ are properly normalised.

The energy term $\beta \Delta U_{\text{SmA}}(z)$ drives the nematic-smectic A phase transition and it is expected to be proportional to the volume fraction $\phi \in [0, 1]$ and the smectic ordering parameter σ , so

$$\beta \Delta U_{\text{SmA}}(z) = -\phi \gamma \sigma \cos\left(\frac{2\pi z}{d}\right), \quad (4.1)$$

where γ is an adjustable parameter and the cosine describes the periodic molecular field (of periodicity d). The smectic ordering parameter is given by

$$\sigma = \int_{-\frac{d}{2}}^{+\frac{d}{2}} dz \rho(z) \cos\left(\frac{2\pi z}{d}\right). \quad (4.2)$$

Note that 4.1 is temperature invariant: it represents the hard-core nature of the interactions. The energy term $\beta \Delta U_{\text{SmA}_2}(z)$ drives the anti-ferroelectric transition and it should arguably be also proportional to the volume fraction ϕ and some power of the smectic ordering parameter σ , as well as to the anti-ferroelectric order parameter δ itself. We put forward

$$\beta \Delta U_{\text{SmA}_2}(z) = -\phi \sigma^2 \tilde{\epsilon} \delta \sin\left(\frac{2\pi z}{2d}\right),$$

where $\tilde{\epsilon}$ is a (dimensionless) measure for the strength of the attraction between the tips and the sine function represents the periodicity $2d$ of the anti-ferroelectric state. There is no obvious mapping of the sticking energy of our simulations and that of our model, although we would guess that $\tilde{\epsilon} \propto \epsilon$. The anti-ferroelectric ordering parameter is given by

$$\delta = \int_{-\frac{d}{2}}^{+\frac{d}{2}} dz f(z) \sin\left(\frac{2\pi z}{2d}\right). \quad (4.3)$$

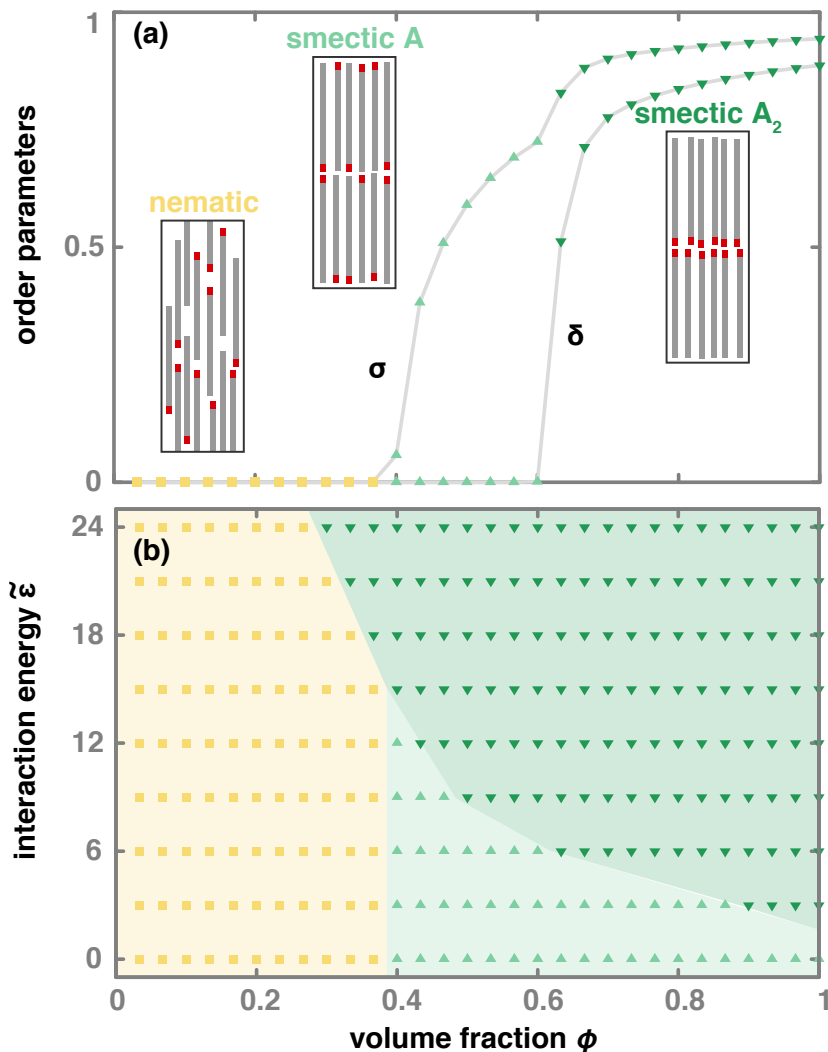


Figure 4.15: Theoretical approach to describe the anti-ferroelectric phase transition for perfectly parallel, hard rods that have a single attractive end. Phases identified are: nematic (yellow square), smectic A (green triangle up), and smectic A₂ (dark green triangle down). (a) Smectic and anti-ferroelectric order parameters numerically calculated for the attraction strength $\tilde{\epsilon} = 6$ and the adjustable parameter $\gamma = 5$, chosen to adjust the volume fraction interval for convenient viewing. (b) Phase diagram obtained from classification based on the order parameters for the same value of the adjustable parameter $\gamma = 5$. We find that the nematic phase is destabilised in favour of the smectic A₂ phase and that the smectic A phase is suppressed at high enough attraction strength $\tilde{\epsilon}$.

In equilibrium, the free energy must be functionally minimised, $\delta(\beta F/N)/\delta p = \lambda$ and $\delta(\beta F/N)/\delta f = \mu$, accounting for the normalisation conditions

$$\int_{-\frac{d}{2}}^{+\frac{d}{2}} dz \rho(z) = \int_{-\frac{d}{2}}^{+\frac{d}{2}} dz f(z) = 1,$$

which require us to introduce the Lagrange multipliers λ and μ .

Making use of the normalisation of $\rho(z)$, we find that

$$\rho(z) = \frac{\exp\left[\sigma\phi(\gamma + \tilde{\epsilon}\delta^2)\cos\left(\frac{2\pi z}{d}\right)\right]}{\int_{-\frac{d}{2}}^{+\frac{d}{2}} dz \exp\left[\sigma\phi(\gamma + \tilde{\epsilon}\delta^2)\cos\left(\frac{2\pi z}{d}\right)\right]}. \quad (4.4)$$

Note that $\tilde{\epsilon}$ is an energy scaled to the thermal energy and hence temperature dependent. From thermodynamics, we have $\tilde{\epsilon}(T) = \tilde{\epsilon}(T_0) - \tilde{h}(T_0)(T - T_0)/T_0$, with \tilde{h} a dimensionless enthalpy and T_0 a reference temperature. For hydrophobic interactions $\tilde{h} < 0$ implying that the molecular field increases in strength with increasing temperature.

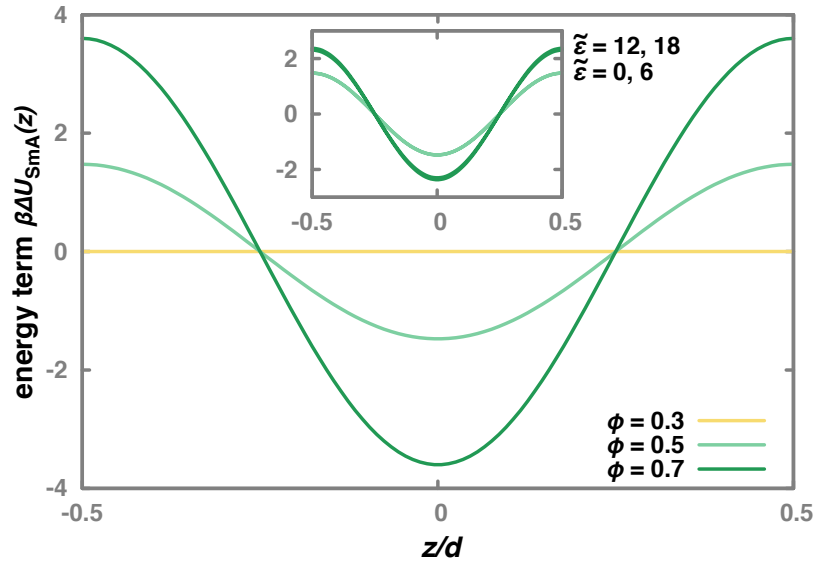


Figure 4.16: Energy term $\beta\Delta U_{\text{SmA}_2}(z)$ or smectic ordering potential as a function of the position normalised by the layer thickness numerically calculated for the attraction strength $\tilde{\epsilon} = 6$ and the adjustable parameter $\gamma = 5$ in the nematic (at volume fraction $\phi = 0.3$), smectic A (at $\phi = 0.5$), and smectic A₂ (at $\phi = 0.7$) phases. In the inset, the same energy term $\beta\Delta U_{\text{SmA}_2}(z)$ calculated for the volume fraction $\phi = 0.5$ and the adjustable parameter $\gamma = 5$ in the smectic A (at attraction strengths $\tilde{\epsilon} = 0$ and 6), and smectic A₂ (at $\tilde{\epsilon} = 12$ and 18) phases. Note that the curves overlap for the same phase.

We employ the same procedure for $f(z)$, and find

$$f(z) = \frac{\exp \left[\delta \phi \sigma^2 \tilde{\epsilon} \sin \left(\frac{2\pi z}{2d} \right) \right]}{\int_{-\frac{d}{2}}^{+\frac{d}{2}} dz \exp \left[\delta \phi \sigma^2 \tilde{\epsilon} \sin \left(\frac{2\pi z}{2d} \right) \right]}. \quad (4.5)$$

We linearise the equations for the smectic and the anti-ferroelectric order parameters, given by Equations 4.2 and 4.3, in which we substitute the explicit expression for the density distribution of both the elongated particles $\rho(z)$ and the attractive tips $f(z)$, from Equations 4.4 and 4.5. From the linearisation, we obtain the following expressions for the order parameters:

$$\sigma^2 = \left(\frac{4}{\phi(\gamma + \tilde{\epsilon}\delta^2)} \right) \left(\frac{1}{2} - \frac{4}{\phi(\gamma + \tilde{\epsilon}\delta^2)} \right) \quad (4.6)$$

and

$$\delta^2 = \left(\frac{4}{\phi\sigma^2\tilde{\epsilon}} \right) \left(\frac{1}{2} - \frac{4}{\phi\sigma^2\tilde{\epsilon}} \right). \quad (4.7)$$

From Equation 4.6, we find that, in order that the smectic order parameter is positive, $\sigma \geq 0$,

$$\phi(\gamma + \epsilon\delta^2) \geq 2, \quad (4.8)$$

and, from Equation 4.7, we find that $\delta^2 \geq 0 \Rightarrow \phi(\gamma + \tilde{\epsilon}\delta^2) \geq 2$. From these results, we have that the transitions to the smectic A or smectic A₂ phases are continuous.

Alternatively, we recursively solve the coupled integral equations numerically for the smectic and the anti-ferroelectric order parameters, using the Mathematica software. We fix the value for adjustable parameter $\gamma = 5$ in order to shift the transitions volume fractions to values close to where we find the transitions in our simulations. The initial values for the smectic and the anti-ferroelectric order parameters is chosen to be 1. From each iteration, we obtain new estimates for σ and δ that are the input values to the next one. The volume fraction is fixed and increased from 0 to 1 in 30 steps. The sticking energy is also fixed at values between $\tilde{\epsilon} = 0$ and 24, which we increased at steps of 3 in each run of our numerical calculations. The convergence criterion is that consecutive integration results differ less than 0.001 for at least 10 iterations.

From the results obtained using the procedure described in the paragraph above, we calculate the values for the order parameters σ and δ , with which we classify the corresponding phase at the fixed set of sticking energy and volume fraction parameters. From this procedure, we obtain the phase diagram of perfectly parallel, hard rods that have a single attractive end. In Figure 4.15, we

present in (a) the smectic σ and anti-ferroelectric δ order parameters as a function of the volume fraction ϕ at sticking energy $\tilde{\epsilon} = 6$ (and $\gamma = 5$) and in (b) the phase diagram obtained from classification based on these order parameters. Notice that the numerical phase diagram shows that the nematic-to-smectic A transition is at $\phi = 0.4$, which is the value given by Equation 4.8 for $\delta = 0$ and the adopted value of $\gamma = 5$, as expected.

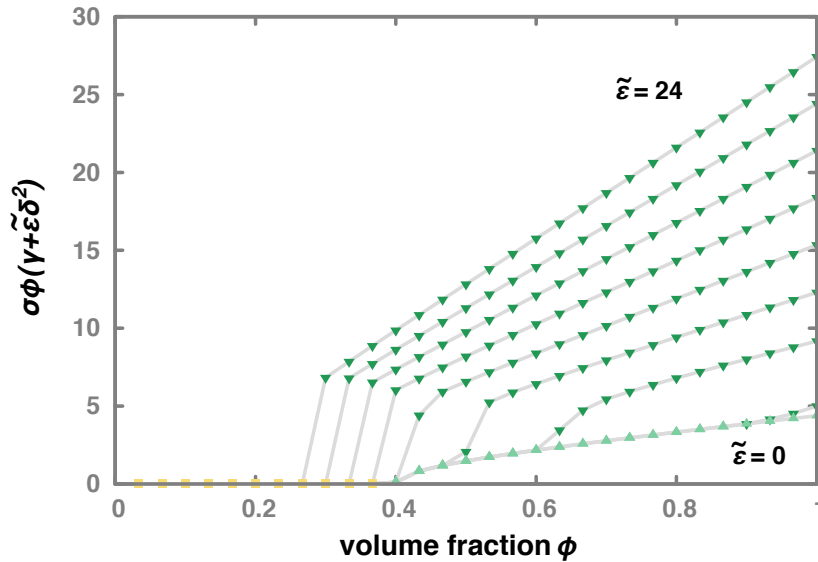


Figure 4.17: The height of the effective smectic ordering potential $\sigma\phi(\gamma + \tilde{\epsilon}\delta^2)$ as a function of the volume fraction ϕ for the attraction strengths $\tilde{\epsilon}$ from 0 to 24 with intervals of 3. The following phases are identified: nematic (yellow square), smectic A (green triangle up), smectic A_2 (dark green triangle down) phases. The linear dependence of the amplitude of the smectic ordering potential with the volume fraction is also what we find in our simulations. See inset in Figure 4.10(a).

From Figure 4.15 (a), we find that, unlike the corresponding order parameters obtained from our simulations, there is a shoulder in the smectic ordering parameter at the volume fraction where the anti-ferroelectric phase transition occurs. It indicates that the particles become more strongly ordered along the director as the rods transition to the smectic A_2 phase. The effect is not captured by the smectic order parameter in our simulations but this could be due to the limited resolution in our simulations. For a comparison, see the inset in Figure 4.8 (a). From Figure 4.15 (b), we find that our model captures the destabilisation of the nematic phase in favour of the smectic A_2 but the same is not true for the smectic A. In this case, the phase transition is independent of the sticking energy. Nevertheless, the destabilisation of the smectic A in favour of the smectic A_2 phase seems to represent what is seen in the simulations. From Figure 4.16, we find that the height is approximately the same in each phase, independently of the attraction strengths between tips, unlike what we find in the simulations. The

same is true for the width of the smectic ordering parameter. It is independent of both the attraction strength and the volume fraction.

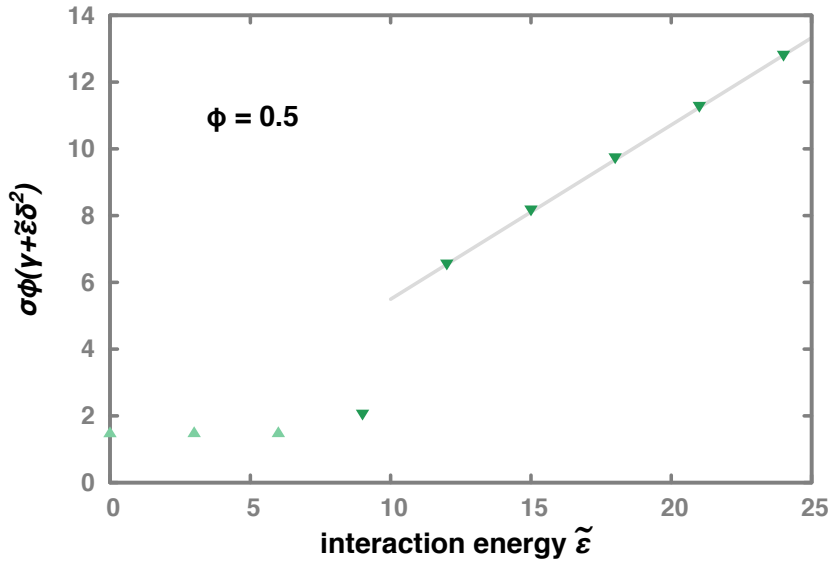


Figure 4.18: The height of the effective smectic ordering potential $\sigma\phi(\gamma + \tilde{\epsilon}\delta^2)$ as a function of the attraction strength at the volume fraction 0.5. The following phases are identified: smectic A (green triangle up) and smectic A₂ (dark green triangle down) phases. The linear dependence of the amplitude of the smectic ordering potential with the attraction strength is also what we find in our simulations. See Figure 4.10(b).

The height of the effective smectic ordering potential is given by $\sigma\phi(\gamma + \tilde{\epsilon}\delta^2)$. See Equation 4.4. This quantity is represented both as a function of the volume fraction for all the attraction strengths investigated (Figure 4.17) and as a function of the attraction strength for the volume fraction 0.5, in which only the smectic A and smectic A₂ phases are found (Figure 4.18). From the comparison between Figure 4.17 and the inset in Figure 4.10 and between Figure 4.18 and the Figure 4.10 itself, we find that the theory emulates the linear dependence of the height of the smectic ordering potential as a function of the volume fraction and of the attraction strength except for the angular coefficient depending on the phase. The same is true for the width of the smectic ordering potential that does not decrease as the attraction strength increases but is constant as can be seen in Figure 4.16.

Acknowledgments

We thank Thijs van der Heijden for the assistance in implementing the numerical integration of the equations presented in the appendix of this chapter.

Chapter 5

Dynamics of elongated guest particles in the smectic A phase

Rod-like colloidal particles self-assembled in a smectic A phase exhibit an unusual hopping-type of diffusion between the layers and quasi two-dimensional diffusion within the layers. Recent experiments show that rod-like guest particles dispersed in the smectic diffuse faster along the director than the host particles do but only if they are incommensurately longer than these. In order to understand why this is so, we perform molecular dynamics computer simulations on semi-flexible guest particles of contour length ranging from 0.3 to 2 times the contour length of the host particles. We also investigate the impact of the bending flexibility of the guest particles on their diffusivity along and perpendicular to the director. We show that the faster layer-to-layer diffusion is characterised by more frequent jumps between the layers and, consequently, a shorter residence time in them. Interestingly, it seems that the persistence length does not play a significant role in the diffusion process of the guest particle. We argue that this might be due to the resolution of the bead-spring chain model that we employ in our bead-chain particles: in all cases studied the deflection length seems to be of the order of magnitude of a particle bead. As a consequence, flexibility is not able to facilitate the penetration into a neighbouring smectic layer. We conclude that the longer guest particles we tested are the fastest particles, in particular guest particles with an incommensurate contour length of ~ 1.7 the contour length of the host particles. For this case a larger persistence length also leads to a larger diffusivity.

5.1 Introduction

The diffusion of elongated colloidal particles presents interesting and sometimes counterintuitive features, depending very much on the underlying symmetry of the phase in which they find themselves. For example, in the smectic phase, which is characterised by (quasi) long-range one-dimensional translational order, recent experiments indicate that particles engage mostly in a layer-to-layer, hopping-type diffusion strongly affected by both their bending flexibility and aspect ratio [33, 38, 48, 49]. This type of motion is linked with the periodic molecular field created by the surrounding particles, also called the smectic ordering potential [85]. The congested nature of the smectic phase requires a cooperative motion of strings of particles, in order to create an empty space for every diffuser part of these strings that are also referred to as *vortices* on account of their closed-loop character [47, 86].

Recent experiments at the Centre de Recherche Paul-Pascal in Bordeaux, France, show that long guest particles in the smectic A phase formed by shorter host particles diffuse faster along the director than the host particles themselves [41]. Such behaviour seems unusual in highly congested dispersions such the smectic phase. The host and guest particles used in the experiments referred to are the filamentous fdY21M and M13K07 viruses, and constructs thereof. The values of the contour length L and persistence length L_p of these particles are tabulated in Chapter 1, Table 1.1. From the values of the persistence lengths of the viruses, we calculate their structural “flexibilities” as L/L_p that we present in the Table 5.1 below. Indicated also are their role as guest or host particle, as well as the calculated values of the ratio between the contour length of the particle and the host fdY21M virus L/L^{fdY21M} . In the table, $2\times$ fdY21M and $3\times$ fdY21M refer to engineered “multimeric” viruses that have 2 and 3 times the length of the fdY21M particle. If we assume that their persistence length is left unchanged by the engineering, the flexibility of these multimeric guest particles are approximately 0.2 and 0.3.

	role	L/L^{fdY21M}	L/L_p
fdY21M	host	1	0.1
M13K07	guest	1.3	0.4
$2\times$ fdY21M	guest	2	0.2
$3\times$ fdY21M	guest	3	0.3

Table 5.1: Guest and host particles employed in the experiments as reported in Reference [41]. For each of them, we calculate the ratio between the contour length of guest and host particles L/L^{fdY21M} and the ratio between the contour and persistence length of the particle L/L_p .

From Table 5.1 we notice that long guest particles of three different contour lengths are employed in the experiments. One particle has an “incommensurate” contour length that is approximately 1.3 times longer than the contour length of the host particle. “Incommensurate” here refers to an incompatibility with the smectic layer spacing, which is approximately equal to the particle length and that is also approximately equal to the interlayer spacing, as the particle is semi-flexible [32]. The other two guest particles are even longer, but do have a commensurate contour length of 2 and 3 times the contour length of the host particle. Between all, the former turns out to be the fastest diffuser, presumably because its larger and non-commensurate length create voids in the adjacent layers facilitating the diffusion through them [41]. This fastest guest particle also happens to have a different persistence length from that of the host and the *commensurate* guest particles. Confusingly, the flexibility, as we define it, is not kept constant for the various particles of the experiment. Therefore, the observations must be a result of the combined effect of contour and persistence length, implying that the explanation remains tenuous and requires further study. We note that both the stability of the smectic A phase and cage-scape dynamics are strongly affected by both the aspect ratio and the flexibility of the particles [21, 23, 31, 39, 66, 87].

The quoted experiments of Reference [41] are the inspiration for the simulation study that we present in this Chapter. Aim is to address the question of in what way anisotropy and particle flexibility of elongated tracer particles affect their diffusion in a smectic A host phase. In Section 5.2, we explain the methods that we employ to investigate the most salient features of these particles dynamics. In Section 5.3, we characterise the in-layer diffusion as well as the diffusion of the guest particle through the smectic layers. In Section 5.4, we focus on diffusion through the layers. There, we characterise in more detail the hopping-type diffusion referred to above, and discuss the relevant parameters in the diffusion of the guest particles. Finally, in Section 5.6, we present our main conclusions.

We note that for the simulations presented in these sections, we keep the persistence length L_p of our particles constant, rather than the flexibility L/L_p . We do this because we already vary the contour length L of the particle to investigate the effect of the various ratios between the contour length of guest and host particles on the dynamics of guests in the smectic phase.

5.2 Methods and Analysis

Our particles are modelled as harmonic bead-spring chains, described in detail in Chapter 2. We recall that the energy of each bond of length s is given by $U = 1/2\kappa_s(s - D/2)^2$, where $\kappa_s = 100 k_B T / D^2$ is the harmonic elastic con-

stant. Because the mean bond length is not fixed, the contour length of the particle is strictly speaking not constant but depends on the pressure. For simplicity, we choose to ignore this in this chapter and refer to the contour length as $L = (b - 1)D/2$, where b is the total number of overlapping beads in the chain. The persistence length is also dependent on the bond length s . Employing the same convention, we set $L_p = \kappa_\theta s/k_B T = \kappa_\theta D/2k_B T$, where κ_θ is the harmonic elastic constant.

We study the diffusion of guest particles in a smectic A phase formed by host particles of contour length $L^{\text{host}} = 10 D$ and persistence length $L_p = 100 D$, so aspect ratio $L^{\text{host}}/D = 10$ and flexibility $L^{\text{host}}/L_p = 0.1$. The number of beads b , contour length L^{host} , and persistence length L_p for the various particles employed are given in Table 5.2. In that table, we also present the ratios between the contour length of the guest and host particles $L^{\text{guest}}/L^{\text{host}}$. The contour length ratios of the guest and host particles are 0.3, 0.6, 1, 1.3, 1.7 and 2. For each guest particle we track the diffusion for two distinct values of the persistence length, $L_p = 100$ and $25 D$.

	b	$L^{\text{guest}} [D]$	$L_p [D]$	$L^{\text{guest}}/L^{\text{host}}$
guest 0.3	7	3	25 and 100	0.3
guest 0.6	14	6.5	25 and 100	~ 0.6
guest 1	21	10	25 and 100	1
guest 1.3	28	13.5	25 and 100	~ 1.3
guest 1.7	35	17	25 and 100	1.7
guest 2	42	20.5	25 and 100	~ 2

Table 5.2: Guest particles employed in our simulations. Indicated are the number of overlapping beads b , the contour length L^{guest} , the persistence length L_p , and ratio of the contour lengths of guest and host particles $L^{\text{guest}}/L^{\text{host}}$. Note that guest 1 with persistence length $L_p = 100 D$ corresponds to the host particle.

We equilibrate the simulation box at a constant number of particles of $N = 4600$, temperature T , and pressure P , following the Molecular Dynamics simulations procedure described in the Chapter 2. We set the temperature at $1 \epsilon/k_B$. The pressure is set at $P = 1.4 \epsilon/D^3$, which leads to particles in the smectic A phase at the volume fraction of $\phi = 0.5$. From our previous work, presented in Chapter 3, we find that the smectic layer for particles of aspect ratio $L/D = 10$ and flexibility $L/L_p = 0.1$ at this volume fraction is approximately $\lambda = 11.8 D$. We take λ as the length scale that we employ as distance unit for the dynamics along the director.

The initial configuration of our simulations consists of 16 layers of AAA stacked host particles in the simulation box. The particles are hexagonally organised in each layer. Approximately in the centre of every other layer, we substitute a host

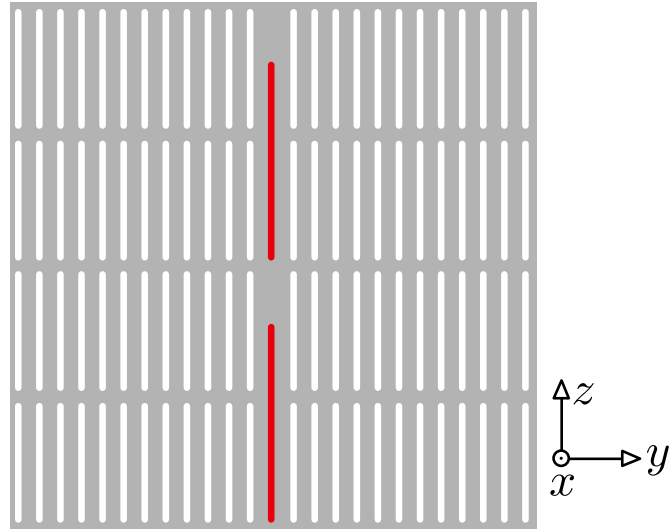


Figure 5.1: Schematic representation of the initial configuration. Approximately in the centre of every other layer we substitute a host (white rod) by a guest particle (red rod). In the neighbouring layers, the host particles with the corresponding positions are excluded in order to create space for the long guest particle.

particle for a guest particle. In the plane of the layer, the guest particle is placed as shown in Figure 5.1. The host particles in the neighbouring layers with the corresponding positions of the guest particle are excluded in order to create space for the long guest particle and avoid overlap with any host particles. This way, we have a total of $N = 4600$ particles in the simulation box, of which eight are guest particles.

We select five distinct equilibrium configurations, each one separated in time by more than two thousand timesteps to the other configurations. These configurations are employed as the initial configurations for Langevin Dynamics simulations that run for about 10^5 time units, corresponding to 2×10^8 timesteps of 5×10^{-3} time unit. We save configurations for each time unit, resulting in a total of 10^5 configurations. We apply the analysis procedure to the particles of all simulations, a total of 40 particles for each ratio and persistence length studied.

We explicitly investigate the motion of the guest particles perpendicular and parallel to the director \mathbf{n} . Due to the initial configuration, the director points approximately along the z direction, $\mathbf{n} \parallel \hat{\mathbf{z}}$. Therefore, we consider the perpendicular motion of the k -th guest particle as described by the coordinates $X_k(t)$ and $Y_k(t)$ of its centre of mass at time t , and the parallel motion as described by $Z_k(t)$. Typical traces of the particles are represented in Figure 5.2 for the case of $L_p = 100 D$, that is, a guest particle with the same bending stiffness as the host particles. We show the position of three guest particles $k = 1$ with different guest-to-host length ratios $L^{\text{guest}}/L^{\text{host}}$ 0.6, 1 and 1.3, focusing on the motion

in the $x - y$ plane and along the director, corresponding to the z direction as a function of time. Shown are the traces $X_1(t) - X_1(0)$ and $Y_1(t) - Y_1(0)$ (top, (a)), and the position $Z_1(t) - Z_1(0)$ (bottom, (b)). Note that in the figure, the particles coordinates are not wrapped at the periodic boundaries, and that the grey box represents the simulation box dimensions in each direction.

From Figure 5.2 (a), we find that the perpendicular or in-plane movement can be described as a conventional Brownian motion, while from Figure 5.2 (b) we conclude that the movement perpendicular to the director is characterised by a short-time rattling and a hopping-type Brownian motion on sufficiently long time scales. A particle rattles within a smectic layer, until it hops to another, neighbouring smectic layer. This means that, for short times, the particle's motion is constrained by a molecular confinement field provided by all other particles in the simulation box, the so-called smectic ordering potential. We employ the in-layer rattling to calculate the smectic ordering potential as to be explained in more detail below.

The figure suggests that guest particles shorter and longer than the host particles cover more distance within the same time and hence diffuse faster, both in the xy -plane, so within a smectic layer, and along the z -axis (the director). That longer particles would be faster is unexpected, given that their self-diffusivities [in the dilute regime](#) are smaller as these scale with reciprocal length of the particles [88]. This implies that this finding must be due to the interaction with the host particles, e.g., associated with caging phenomena of the effective molecular field they experience from the host particles.

To make the analysis more quantitative, we evaluate from the trajectories of all guest particles the mean-square displacement (MSD) for the movement in the xy -plane and along the z -axis. We also evaluate the number of jumps between layers, and the residence time of the guest particles in a layer. The procedure we follow to obtain these values we explain in the next paragraph. Because we employ bead-spring chains to model our particles and invoke Langevin dynamics simulations, longer particles are subject to a larger friction proportional to the number of beads that make up the chain, as already alluded to. Therefore, in order to compare the MSD of the various guest particles, and compensate for the effect of the friction, we multiply the value of the MSD obtained from the simulations by the number of beads b that make up a particular guest particle. Similarly, the same procedure is performed for the number of jumps, while the residence time in a layer, on the other hand, is divided by the number of beads.

To extract the long-time diffusivity, and correct for the friction, we divide the MSDs scaled by the number of beads $b \times \text{MSD}$ and by the time interval Δt . For late times, we expect an approximately constant value as function of the time interval Δt . This value represents the long-time diffusion constant, denoted \mathcal{D} .

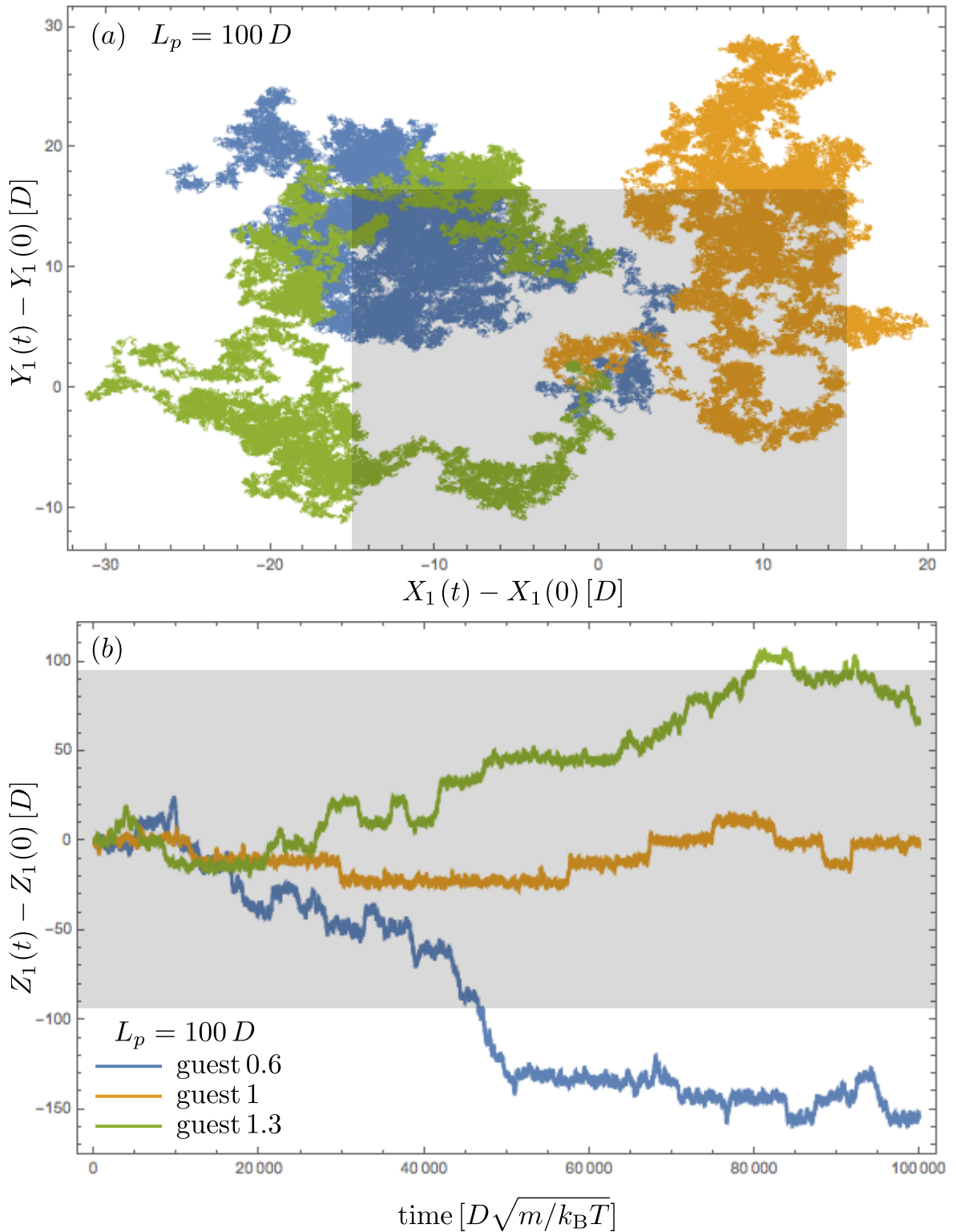


Figure 5.2: Traces of guest particles perpendicular and parallel to the director \mathbf{n} for one particle of the guest 1 ($L^{\text{guest}} = 10 D$), guest 0.6 ($L^{\text{guest}} = 6.5 D$), guest 1.3 ($L^{\text{guest}} = 13.5 D$) type of persistence length $100 D$. (a) The perpendicular in-plane movement shown in the xy -plane can be described as Brownian, mainly caused by the interaction with neighbouring particles, while (b) the movement perpendicular to the director is Brownian but resembles a hopping-type motion. The grey box represents the simulation box dimensions in each direction. The total diffusion time is equal in a) and b), and corresponds to 10^5 time units.

We estimate the diffusion coefficients perpendicular and parallel to the director, \mathcal{D}_\perp and \mathcal{D}_\parallel , by taking the average of $b \times \text{MSD}_\perp / \Delta t$ and $b \times \text{MSD}_\parallel / \Delta t$ from $\Delta t \geq 2000$ time units, which corresponds to $4\mathcal{D}_\perp$ and $2\mathcal{D}_\parallel$. We utilise this average of $b \times \text{MSD} \Delta t$ rather than the coefficients of the linear regression of the logarithm of the MSD as a function of the logarithm of the time interval Δt for two reasons. First, because of the limitations of our statistics which involves only 40 particles. Second, due to the presence of different and usually not distinct diffusion regimes involving ballistic, short-time and long-time diffusive behaviour, and crossovers between them. From the aforementioned linear regression, we obtain the diffusion exponent γ that we present in the next section.

Our procedure to obtain the smectic ordering potential, the number of jumps and the residence time in a smectic layer consists of two steps. First, we determine the positions of the centres of mass of the particles that are temporarily “trapped” in a smectic layer, which we find to coincide with the centres of that layer (to be discussed in more detail below). See Figure 5.3 (a). Second, we calculate the degree to which their instantaneous positions deviate from these positions. For the first step, we take the displacement along the director of all 8 guest particles in the simulation box and count the frequency of their positions in bins of $0.1 D$ length. We employ the function in the software Mathematica to find the position of the peaks, illustrated in Figure 5.3 (b).

For the next step, we compare the position of each guest particle with the list of peaks in order to determine the position where it is temporarily trapped. If in the next configuration the particle is located around another position, we count this as one jump. The interval between two jumps is the residence time of the particle k in a layer. We store the number of jumps J_k and the average residence time between jumps τ_k for the entire simulation time for each particle. We then take their averages, which include the data from the other 4 simulation runs, and study their distribution. The deviation of the instantaneous particle position to the *trapping* position Z_k^λ is stored for the calculation of the smectic ordering potential.

As discussed in Chapter 4, the smectic ordering potential ΔU describes the molecular field experienced by each individual particle in the smectic phase. In this case, because there are only a few particles in each configuration, it is obtained from the distribution of all guest particles positions p for the entire simulation. The distribution ρ is the frequency count of the various values of p in bins of $0.1 D$, divided by the maximum count of p . The smectic ordering potential ΔU is then related to ρ by $\rho \propto e^{-\Delta U/k_B T}$, as we assume a Boltzmann distribution. The smectic ordering potential presented here corresponds to the average over all five simulation runs (involving 40 particles). It is important to stress that, except for the short guest particles, an individual particle does not usually visit all lay-

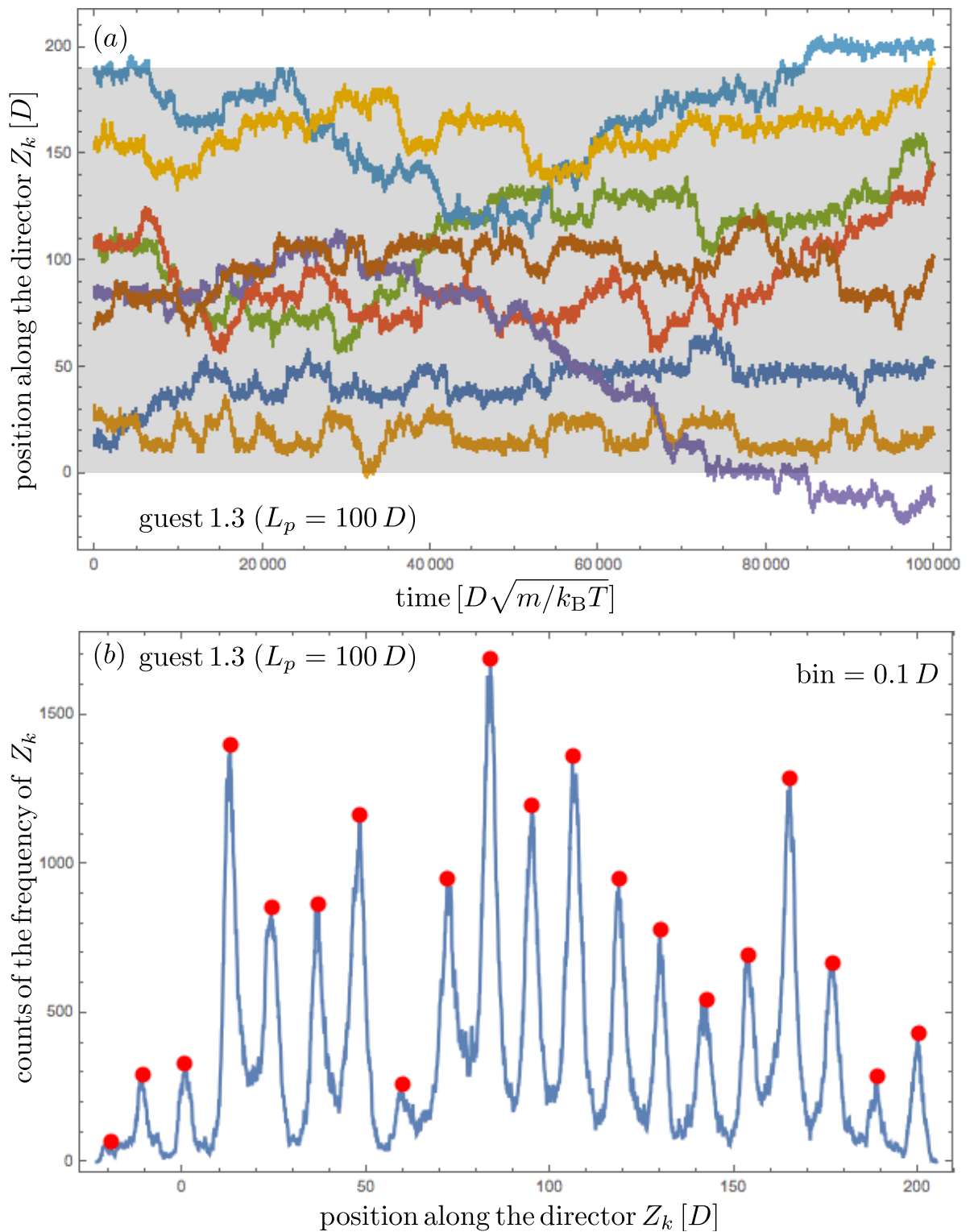


Figure 5.3: (a) The position along the director as a function of the simulation time for all 8 guest particles in the simulation box, each particle has its trajectory along the director represented by a different colour. The grey box represents the height of the simulation box. (b) The frequency count of positions in bins of $0.1 D$ as a function of the position along the director for guest 1.3 particles of persistence length $100 D$. The red dots represent the position where the particles are temporarily trapped in a smectic layer for approximately 520 time units, which is the average residence time for this particular guest particle.

ers in the simulation box within a simulation run. However, each layer is visited by at least one of the eight particles within a run, suggesting we are probing a sufficient number of configurations. This can be seen in Figures 5.2 and 5.3 from the comparison between the particles' trajectories with the dimensions of the simulation box, represented by the grey box.

We find from our simulations (results not shown) that the positions of the centres of mass of the guest particles represented in Figure 5.3 (b) correspond to the centres of the smectic layers. For this, we compare the centre of the distribution of the positions along the director of the host particles to the position of each particle at every configuration. The distribution of these values show that they are indeed usually located near the centre of the smectic layer. The distribution for guest 1 is the one with highest probability to be around the centre within a deviation of $\pm 0.5 D$, as to expected: guest 1 has the same length as the host particle. Interestingly, it is the shortest and the largest guest particles, that is guests 0.3 and 2, that are *more widely spread* around the centre of the smectic layer. For the guest 0.3, most of configurations are near the centre of a layer, but exhibit a deviation of about $\pm 2 D$, indicating that this is probably due to an in-layer rattling. For the guest 2, we expect that such a wide distribution is due to permeation to adjacent layers already partially occupied by the particle, allowing for significantly more rattling space than the host particles have.

5.3 Characterisation of the dynamics

In this section, we characterise the dynamics of the guest particles perpendicular and parallel to the director, $\hat{\mathbf{n}}$, which is parallel to the z axis. A taste of this was already given in the previous section, in Figure 5.2, representing the host (guest 1), a short guest particle (guest 0.6), and a long guest particle (guest 1.3) of persistence length $L_p = 100 D$. These already indicate some of the findings that we confirm more quantitatively in this section. We recall that from Figure 5.2 (a) we find that the random displacement of the particles perpendicular to the director does not appear to be very strongly influenced by the difference in contour length between the guest and the host particles. Figure 5.2 (b) shows that the displacement along to the director is of a hopping-type, as the particles remain in a layer for some time and jump to another layer several times during the simulation run. In this case, unlike the displacement perpendicular to the director, both the short and long guest particles seem to diffuse faster, as we observe a larger number of jumps within the simulation time. In line with what is found experimentally [41], the hopping-type diffusion of shorter and longer guest particles is not sluggish as that of the host particles, where we note that the guest 1 of persistence length

$L_p = 100 D$ corresponds to the host particle. Therefore, host particles stay longer in a given smectic layer than shorter or longer guest particles, which results in a longer residence time.

From the traces of all 40 guest particles of each contour and persistence length considered, we calculate the MSD parallel and perpendicular to the director in order to quantify the diffusion. In Figure 5.4, we present the average of $b \times \text{MSD}$ along and perpendicular to the director, which we respectively denote $b \times \text{MSD}_{\parallel}$ (a) and $b \times \text{MSD}_{\perp}$ (b), for the host and guest particles of persistence length $L_p = 100 D$. We obtain the diffusion exponent γ from the time evolution of the MSD for the perpendicular and parallel displacement for all cases, $\text{MSD} \sim \Delta t^\gamma$. These values are mostly around unity and all of them are larger than 0.83, as can be seen in the Table 5.3. Therefore, we find that the particles are for all intents and purposes diffusive in both directions, as expected from the displacement of these particles presented in Figure 5.2. For the displacement along the director, we note that this is only true for larger time scales, as to be expected.

	$L_p = 100 D$		$L_p = 25 D$	
	MSD_{\parallel}	MSD_{\perp}	MSD_{\parallel}	MSD_{\perp}
guest 0.3	0.974	0.988	0.940	0.960
guest 0.6	1.009	0.834	1.036	0.999
guest 1	0.918	0.955	0.972	1.028
guest 1.3	0.990	1.064	1.046	1.066
guest 1.7	0.949	1.058	0.827	0.941
guest 2	1.026	0.941	0.980	0.967

Table 5.3: The scaling exponent γ from the time evolution of the MSD for the perpendicular and parallel displacement for guests particles of persistence lengths $L_p = 100$ and $25 D$.

The insets in Figure 5.4 give the same $b \times \text{MSD}$, but now divided by the time interval Δt in the linear scale, starting from 2000 time units. As can be seen from these insets, the values of $b \times \text{MSD} / \Delta t$ are not exactly constant, despite the fact that values of the diffusion exponent γ are very close to unity, presumably due to insufficient statistics.

In Figure 5.5, the diffusion coefficients perpendicular and parallel to the director, \mathcal{D}_{\perp} and \mathcal{D} , for all guest/host particle ratios and persistence lengths are represented. Note these diffusion coefficients are scaled by the number of beads b . Error bars indicate the standard deviation obtained from our data. A first approach to provide an order of the various diffusers by their relative speed from slowest to fastest, is to compare the values of the diffusion constants for the guest particles. Figure 5.5 (a) shows that the scaled diffusion coefficients perpen-

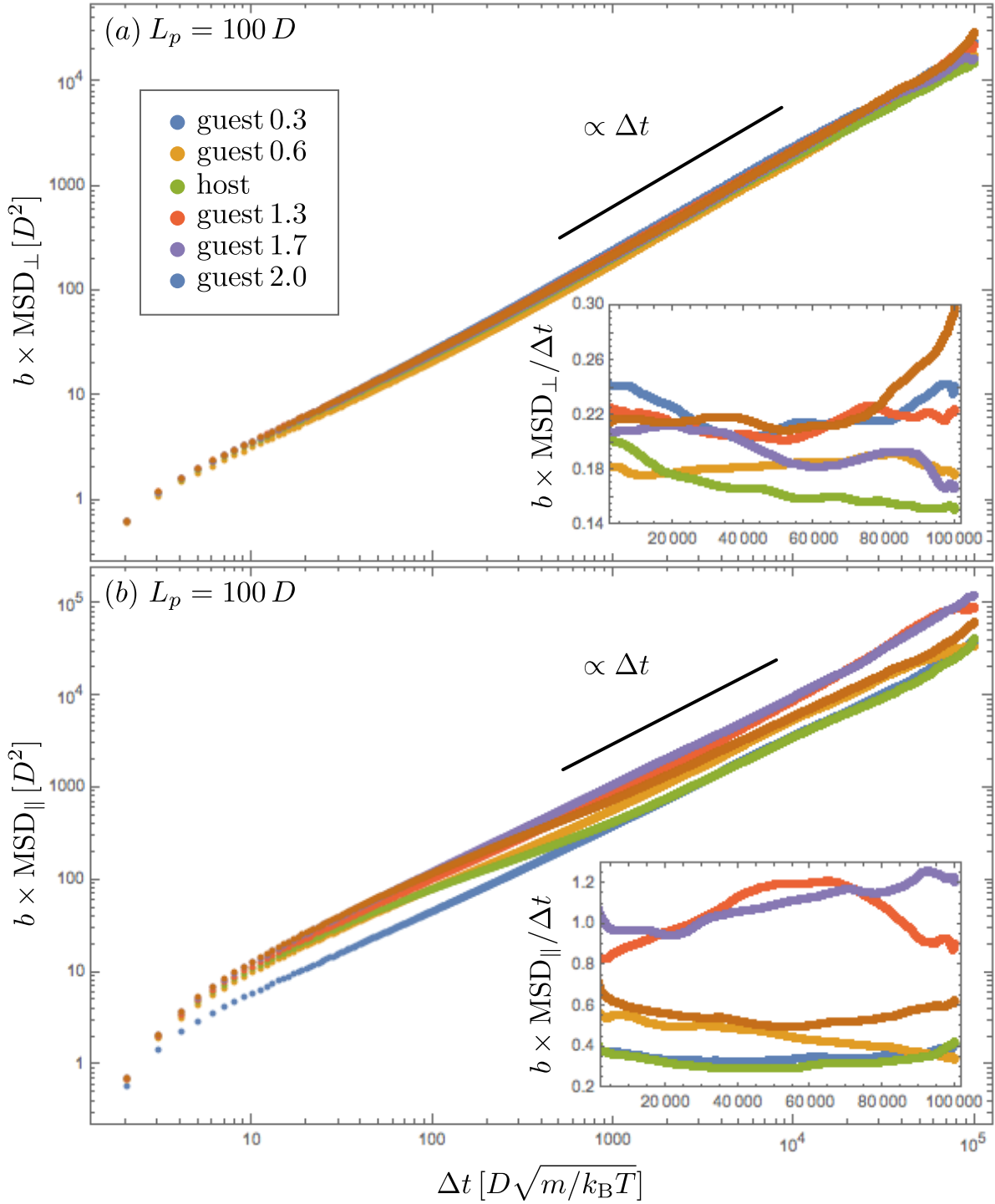


Figure 5.4: (a) Scaled MSD perpendicular and (b) parallel to the director for the host and guest particles of persistence length $L_p = 100 D$ diffusing in the smectic A phase at volume fraction $\phi = 0.5$. The MSD is scaled by the number of beads b that compose the guest particle. The insets represent the same MSD divided by the time interval Δt on a linear scale, starting from 2000 time units. See also Table 5.2.

pendicular to the director cannot reasonably make a distinction between the various ratios and contour lengths studied, as the differences in values are quite limited in magnitude. In other words, the diffusion perpendicular to the director is similar for all ratios and persistence lengths considered, if we scale out the trivial dependence on their length.

In Figure 5.5 (b), we present the (scaled) diffusion coefficients parallel to the director. In this case, we notice that the non-commensurate long guests are the fastest. The trend is upwards: diffusivity increases with the length ratio. The relation is not strictly linear nor monotonic, however, as we can identify two peaks. The first peak is around the ratio $L^{\text{guest}}/L^{\text{host}}$ of 0.6, and the second around 1.7. This indicates that short guests may diffuse faster than host particles, even we correct for the difference in fraction. If we consider the average value of the $b \times \text{MSD}$ divided by Δt , we find the following sequences (ordered from the slowest to the fastest diffusors): guest 1 (or host), guest 0.3, guest 0.6, guest 2.0, guest 1.3, and guest 1.7, for the persistence length $L_p = 100 D$; and guest 0.3, guest 1.0, guest 0.6, guest 2.0, guest 1.3, and guest 1.7 for the persistence length $L_p = 25 D$.

Note that we also find no clear trend of how flexibility influences the diffusion of the guest particles. We discuss this further in the next section, in which we focus on the diffusion along the director.

5.4 Hopping-type diffusion

The results presented in the previous section are supported by our analysis of the average number of jumps of a guest particle during the simulation time over all 40 particles \bar{J} . We evaluate this quantity, scaled by the number of beads b to account for differences in friction, as a function of the ratio between the contour length of guest and host particles for guests of persistence length $L_p = 100$ and $25 D$. Results are presented in Figure 5.6.

Notice the direct relation between Figures 5.5 (b) and 5.6 (a) with the exception of flexibility effects. Similarly to Figure 5.5 (b), we also find two peaks in Figure 5.6 (a), indicating that an increase in jump frequency is at the root of the faster diffusion of guests 0.6 and 1.7. Still, it is the non-commensurate long guest particle 1.7 that exhibits the fastest diffusion. In other words, the *optimal* length ratio for the fastest diffusion must be around 1.7.

Even though the figures present the same trends, there is a difference if we focus on the effect of the persistence length of the fastest diffuser. Again, the impact of bending flexibility on the dynamics seems relatively weak. From the analysis of the diffusion coefficient, the fastest diffuser is the guest 1.7 with a persistence length $L_p = 100 D$, while from our analysis of the number of jumps,

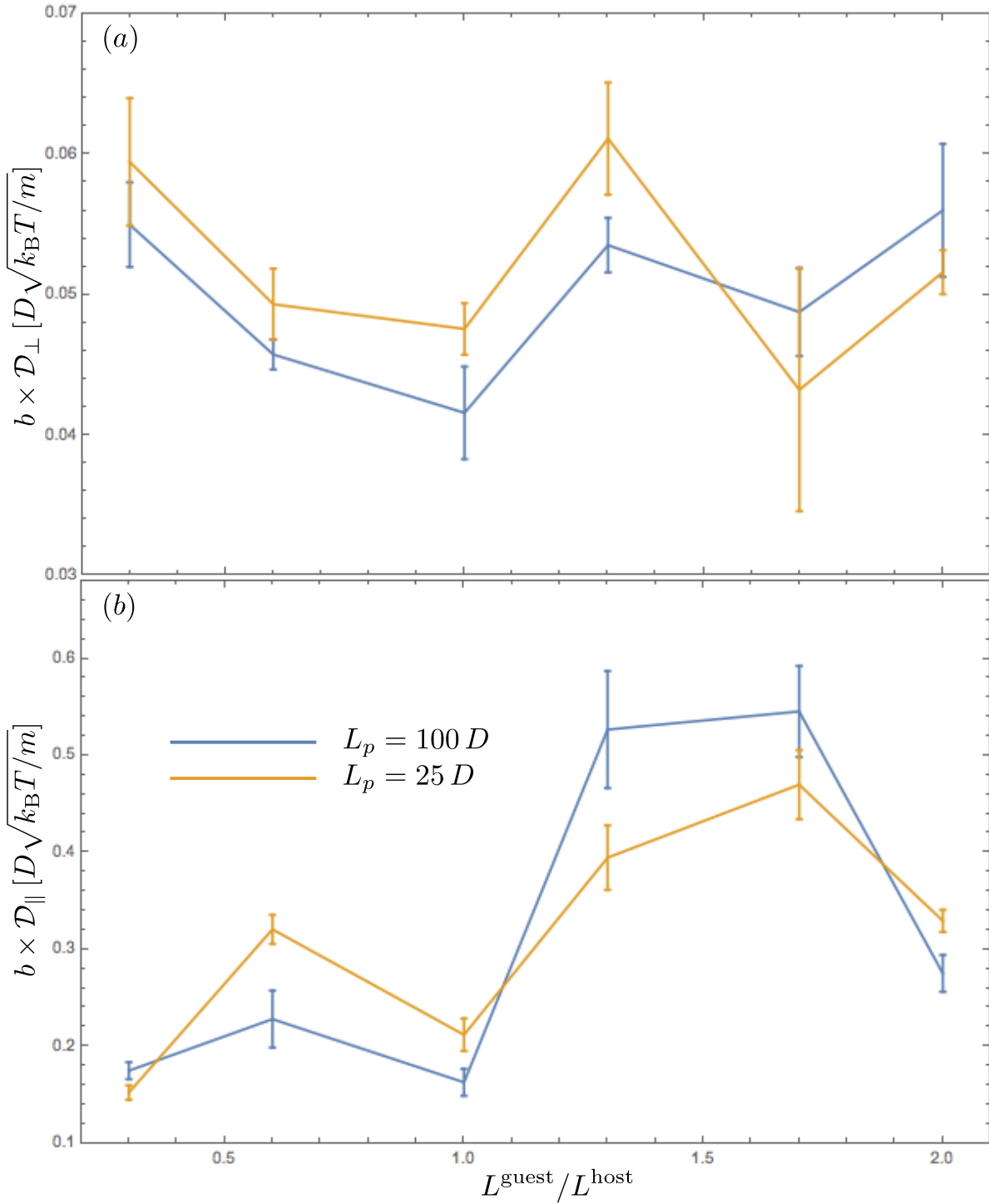


Figure 5.5: (a) Scaled diffusion coefficient perpendicular to the director \mathcal{D}_\perp and the (b) diffusion coefficient along the director \mathcal{D}_\parallel for particles in the smectic A phase at volume fraction $\phi = 0.5$. Values are calculated from the average value of the $b \times \text{MSD}/\Delta t$ as a function of the ratio of the contour length of the guest and the host particles $L^{\text{guest}}/L^{\text{host}}$ for the persistence lengths $L_p = 100$ and $25 D$ of the guest particles.

it is the same length ratio but the particle with persistence length $L_p = 100 D$ wins out in this case. From our findings, it seems justified to conclude that the impact of flexibility is not always to increase the jump frequency, even though this might be expected (see below). It depends also on the length ratio considered. For example, a similar effect presents itself for the commensurate length ratios 1.0 and 2.0.

A measure related to the average of the number of jumps is the average residence time in the simulation run over all 40 particles $\bar{\tau}$, that we again divide by the number of beads b and probe as a function of the ratio between the contour length of guest and host particles for guests of persistence length $L_p = 100$ and $25 D$. See Figure 5.6 (b). The average residence time is approximately inversely proportional the average of the number of jumps, therefore presenting valleys instead of peaks near the ratios 0.6 and 1.7. This implies our findings are internally consistent, as they should.

In order to come to some sort of understanding of these findings, in Figure 5.7, we present the mean smectic ordering potential as a function of the z position relative to the smectic layer. This is done for all ratios of the guest/host contour lengths with persistence lengths $L_p = 100$ (a) and $25 D$ (b) of the guest particle. By comparing what we find from the smectic ordering potential in the light of the order of the diffusers by their speed, discussed above, we infer that not only the height of the smectic ordering potential but also the *shape* must be relevant to their dynamics. For example, for the guest 2.0, the smectic ordering potential for persistence lengths $L_p = 100$ and $25 D$ are comparable in height, but that of the latter is much wider. This is in line with our finding that the more flexible guest 2.0 diffuses faster than its stiffer version. Note that the shapes of the smectic ordering potential are actually quite different for the different guest particles, where in particular that of guest 1.7 springs out from the rest.

In spite of this, there is an interesting similarity of the potentials for positions very near the smectic layer centre ($Z_\lambda = 0$). Indeed, it seems that the shape of the potential is the same independent of the particle contour length and persistence length. Beyond this region, the smectic potentials diverge from each other. Near $Z_\lambda = \lambda/2$, a second regime presents itself near the transition zone between smectic layers. Here the potential rise fast with position. Because few particles reside in that region, statistics are low. There, small differences in height are probably not statistically significant.

To highlight the differences in smectic ordering potential, we present in Figure 5.8 the same results but now separated by the contour length ratios $L^{\text{guest}}/L^{\text{host}}$, and focusing on the effect of flexibility. Note that the shapes of the curves vary significantly between the different length ratios, but less so between the two flexibilities for a given length ratio. We present the smectic ordering potential using

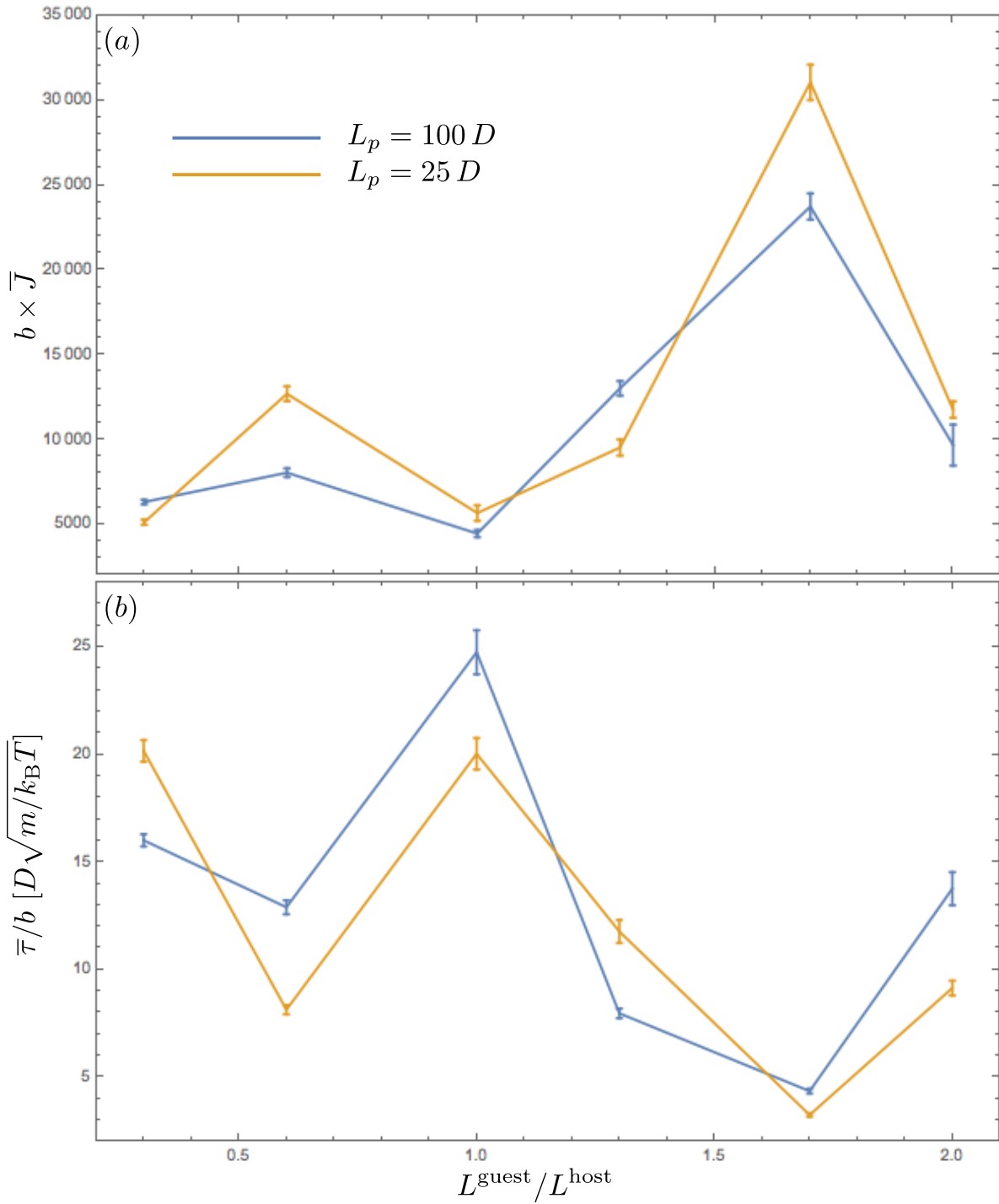


Figure 5.6: (a) Average of the number of jumps during the simulation time over all 40 guest particles \bar{J} (diffusing in the smectic A phase at volume fraction $\phi = 0.5$) times the number of beads b . (b) of the average residence time in the simulation run over all 40 particles $\bar{\tau}$ divided by the number of beads b in the guest chain as a function of the ratio between the contour length of guest and host particles for guests of persistence length $L_p = 100$ and $25 D$.

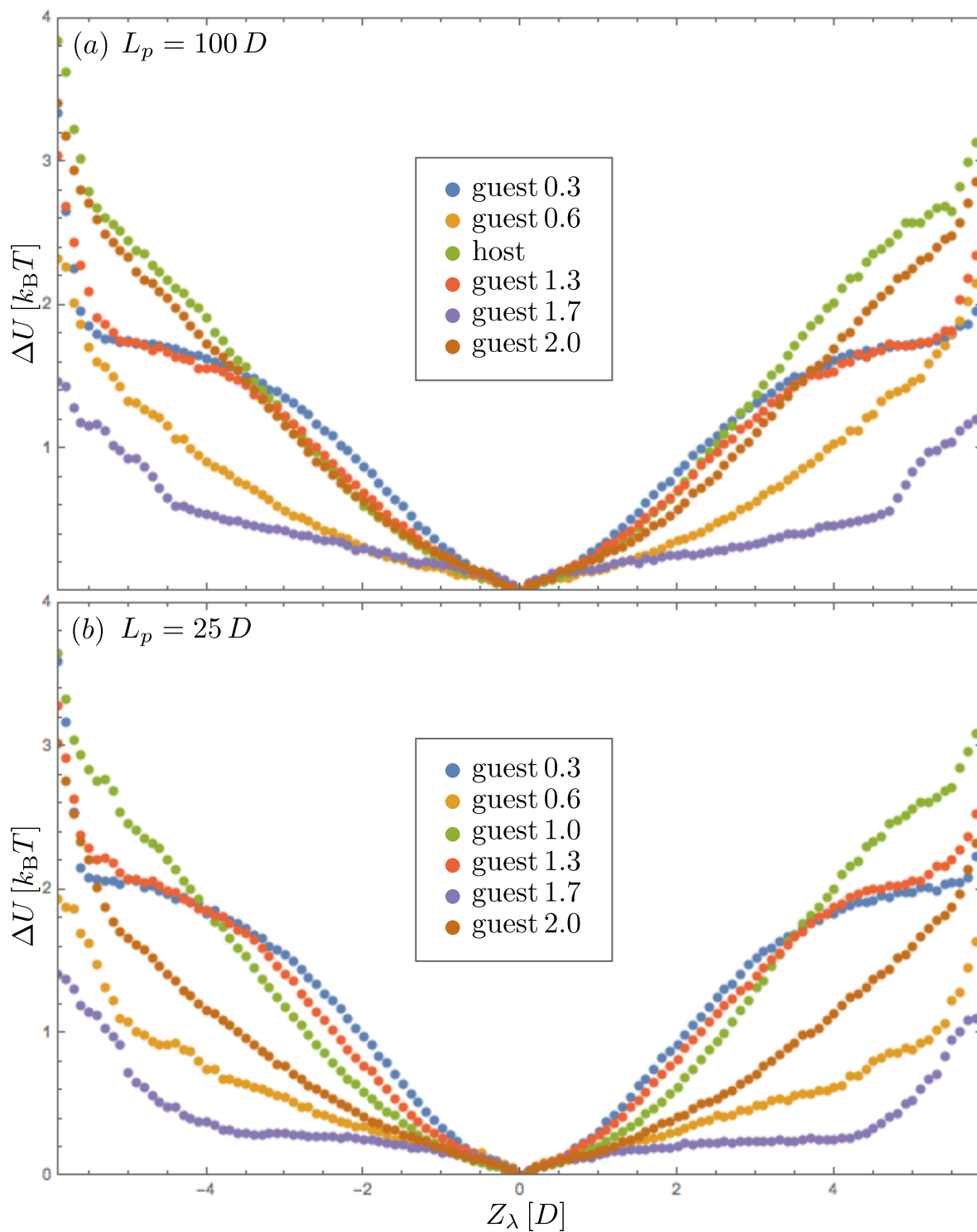


Figure 5.7: Smectic ordering potential as a function of the Z position along the director to the smectic layer. This is for all ratios between the contour length of the guest and host particles for (a) the persistence length $L_p = 100$ and (b) $25 D$ of the guest particle diffusing in the smectic A phase at volume fraction $\phi = 0.5$.

slightly different scales for the commensurate and incommensurate guest particle contour lengths, for it allows us to better appreciate the differences in shape. Notice that there are similarities between the smectic ordering potential curves that are paired in rows, so comparing the figure in the columns on the left and right.

In (a) and (d) the figure shows that the more flexible guests (for guests 0.3 and 1.3) experience a *larger* potential, indicating that they diffuse more slowly than the more stiff ones do. Nevertheless, the difference in height of about $0.25 k_B T$ remains rather small. This is probably the reason for the not-so clear trend we saw of the diffusivities in terms of the effect of flexibility on the diffusion. In figure (e), representing the guest 1 that has the same contour length as the host particles, they have nearly coinciding smectic ordering potentials (shape and height), yet we do observe small differences in the diffusivity and number of jumps show in our simulations, indicating that the more flexible host is the fastest in this case.

From the remaining figures (b), (e), and (f), we find that the potential is larger for the stiffer particle, and therefore the more flexible guest must arguably be the faster. The differences in shape of the smectic ordering potential seems to be the mostly influenced by contour length of the guest particle. It is only the guest 1.7 that shows a substantial difference in height of the potential. In comparison to the guests 1, which corresponds to the host particles themselves for $L_p = 100 D$, the smectic ordering potential is approximately $1 k_B T$ higher. For this case, the shape is also substantially different, showing an almost flat profile in the interval -4 to $4 D$, in which the value of the potential less than $0.5 k_B T$. This indicates that the particle may easily move between these positions in the smectic layer. This implies large fluctuations in the position relative to the centre of the layer.

The smectic ordering potentials that we just considered point at significant differences in the level of ordering of the guest particles in the smectic layers. This expresses itself also in the development of the self-van Hove function, as shown in Figure 5.9. In the figure we show the van Hove function at the time of 10^4 time units for all cases, for which time up to six jumps may be observed. From (a) to (e), the van Hove function is presented for each ratio of contour lengths of the guest and host particles. Indicated are results for the two values of the persistence length $L_p = 100$ and $25 D$ of the guest particle.

We do not correct for the larger viscous force felt by the longer rods and focus on the number of layers a particle visits during the time interval considered but rather on how distinct the peaks in the distribution are for each contour length ratio. In accordance with what we find in Figure 5.8, the van Hove function for guests 0.6 (b) and 1.7 (e) do not present very distinct peaks: this is not surprising giving that they also present the flattest smectic ordering potentials.

The peaks that we find for all guest particle lengths and flexibilities corre-

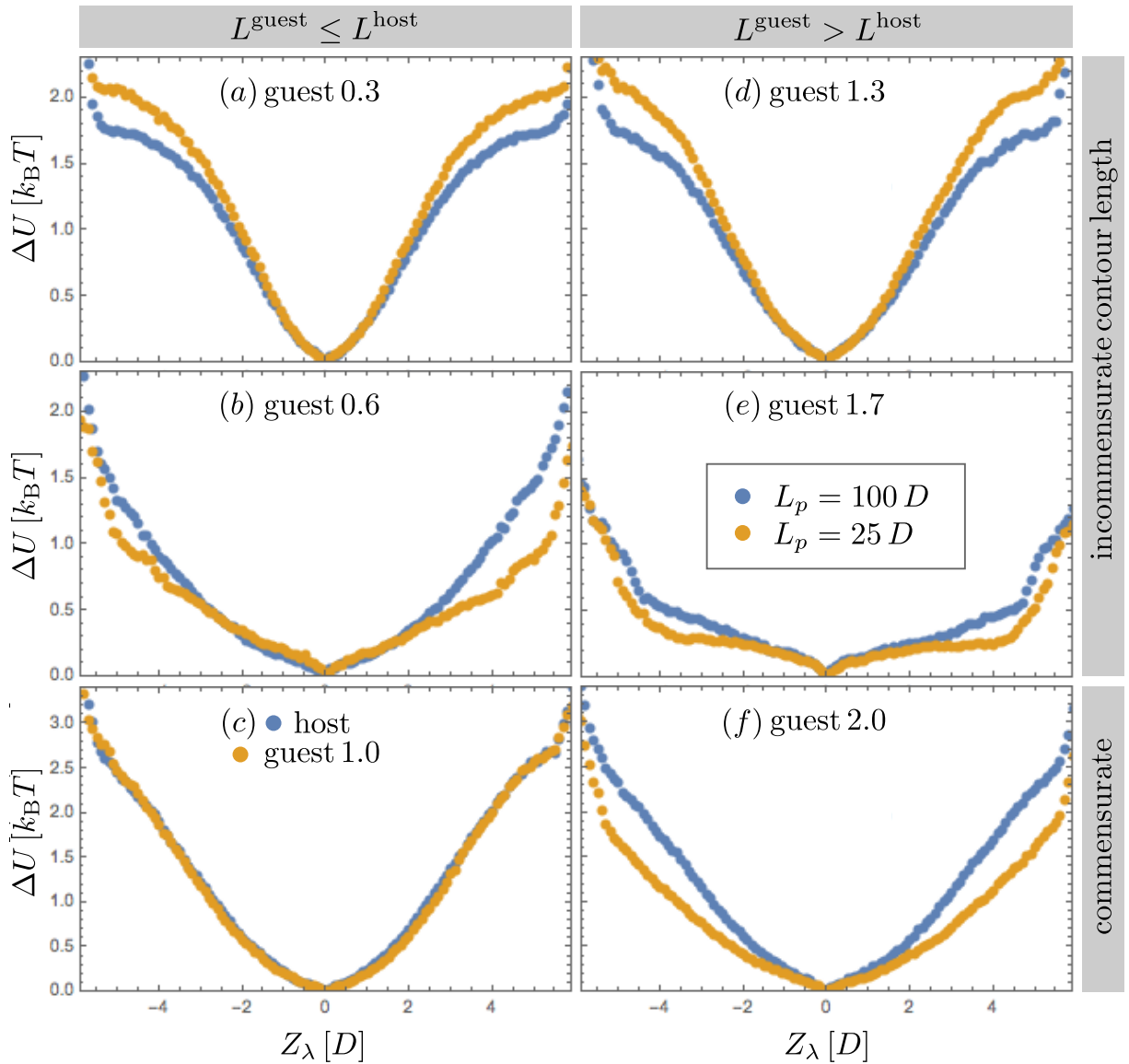


Figure 5.8: Smectic ordering potential as a function of the Z position in relation to the centre of the smectic layer for the persistence length $L_p = 100$ and $25 D$ of the guest particle, for ratios between the contour length of the guest and host particles $L^{\text{host}}/L^{\text{guest}}$ of (a) 0.3, (b) 0.6, (c) 1, (d) 1.3, (e) 1.7, and (f) 2. Note that the y-axis for the non-commensurate values (a), (b), (d), and (e) represents the interval $[0, 2.3]$ and for commensurate values (c) and (f) represents a larger interval $[0, 3.4]$. This way the height of the smectic ordering potential for these guests is higher and it is possible to better compare the shapes of the curves.

sponding to excursions to the nearest neighbour layer indicate a lower probability for particles whose contour length is commensurate with the contour length of the host particles in comparison to the other guest particles investigated. See in particular Figure 5.9 (c) and (f). Not surprisingly, these are also the slowest diffusers.

5.5 Deflection length

That aspect ratio must have an effect on the layer-to-layer diffusion of particles seems reasonable to assume, and we are seeing this in the diffusivities but not really in the free energy barriers between the smectic layers as we have seen in the previous section. This implies that layer-to-layer hopping might be dominated by particle density fluctuation necessary to transport a particle to a neighbouring layer, given that our smectic phase is very congested [85]. That in-layer diffusion seems also to be virtually independent of the length ratio suggests that caging by host particles involves correlated particles in neighbouring layers, which perhaps is not all that surprising, considering that the layer spacing is about one rod length and that guest particles make direct contact with the neighbouring layers too on account of their rattling.

What is also not intuitive is that we are not really seeing significant differences in the diffusive behaviour of particles with different bending flexibilities. More flexible particles should be able to escape a cage formed by host particles more easily than rigid ones, which seems to be true in isotropic dispersions [21, 89]. Whether this is true in liquid-crystalline phases has as far as we are aware not definitively been established but seems likely [90], but a simple analysis does suggest that for highly aligned particles flexibility must play a much smaller role in diffusive processes than in congested isotropic systems. Indeed, the alignment of the rod-like particles should strongly attenuate any bending modes that could assist in cage escape [21, 67].

To illustrate this, we investigate the orientation of the guest particles \mathbf{S}_k for all contour lengths and persistence lengths considered in this study. We take all the absolute value of the orientations of all guest particles $\|\mathbf{S}_k \cdot \hat{\mathbf{n}}\|$ as an estimate of the average orientation angle $\langle \theta^2 \rangle$ in the phase. With this value, we estimate the nematic order parameter \mathcal{S}_2 using the relation $\mathcal{S}_2 = 1 - 3\langle \theta^2 \rangle^2/2$. These values, as well as the values of the so-called Odijk deflection length λ_{Odijk} , are presented in Table 5.4 for guest particles of persistence lengths $L_p = 100$ and $25D$ [21]. The Odijk length measures the length scale over which a local bending fluctuation of a semi-flexible particle is directed back to the director.

We find that for all guest particles, except the shortest, the scalar nematic

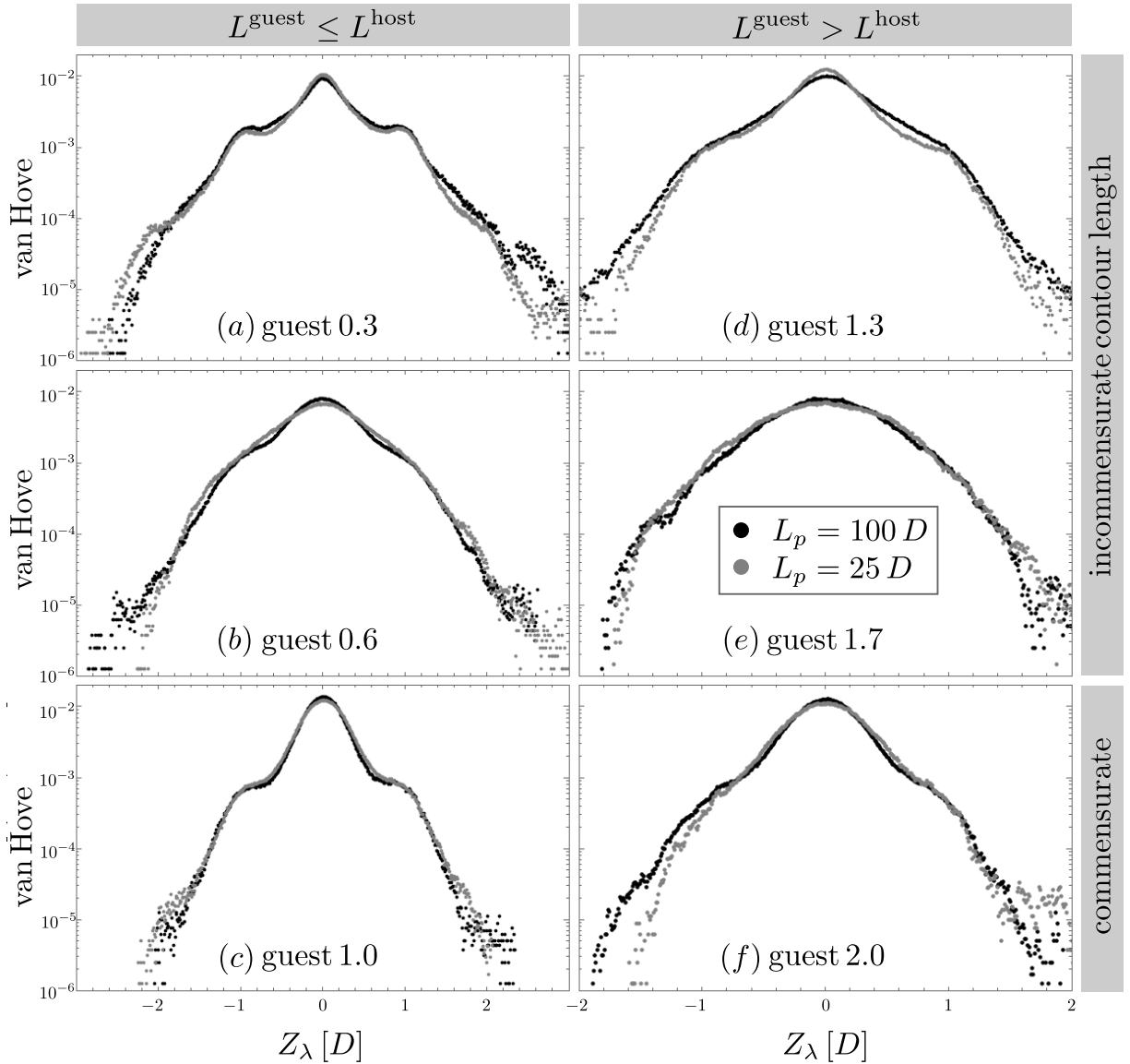


Figure 5.9: Van Hove function I as a function of the Z position in relation to the centre of the smectic layer for the persistence length $L_p = 100 D$ and $25 D$ of the guest particle, for ratios between the contour length of the guest and host particles $L^{\text{host}}/L^{\text{guest}}$ of (a) 0.3, (b) 0.6, (c) 1, (d) 1.3, (e) 1.7, and (f) 2. Note that the y-axis for the non-commensurate values (a), (b), (d), and (e) represents the interval $[0, 2.3]$ and for commensurate values (c) and (f) represents a larger interval $[0, 3.4]$. This way the height of the smectic ordering potential for these guests is higher and it is possible to better compare the shapes of the curves.

	$L_p = 100 D$		$L_p = 25 D$	
	S_2	$\lambda_{\text{Odijk}} [D]$	S_2	$\lambda_{\text{Odijk}} [D]$
guest 0.3	0.658	18.3	0.658	5.7
guest 0.6	0.949	3.4	0.938	1.0
guest 1	0.965	2.4	0.960	0.7
guest 1.3	0.968	2.1	0.961	0.6
guest 1.7	0.974	1.7	0.971	0.5
guest 2	0.972	1.8	0.975	0.4

Table 5.4: The nematic order parameter S_2 estimated from the orientation of the guest particles and the corresponding Odijk deflection length λ_{Odijk} for guests particles of persistence lengths $L_p = 100$ and $25 D$.

order parameter is close to unity. Consequently, the deflection length is equal to the particle width or even below that. This implies the particles behave more or less as rigid chains as bending modes are strongly suppressed by the ordering field. This in turns means that bending modes cannot assist the particles to find, say, a vacancy in the neighbouring smectic layers and hop to that layer. If the diffusion is not so much made possible by spontaneous openings of vacancies in neighbouring layers but by a concerted motion of particles across layers [47, 85], then finding partner particles that are able to engage in this kind of motion must also be much more difficult. Our results seem to suggest this.

5.6 Discussion and conclusions

In this Chapter we investigate by means of overdamped molecular dynamics simulations the impact on the single-particle dynamics of the contour and persistence length in a high-density smectic A phase consisting of slightly rigid, rod-like host particles. Interactions between all particles are purely repulsive and hence our study focuses specifically on lyotropic liquid crystals.

We find that for the diffusion perpendicular to the director, so within the smectic layers, contour and persistence length do not seem to play a very significant role if we correct for the length dependence of the solvent friction of the particles. For the diffusion along the director, non-commensurate short and long guest particles diffuse faster than commensurate ones, including and in particular those identical to the host particles. Remarkably, the by far fastest non-commensurate particle is *longer* than the host particles are. Our calculations show that this must be due to a much weaker and flatter molecular field that these particles experience by the host particles.

Interestingly, even though that the long commensurate guest 2.0 does not diffuse faster than the shorter guests 1.3 and 1.7, it is still, relatively speaking, as fast or even faster than the shorter commensurate and incommensurate particles. It seems that the *advantage* that a longer guest particle has is the partial penetration into the neighbouring layers, creating the space needed to diffuse along the director as in fact was also suggested in reference [41].

Remarkably, the persistence length of the guest particles does not seem to significantly change the trends that we observe with increasing contour length. This is unexpected for one would naively surmise that bending fluctuations of the particle help cage escape, in particular between layers. Nevertheless, suppression of bending modes by the molecular ordering field is possibly the root cause of our finding that bending flexibility does not strongly affect diffusion parallel and perpendicular to the director.

We realise that our results are tentative, in spite of the fact that in our simulations we consider a total number of 40 guest particles of a total of 4600 particles in the simulation box, and a total simulation time of 10^5 time units. This reasonably large number of guest particles and seemingly long simulation time still result in, e.g., mean-square displacements that bear the hallmarks of incomplete statistics. Indeed, the mean-square displacement divided by the time is not a strict invariant of time and shows long-time fluctuations. It may well be that much longer simulations are needed to unequivocally establish the impact of length on the diffusivity of the rod-like guest particles in a sea of host particles in the smectic A phase. We also surmise that much more finely grained bead-chain particles are needed to pinpoint the subtle effects of flexibility in this context.

Acknowledgments

We thank Rachel Armstrong for her help proofreading this chapter.

Chapter 6

Dynamics of clusters and percolation in the isotropic phase

In order to make headway in the field of dynamical percolation, relevant in the context of the fabrication of carbon nanotube nanocomposites, we study the statics and dynamics of geometric percolation of mutually repulsive particles, taking as a starting point spheres rather than tubes for reasons of simplicity. The question that we address here is whether geometric percolation exhibits critical slowing down expected because of the critical nature of the percolation transition. While we find that at the percolation threshold the size distribution of clusters is algebraic and scale free up to a certain cutoff, suggesting critical behaviour, tell-tale signs of a diverging time scale remain elusive. Interestingly, the connectivity length strongly impacts upon the survival dynamics of pairs of particle in clusters.

6.1 Introduction

There is a significant interest in the physics of continuum percolation of colloidal particles dispersed in a fluid host medium, on account of potential applications in photovoltaics, electromagnetic shielding, electromechanical energy conversion and actuation, and so on [91–93]. In these applications, one makes use of the collective properties of system-spanning networks of the in some sense connected particles. Connectivity may, for instance, be defined in terms of a length scale relevant to the efficient transport of charge carriers for electrical conductivity, that of energy for heat transfer, or the extent of charge separation for amplification of electrical permittivity [94]. Of particular interest are particles of very large aspect ratio, such as carbon nanotubes and graphene, as these tend to have a very low percolation threshold, that is, the minimum filler fraction required to obtain a system-spanning network in the host medium [95, 96]. In electrical percolation the conductivity of a composite increases very strongly with increasing filler fraction beyond the percolation threshold [93].

Although actual applications typically involve solid-state devices, their processing and manufacturing takes place in the fluid state. It is often thought that the properties of the final solid-state composites, in most cases involving host materials of polymeric nature, somehow reflect the collective properties of the particle networks in the fluid state prior to solidification [97]. The solidification process itself may involve the polymerisation of initially low-molecular weight compounds, compression moulding in the melt, spin and slot die coating from solution, and so on [93, 98]. Whilst by far most of the theoretical and simulation efforts in this field focus on the impact of the so-called formulation of the composite, that is, its composition [91, 96, 99–102], and presume thermodynamic equilibrium to apply, there are strong indications that liquid-state processing conditions also strongly affect the properties of the final product [97, 103, 104]. Most attempts to deal theoretically or computationally with any effects of out-of-equilibrium processes on percolation involve investigating the impact of external fields on particle alignment [105–107], although there are notable exceptions [108, 109]. The impact of elongational flow fields on alignment of rods can indeed be modelled at the level of an equilibrium theory [88], but such is not the case for that of shear fields [15].

Theoretically, the field of non-equilibrium percolation phenomena remains uncharted territory, although one would naively think that an extension of Schmolukowski theory should prove a promising starting point [110]. Notwithstanding that a connectedness percolation version of the framework of Schmolukowski theory would indeed seem promising, it would suffer from the same disadvantage as the original equilibrium version, which is that it deals solely with a few mo-

ments of the full cluster size distribution [94]. Indeed, connectivity percolation theory, which has at its root classical liquid state theory, focuses attention on the pair connectedness function, from which the mean aggregation number and mean radius of gyration of clusters may be calculated [105]. Hence, if interested in cluster dynamics, this avenue of theoretical investigation would provide limited information only.

It seems sensible, then, to opt for dynamical computer simulations and investigate the statics and dynamics of connectedness clustering of mutually repulsive spheres near the percolation threshold, making use of the so-called cherry pit model [94]. We focus on spheres rather than elongated particles for simplicity, because for the latter the clustering dynamics is impacted upon not only by translational diffusion but also rotational diffusion of particles. This should lead to very different buildup and breakdown dynamics of clusters, as we may deduce from the fact that the regression of concentration fluctuations is very different for interacting rod-like particles compared to that of spherical shape [111]. As this is a preliminary study, we limit ourselves to cluster dynamics in quiescent suspension, postponing shear-flow studies to future work.

While the dynamics of the clustering of spherical particles has been extensively studied in the context of the sol-gel transition of mutually attractive particles and the crystallisation of mutually repulsive particles [112, 113], little is known about the statics and dynamics of geometric clusters of repulsive spheres away from any actual phase transition, kinetic trapping or structural arrest. Hence to make headway in this field of study, we investigate average cluster distributions, temporal fluctuations in the average cluster size and pair survival times for conditions under which we expect percolation to occur on a macroscopic scale. We pinpoint these conditions by relying on the crossing of the percolation probabilities for different box sizes.

Even though in our finite simulation box the percolation probability is under those conditions not equal to unity, we do find universal cluster size distributions following a power-law distribution. This is indicative of critical behaviour [114]. The temporal autocorrelation function of the average cluster size, while somewhat noisy, seems to point at two time scales. This is confirmed by our calculated pair survival probability, which shows much cleaner statistics and clearly demonstrates the existence of two relevant time scales for the problem at hand. We associate the short time scale with individual particle movements, attaching and detaching from clusters, and the longer time scale with large-scale attachment and detachment processes involving groups of particles.

Interestingly, the short time scale is only weakly dependent on the connectivity range, while the longer time scale strongly increases with increasing connectivity range. However, both do not seem to be very sensitive to the system size.

This we interpret as there not being a diverging time scale at percolation, to be expected in the thermodynamic limit if percolation indeed is akin to a (second order) phase transition [15, 114]. A naïve diffusion model that we put forward in the Appendix 6.A also points at the existence of such a diverging time scale. It seems that more extensive simulations on much larger systems need to be done to confirm the absence of critical slowing down near percolation.

The remainder of this chapter is organised as follows. In Section 6.2 we present the methods and analysis procedures employed. In Section 6.3 we present the percolation threshold for three values of the connectedness diameter and two values of the box size. At the percolation threshold, we quantify the statics and dynamics of the clusters in the isotropic phase. These results are presented in Section 6.4. In Section 6.5 we present the main conclusions. In addition, we also present a simple argument for the diverging time scale in Appendix 6.A.

6.2 Methods and analysis

Computer simulations - We perform Langevin dynamics (LD) simulations using the simulation package LAMMPS on N mutually repulsive spheres in an implicit solvent. The particles have a mass m and interact by the Weeks-Chandler-Anderson (WCA) potential given in Equation 2.3 of Section 2.2. From this equation, we have the parameter D (which defines the particle diameter) and ϵ as our length and energy units. The temperature T is kept constant, $T = 1 \epsilon/k_B$. The particles reside in a cubic simulation box of fixed side L ranging between $10 D$ and $60 D$, with periodic boundary conditions. Initially, the particles are placed at random positions (pseudo-random generation using the time as seed) in the simulation box. If this leads to a configuration in which they partially overlap, the initial configuration is discarded. The particles are equilibrated for 2×10^5 timesteps or 1000 time units, where the time unit is given by $(m/k_B T)^{1/2} D$, at a given volume fraction $\phi = N \pi D^3 (6V)^{-1}$, where V is the volume of the box, $V = L^3$. The damping factor of the implicit solvent is 0.1 time units, which corresponds to a solvent viscosity of just below that of water. For the data acquisition run, the total simulation time t_s is such that the particles can explore the entire simulation box. In other words, the MSD at t_s has to be larger than $3L^2$ (cubic box diameter squared). We employ the mean-square-displacement (MSD) of the particles as a measure of the particle displacement. The configurations are recorded every Δt , a time interval chosen such that particles move on average half a diameter between two consecutive configurations: the values $t_s = 10^7$ and $\Delta t = 100$ timesteps satisfy these criteria, and produce a total of 10^5 configurations.

We perform our simulations for various values of the number of particles

N and box size dimension L . In each configuration, we classify these particles in clusters based on the distance between the particles. A cluster is formed by particles that are connected. The connectedness diameter d demarcates a maximum distance between centres of mass for two particles to be considered directly connected. This is known as the cherry pit model in continuum percolation [94], schematically represented in Figure 6.1. Two particles may also be indirectly connected by intermediate particles.

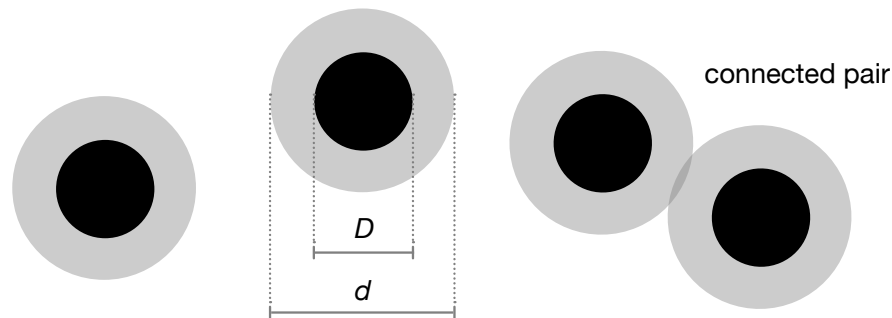


Figure 6.1: Schematic illustration of cherry pit model [94]. In this model, a particle is characterised by the particle diameter D (or impenetrable diameter) and the connectedness diameter d (or penetrable diameter).

After all the particles in the simulation box have been divided in clusters, we verify if there is at least one cluster that is connected to its periodic image. If that is the case, it percolates the simulation box. This may occur in one or more dimensions of the simulation box. For this reason, there are several ways to determine if percolation occurs. Here, we compare two different criteria. Firstly, percolation occurs if there is a cluster connecting to its periodic image in at least one dimension (criterion 1). Secondly, percolation occurs if there is a cluster connecting to its periodic image in *each* of the three dimensions (criterion 2). We calculate the percolation probability by taking the number of configurations that has a system-spanning cluster divided by the total number of configurations.

We obtain the percolation probability as a function of the dimensionless number density Nd^3/L^3 as defined in Reference [115] for different box sizes and values of the connectedness diameter d . Next we identify the percolation threshold as the crossing point of the percolation probability curves as a function of the number density for the two different box sizes we tested. Such a crossing point occurs for sufficiently large boxes, and is known to coincide with the percolation point in the thermodynamic limit [116]. This means that a formal (and time-consuming) finite-size analysis is not necessary [116].

At the percolation threshold, we analyse the distribution of sizes of the clusters for each combination of box size and ratio between the connectivity and particle diameters, D/d . We also record the time evolution of the average clus-

ter size. The time series of the average cluster size may present an underlying correlation. For this reason, we perform further analysis of the average cluster size, including the calculation of the temporal autocorrelation function of the average cluster size. We also present the scatterplot of the average cluster size c at time t , subtracted by the global averages of the cluster size \bar{c} versus the same quantity at time $t - 1$ unit in order to study the correlation in the cluster size in our simulation. We compute the time interval for which a pair of particles remains connected in a cluster.

6.3 Percolation threshold

We validate our procedure to find the percolation threshold (using dynamical simulations) for our somewhat soft repulsive spheres, by comparing our results the with recent results of Monte Carlo (MC) simulations by Miller for hard spheres based on 10^5 configurations [115]. In the MC simulations, the box sizes are $L_1 = 8d$ and $L_2 = 12d$, which are the sizes we choose for our simulation as well. In our simulations, we consider three values of the ratio $D/d = 0.8, 0.5,$ and 0.2 . As we keep the impenetrable diameter D constant, the penetrable diameters are then $d = 1.25D, 2D,$ and $5D$. Our simulation parameters are summarised in Table 6.1.

	LD simulations parameters					MC simulations	
	D/d	L_1/D	L_2/D	$N_c(L_1)$	$N_c(L_2)$	$N_c d^3/L^3$	
A	0.8	10	15	335	1130	0.65	0.64
B	0.5	16	24	315	1065	0.62	0.61
C	0.2	40	60	335	1130	0.65	0.65

Table 6.1: Simulation parameter and comparison with literature. Given are the ratio between the connectivity and particle diameters D/d , the two box sizes L_1 and L_2 in units of the sphere diameter D , the critical number of particles N_c for each box size and ratio D/d , and the critical number density $N_c d^3/L^3$ from our simulations and Reference [115].

In Figure 6.2, we present the percolation probabilities as a function of the scaled number density Nd^3/L^3 for two box sizes and three values of D/d . For each combination of these parameter, we calculate the percolation probability considering the two different percolation criteria described in Section 6.2. The top figures are related to the first criterion saying that percolation occurs if there is a cluster connecting to its periodic image in at least one dimension. The bottom figures are related to the second one, which only considers percolation to occur

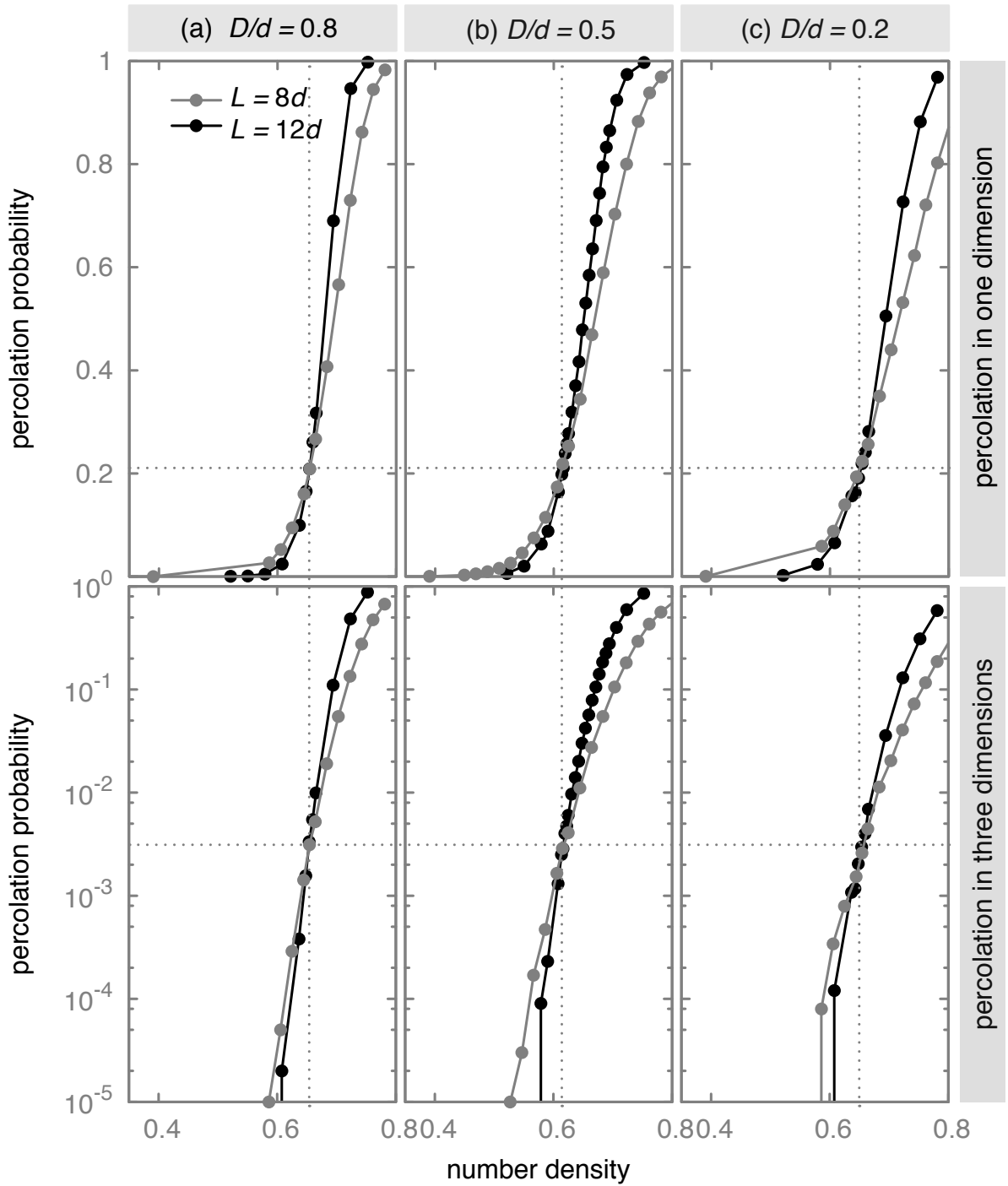


Figure 6.2: Percolation probability as a function of the scaled number density Nd^3/L^3 for both box sizes $L = 8$ (grey) and $12d$ (black) and ratios of (a) $D/d = 0.8$, (b) $D/d = 0.5$, and (c) $D/d = 0.2$. The dotted lines indicate the points at which the curves of the percolation probability for different box sizes cross. The vertical dotted line indicates the critical number density $N_c d^3/L^3$ for each ratio D/d and the horizontal dotted line indicates the percolation probability for each percolation criterion adopted.

if the clusters are connected in each of the three dimensions. In this case, the crossing of the percolation probability curves occurs at a very low concentration. For this reason, we present this figure in the log-linear scale such that the crossing point can be visualised.

In Figure 6.2, the dotted lines cross at the point where the curves of the percolation probability for different box sizes cross. The vertical dotted line indicates the critical number density for each ratio D/d , and the horizontal dotted line indicates the percolation threshold for each percolation criteria adopted. We find that criterion 1, the percolation in one dimension criterion, leads to a percolation probability of approximately 0.22 at the threshold in the thermodynamic limit, and that criterion 2, the percolation in all dimensions, to a much smaller percolation probability of approximately 0.3×10^{-2} at the threshold in that limit. These values are smaller than those found in previous work [116] and we have no explanation for it. However, the concentration at the crossing points that we identify as the percolation threshold agree well with the Miller data [115] that we also quote in the last column of Table 6.1. For example, from the MC simulations for the ratio $D/d = 0.5$, the number of particles in the simulation box at the percolation threshold corresponds to $N_c = 312$ and 1054 particles, if the the box size is respectively $L = 8d$ and $12d$. In comparison, our simulations for $d = 2D$, so that we have the same case of $D/d = 0.5$, $L = 24D = 12d$ (for soft spheres) give very similar values of $N_c = 315$ and 1065. These values agree within about one percent. The fact that the percolation threshold for our two criteria are internally consistent, and that our percolation thresholds agree with those of Miller [115], support our conclusion that our simulation procedure is reliable.

6.4 Cluster dynamics

Next, we discuss the cluster statics and dynamics for the two box sizes and three values of the ratio D/d , at what we infer must be the percolation threshold in the thermodynamic limit, see Table 6.1. We analyse several features of the dynamics of the spheres near the percolation threshold, the first of which is the distribution of cluster sizes. In Figure 6.3, we present the distributions of the cluster sizes for both box sizes $L = 8d$ and $12d$ and ratios of (a) $D/d = 0.8$, (b) $D/d = 0.5$, and (c) $D/d = 0.2$ in log-linear and log-log scales. From the figures on the left (log-linear), we find that larger clusters form for smaller values of the ratio of the impenetrable and penetrable diameters of the spheres, D/d . This is expected as, for these ratios, the simulation boxes are proportionally larger (in units of the particle diameter D). The difference between the distribution becomes clearer if we compare the ratios $D/d = 0.8$ and 0.2 as, for these ratios, there is the same

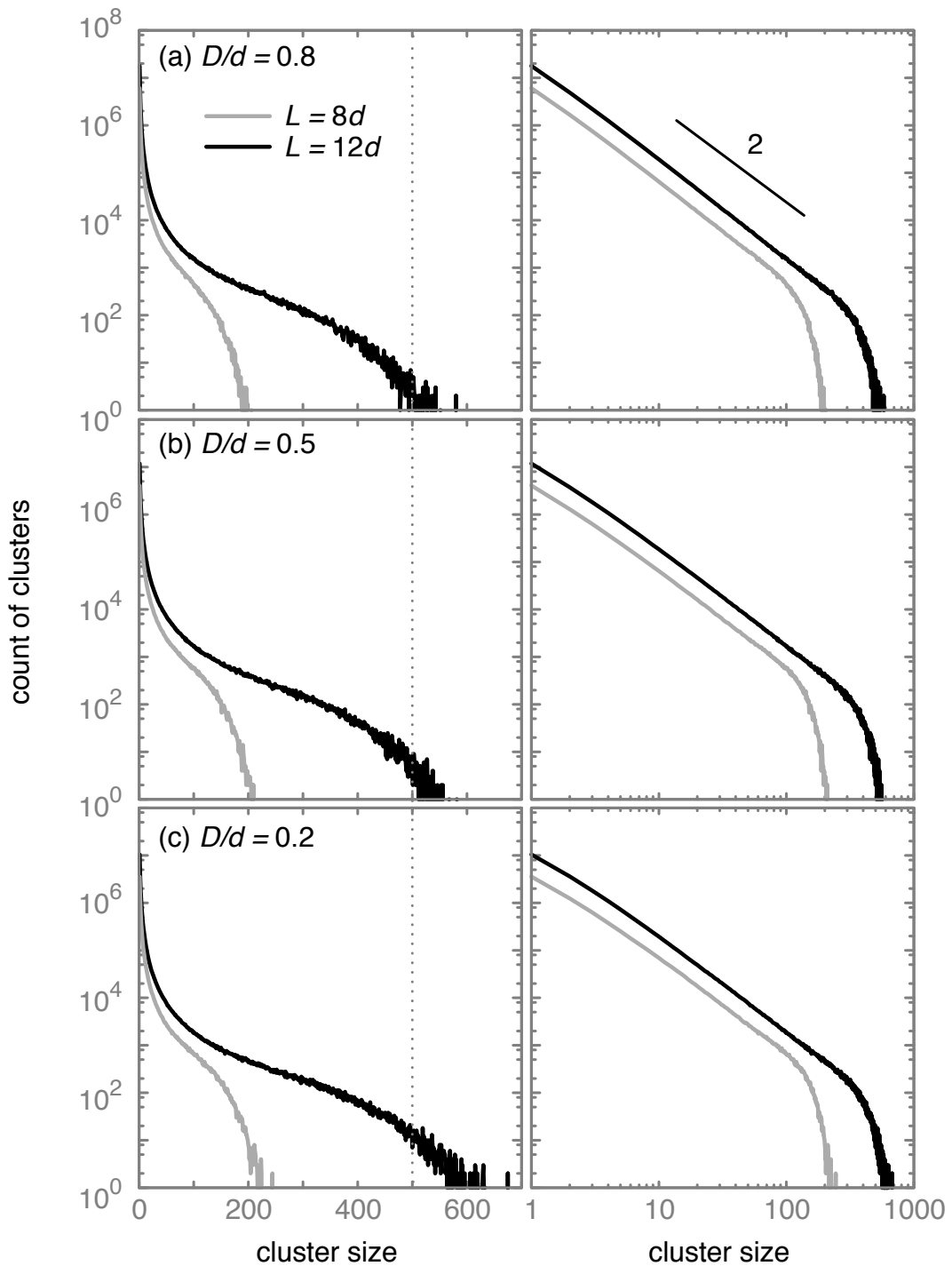


Figure 6.3: Distribution of the cluster size for both box sizes $L = 8d$ and $12d$ and ratios of (a) $D/d = 0.8$, (b) $D/d = 0.5$, and (c) $D/d = 0.2$ in a log-linear scale (left) and a log-log scale (right). Particle numbers are fixed to correspond conditions at the percolation threshold in the thermodynamic limit. See Table 6.1.

number of particles N_c in each size of the simulation box, a particle number that we identified as the critical number corresponding to percolation in the thermodynamic limit. For the ratio $D/d = 0.2$, we find a considerably larger tail (a larger number of clusters contains more than 500 particles, as indicated by the dotted line). In the figures on the right (log-log), we find that the distributions follow a power law with exponent -2 for all box sizes and ratios D/d . A power law of -2.1 is found in the off-lattice simulation of sticky particles close to the percolation threshold [117]. For concentrations below the percolation threshold, in the flocculation regime, the cluster size distribution follows a power law of 1.5 in the same system. Actually, the power law of approximately 2 is also found in lattice-based simulations in 2 and 3 dimensions [118]. This indicates that lattice and off-lattice percolation belong to the same universality class. The algebraic distribution seems to cross over to an exponential one beyond some large cluster size, which is expected theoretically [114].

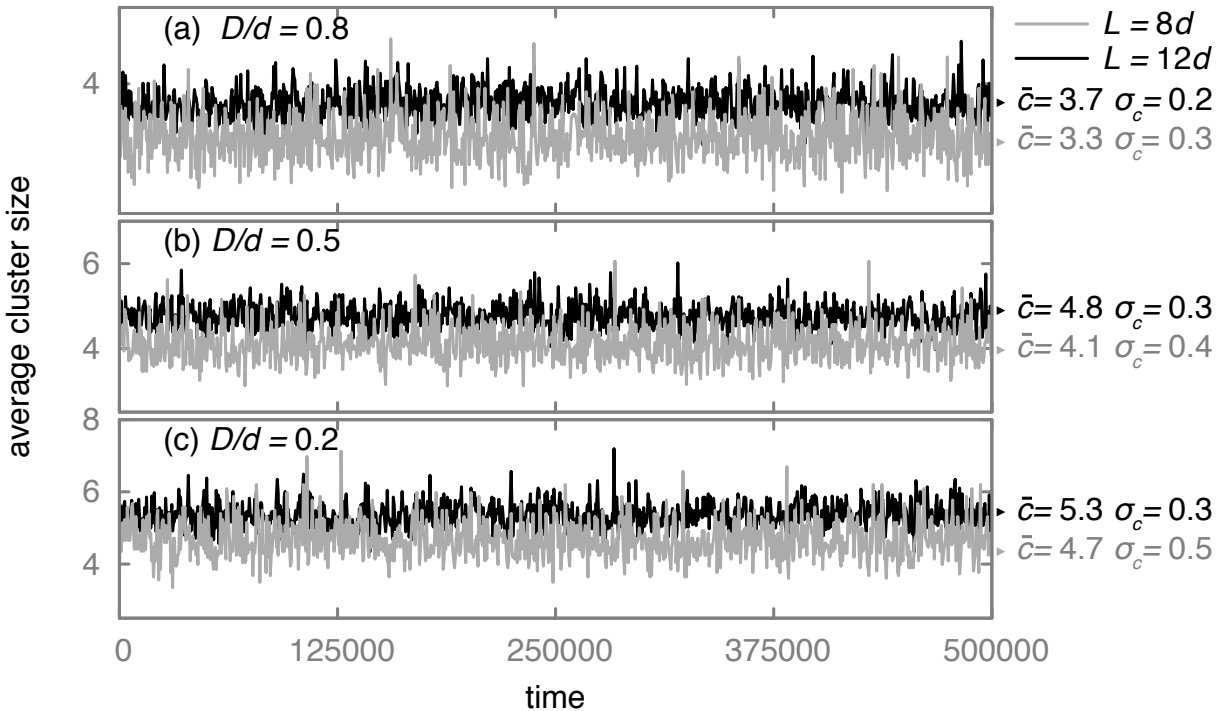


Figure 6.4: Time evolution of the average cluster size for both box sizes $L = 8d$ (grey) and $12d$ (black) and ratios of (a) $D/d = 0.8$, (b) $D/d = 0.5$, and (c) $D/d = 0.2$. The data points are presented every 500 time units for better visualisation. As mentioned previously, we probe 5 times more points as the sampling time is every 100 time units. The time unit is $D\sqrt{m/k_B T}$. We indicate the global averages of the cluster size \bar{c} and standard deviation σ_c for the data presented.

Having established the mean size distribution, we now turn to temporal fluctuations in this distribution, focusing on a single moment of this distribution. In

Figure 6.4 we present the average cluster size as a function of the simulation time for the box sizes $L = 8d$ (grey) and $12d$ (black) and core-shell ratios of (a) $D/d = 0.8$, (b) $D/d = 0.5$, and (c) $D/d = 0.2$. Data points are presented every 500 time units. We also indicate the global averages of the cluster size \bar{c} and standard deviation σ_c of the data presented. The averages shown are not for a percolating cluster as this should have at least around 10 particles in order to cover the distance of one box dimension. As expected, we find in Figure 6.4 that the average cluster size increases with decreasing values of the ratio D/d . By eye, the time-dependent mean cluster size of Figure 6.4 seems to be dominated by two time scales: a short *noisy* time scale and a longer time scale. Naively one expects the short time scale to be related to the attachment to and detachment of single particles from a cluster, and a long time scale related to similar processes on a larger length scale, involving entire subclusters. To verify this we analyse the frequency spectrum by performing a Fast Fourier Transform of the time evolution of the average cluster size (results not shown). We cannot identify characteristic frequencies in this spectrum, probably due to the noise in the data. Hence, we calculate the autocorrelation of the average cluster size. In Figure 6.5, we present the autocorrelation for both box sizes $L = 8d$ and $12d$ and ratio of the impenetrable and penetrable diameters of the spheres of (a) $D/d = 0.8$, (b) $D/d = 0.5$, and (c) $D/d = 0.2$. The figure clearly shows that the correlation time decreases with increasing value of D/d . This is expected as the clusters are more “dense”: there is more overlap between the particles due to the larger penetrable diameter. Actually, a closer inspection of the decay of the cluster size autocorrelation function shows that it is not a simple single exponential decay. The short-time decay seems to be algebraic whilst the long-time decay seems exponential. We can quantify the long-time decay by measuring the relaxation time associated with the exponential decay regime. This produces decay times of approximately 439, 253, and 18 time units for $D/d = 0.2, 0.5$ and 0.8 . Interestingly, as can be inferred from Figure 6.5, these values seem to depend quite strongly on the ratio D/d and much less so on the simulation box size.

That there are temporal correlations in the instantaneous cluster size can also be seen in the scatterplot of the average cluster size c at time t subtracted by the global averages of the cluster size \bar{c} versus the same quantity at time $t - 1$. In Figure 6.6, we find that for the ratio $D/d = 0.8$ the time evolution of the cluster size is less correlated over one time unit but the correlation increases as we decrease the ratio D/d . This agrees with what we find previously from the autocorrelation function in Figure 6.5. Unlike our findings by considering the autocorrelation function, the scatterplot does indicate that there are differences between the box sizes for each value of the ratio D/d . These, presumably, are related to the larger (relative) fluctuations in the average cluster size for the smaller box sizes.

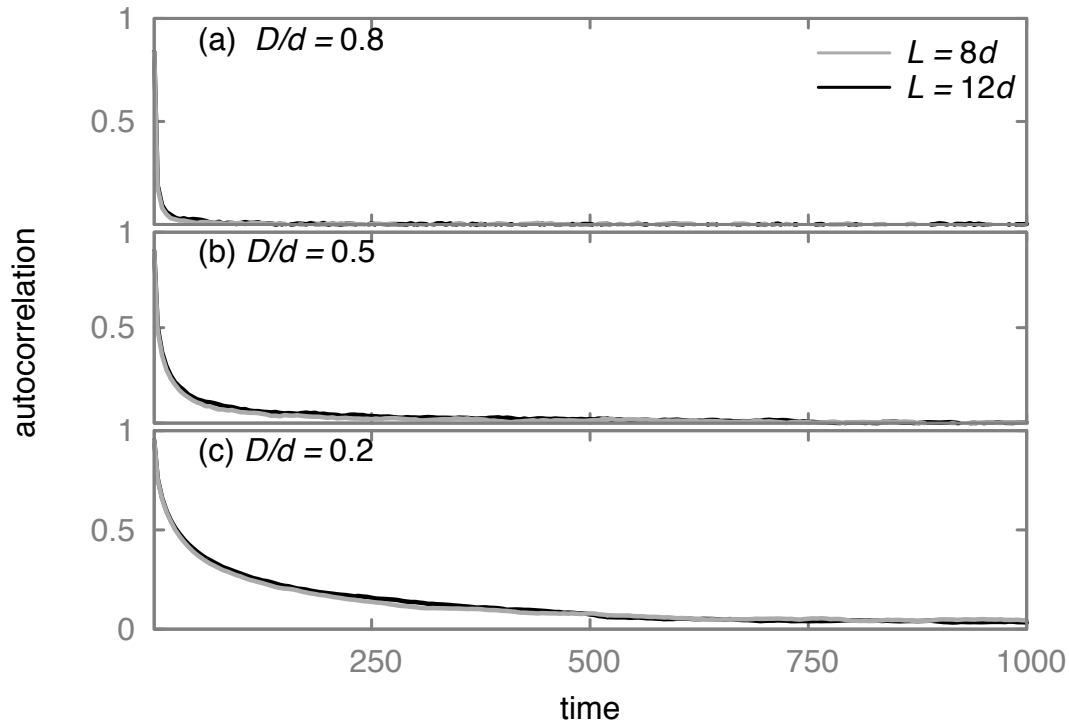


Figure 6.5: Autocorrelation of the average cluster size as a function of time for both box sizes $L = 8d$ and $12d$ and ratio of the impenetrable and penetrable diameters of the spheres of (a) $D/d = 0.8$, (b) $D/d = 0.5$, and (c) $D/d = 0.2$. The time is in units of $D\sqrt{m/k_B T}$.

We obtain better statistics if we measure the survival time of pairs of particle in the same cluster, that is, if we focus on particles that are directly or indirectly connected during the simulation run, and we measure the time that they remain connected. In Figure 6.7, we present the distribution of the lifetime τ for both box sizes $L = 8d$ and $12d$, and connectivity ratios (a) $D/d = 0.8$, (b) $D/d = 0.5$, and (c) $D/d = 0.2$. The counts of number of pairs connected seem to decay biexponentially with different characteristic times τ_c for short and long times. The values for the short and long characteristic times that we find are collected in Figure 6.8. It shows that the latter depends strongly on the ratio D/d , whereas the former does not. We note that for the short lifetime it is not clear whether the decay is actually exponential, as it could also be algebraic on account of the low resolution in this interval, we fit an exponential to obtain the appropriate time scale. The values of both characteristic times seem to not depend on the box size, supporting earlier finding focusing on the cluster size autocorrelation function. This suggests that increasing the system size does not lead to a diverging time scale, and hence we surmise that there is no equivalent of the expected critical slowing down near the percolation transition.

To investigate this in more detail, we performed our simulations and analysis

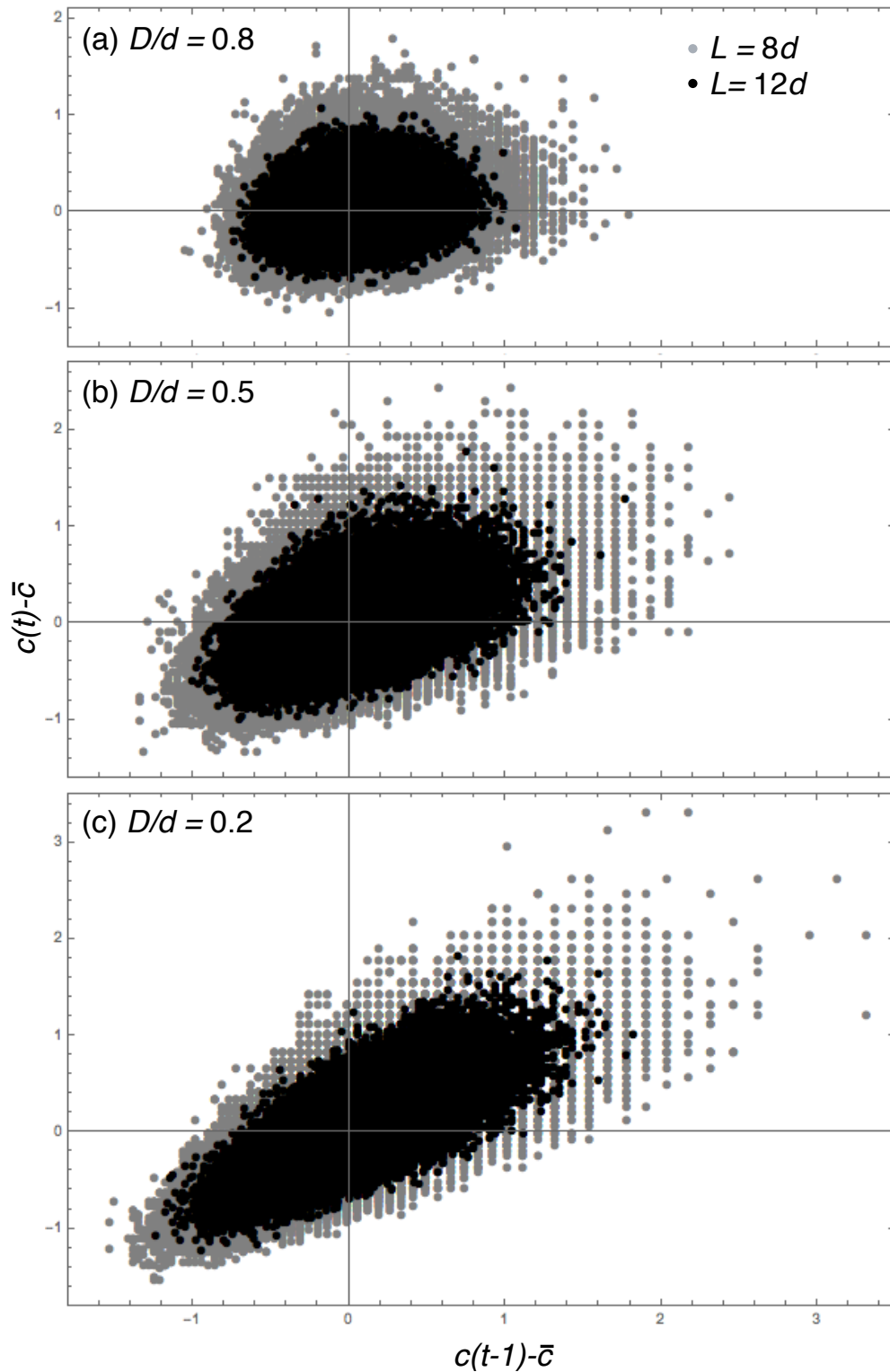


Figure 6.6: Scatterplot of the average cluster size c at time t subtracted by the global averages of the cluster size \bar{c} versus the lag-1 time unit. This is for both box sizes $L = 8d$ and $12d$ and ratio of the impenetrable and penetrable diameters of the spheres of (a) $D/d = 0.8$, (b) $D/d = 0.5$, and (c) $D/d = 0.2$.

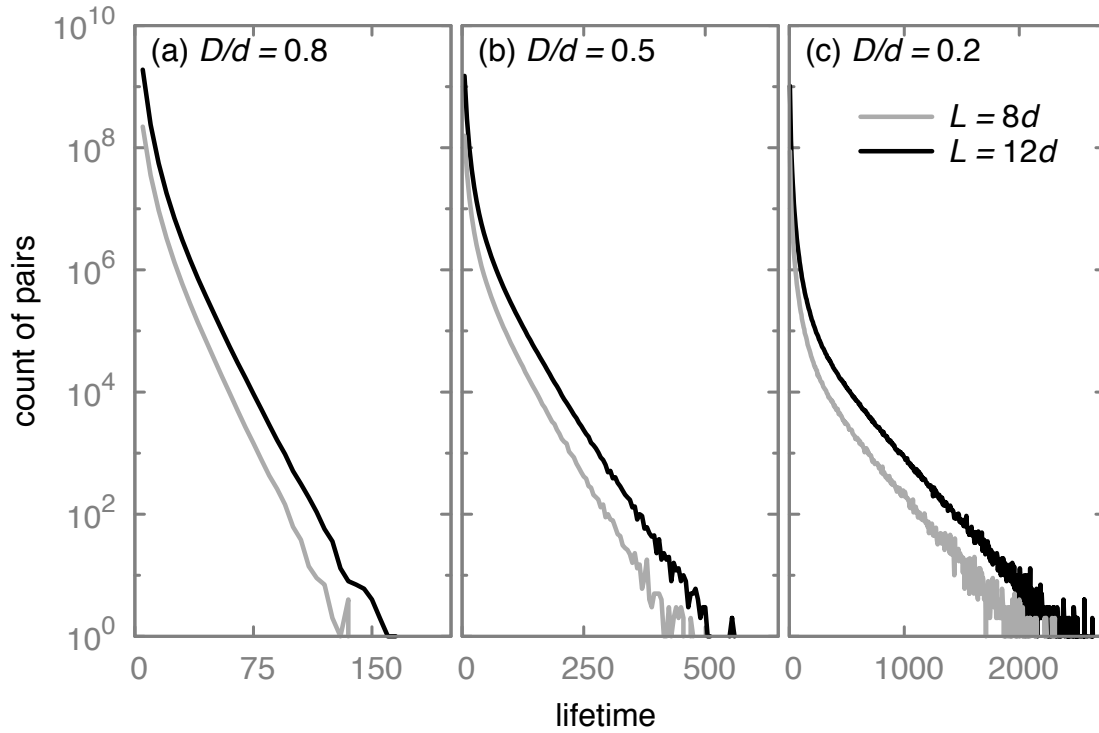


Figure 6.7: Distribution of the lifetime that a pair of particles remain connected (directly or indirectly) for both box sizes $L = 8$ and $12d$ and ratios of (a) $D/d = 0.8$, (b) $D/d = 0.5$, and (c) $D/d = 0.2$. Data points are presented every 5 time units. The time unit is $D\sqrt{m/k_B T}$.

also for a larger box size of $L = 16d$ for the connectivity ratio $D/d = 0.5$. For this additional box size, the percolation probability as a function of the scaled number density Nd^3/L^3 crosses the percolation probabilities of the box sizes $L = 8d$ and $L = 12d$ at their crossing point for both percolation criteria adopted within 1% error. We find that the critical number of particles N_c for this larger box is $N_c = 2510$. This gives the number density $N_c d^3/L^3$ of 0.61, in agreement with the MC simulations in Reference [115]. Therefore, this result (not shown) confirms what we find for the smaller box sizes.

In addition, we investigate the time evolution of the average cluster for this box size at the percolation threshold as well as for values of the connectedness diameter d slightly below and above $d = 2D$, but keeping their respective values of the critical number of particles N_c for $d = 2D$ constant. In other words, we compare the time evolution of the average cluster at the percolation with simulation conditions slightly below and above percolation. The average cluster size increases with increasing connectedness diameter, as expected. Results not shown. The same procedure is applied for the distribution of both the cluster size and the lifetime that a pair of particles remain connected. In Figure 6.9, we show that the distribution of the cluster size also follow a power law with expo-

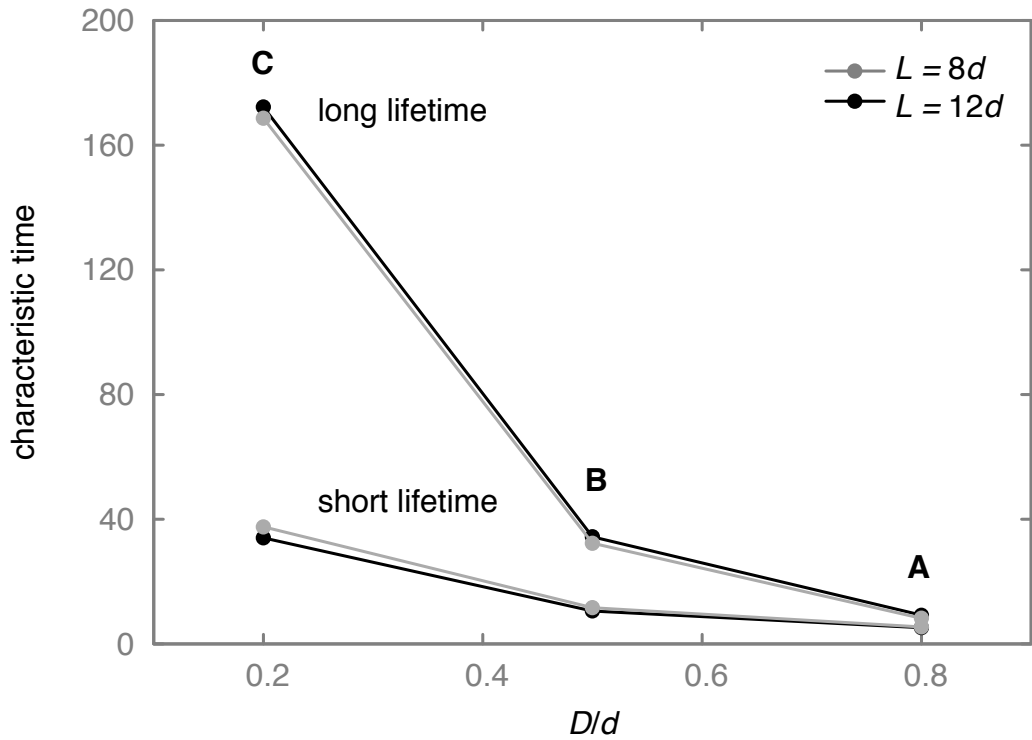


Figure 6.8: Short and long characteristic lifetimes τ_c as a function of the ratio D/d for both box sizes $L = 8d$ (grey) and $12d$ (black). The time unit is $D\sqrt{m/k_B T}$.

ment -2 for all critical and off-critical values of the connectedness diameter $d = 1.90, 1.95, 2.00, 2.05,$ and $2.10 D$ for box sizes $L = 24 D$ (a) and $L = 32 D$ (b), which correspond to the box sizes $L = 12 d$ and $16 d$ if $d = 2 D$. The major difference between these distributions of the cluster size is the tail, as the number of large clusters increases with increasing d . There is, nevertheless, a limitation in size for the clusters (that is the total number of particles in the box). For this reason, we find a deviation in the decay of the cluster distribution for the connectedness diameter $d = 2.05,$ and $2.10 D$ for both box sizes. As expected, for the distribution of the lifetime that a pair of particles remain connected, we find that both the short and long characteristic lifetime increase with increasing connectedness diameter. Results not shown.

6.5 Discussion and conclusions

We perform Langevin dynamics computer simulations in order to investigate the statics and dynamics of clustering in suspensions of mutually repulsive spherical particles. The clustering we investigate is purely geometric and determined by a maximum distance between the particles' centres of mass. The percolation threshold is defined as the critical concentration beyond which there is at least

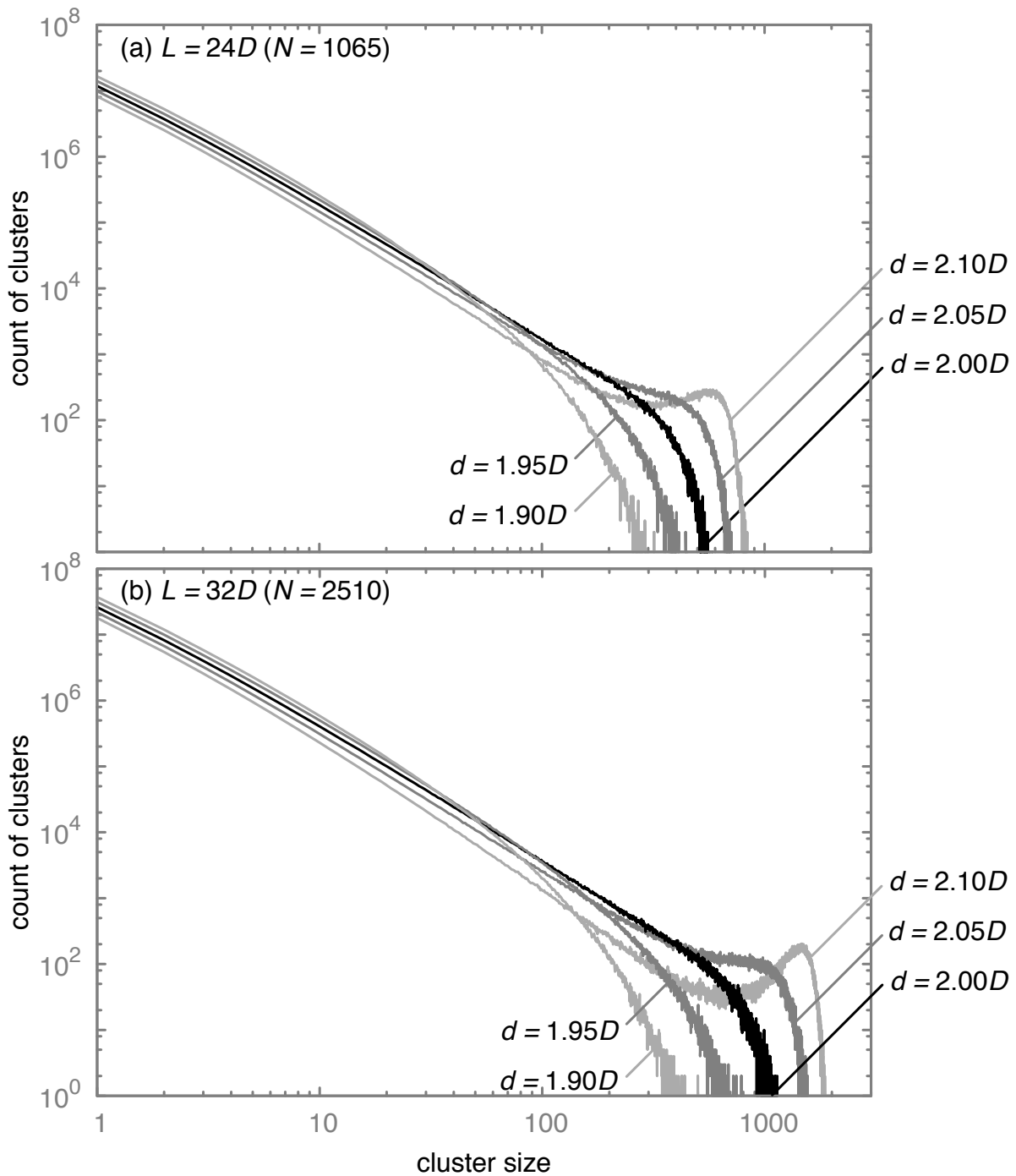


Figure 6.9: Distribution of the cluster size for both box sizes for box sizes $L = 24D$ (a) and $L = 32D$ (b), which correspond to the box sizes $L = 12d$ and $16d$ if $d = 2D$ on a double-logarithmic scale. The distribution of the cluster size follows a power law with exponent -2 for all values of the connectedness diameter d investigated, critical and off-critical.

one system-spanning network in the dispersion.

While the statics of geometric percolation is reasonably well understood, this is not the case for the dynamics associated with this phenomenon. If percolation is akin to a second order phase transition, as it is often put forward [114], then naively this might imply that the dynamics should exhibit critical slowing down. This would, for instance, imply that clustering becomes infinitely slow at the transition. If so, then the percolation threshold would be impossible to pinpoint accurately. The problem thus merits some attention.

In our simulations, we evaluate the percolation probability for various concentrations of particle, connectivity ranges, and simulation box sizes. We pinpoint the macroscopic percolation threshold by evaluating at what density the percolation probabilities cross for different system sizes. The percolation thresholds that we find agree with values of recent Monte Carlo simulations [115]. The statics and dynamics of the clustering we evaluate for densities at the percolation threshold.

We find for finite-size simulations at the concentration corresponding to the macroscopic percolation threshold that the cluster size distribution is algebraic, crossing over to what seems an exponential distribution. We find that this is independent of the connectivity range and the box size, at least for the box sizes that we tested. The exponential tail we expect because of our finite system size, implying that there is no actual percolation threshold in our simulations.

The mean cluster size that we find varies with time. This is not surprising because particles, depending on their instantaneous time-dependent location, continuously “attach to” and “detach from” the clusters and spend time as not connected to any cluster. The temporal fluctuations of the average cluster size must contain information on these processes. If we investigate the existence of dominating time scales by means of evaluating the autocorrelation function, we find evidence for two regression times. However, because of poor statistics, we are not able to quantitatively evaluate the prevalent times.

Hence, we resort to evaluating the survival time of pairs of particle in the same cluster. This quantity turns out to present good statistics, confirming that there are indeed two underlying time scales that define the physics of the problem in hand. These two time scales turn out to depend on the connectivity range. The shorter time scale depends only weakly on that, whilst the longer time scale is very sensitive to the connectivity range. We speculate that the first involves local attachment and detachment events, and the second global ones involving whole clusters.

The two time scales that we find are relatively insensitive to the simulation box size, even though the average cluster size does vary with box size albeit modestly so. The longer time scale we expect to be the candidate that might exhibit

critical slowing down, implying that if that were the case it should become slower with increasing system size. It does do that but only very weakly so. From our simulations, we cannot confirm that it is indeed a diverging time scale at the percolation threshold. Of course, our simulations are restricted to very small box sizes, so we cannot exclude this possibility either. Clearly, more study is needed to settle this issue.

6.A Estimate of the cluster renewal time

To estimate the renewal time of a cluster, we make use of the idea that all particles that make up a cluster must be replaced by particles coming from further away than the volume spanned by the cluster. We presume that there is a steady state influx of particles from outside of the cluster that obeys the diffusion equation, $\partial\rho/\partial t = \mathcal{D}\nabla^2\rho$, where ρ is the number density of particles, \mathcal{D} is their (collective) diffusion coefficient, and ∇^2 the Laplacian operator. As we are interested in steady-state renewal of clusters, we ignore any time dependence and put $\nabla^2\rho = 0$.

Presuming the cluster is more or less spherical in shape, and making use of spherical coordinates, we find for the solution of the Laplace equation $\rho = \rho(r) = a + (b/r)$, with $r \geq R$ the radial distance from the centre of the cluster of radius R . Note that a and b are constants to be fixed by the boundary conditions. We plausibly presume that at infinity, so for $r \rightarrow \infty$, we have the bulk density $\rho(r \rightarrow \infty) \equiv \rho_\infty$, implying that $a = \rho_\infty$. We surmise that upon entering the cluster via its boundary at $r = R$, a particle immediately becomes part of the cluster and hence no longer counts as a bulk particle. Hence, we impose an absorbing boundary condition: $\rho(R) = 0$. This in turn implies that $b = -\rho_\infty R$, and $\rho(r \geq R) = \rho_\infty(1 - r/R)$.

To answer the question how much time it takes to completely renew the particles in a cluster, we evaluate the flux $J_r(R)$ across the surface of the envelope towards the cluster: $J_r(R) = \lim_{r \rightarrow R} \mathcal{D} \partial_r \rho(r) = \mathcal{D} \rho_\infty / R$. Let N be the number of bulk particles that have entered the cluster. The rate at which particles enter the volume of the cluster obeys $\partial N / \partial t = 4\pi R^2 J_r(R) = 4\pi R \mathcal{D} \rho_\infty$. This means it takes $\tau = N / 4\pi R \mathcal{D} \rho_\infty$ seconds to get N particles across the surface of the cluster. Now, the total number of particles n in an average cluster of size R obeys, within mean-field continuum percolation theory [105], $R \sim D n^{1/2}$. Since we need to renew all particles, we must have $n = N$. In other words, the renewal time must be equal to $\tau = N^{1/2} / 4\pi D \rho_\infty$.

For volume fractions $\phi = \pi \rho_\infty D^3 / 6$ just below the percolation threshold, ϕ_c , we have, again within mean-field theory [114] and in the thermodynamic limit,

$N \sim (\phi_c - \phi)^{-1}$. Hence, the renewal time scales as $\tau \sim (\phi_c - \phi)^{-1/2}$ and should therefore diverge at the percolation threshold. Obviously, this somewhat naïve analysis remains contentious, not least as it presumes that all bulk particles that enter the cluster become part of the cluster on time scales small compared to the diffusion time to the cluster. Also, we ignore replacement of newly absorbed particles by even more recently absorbed particles.

Acknowledgments

We thank Shari Finner for useful discussions and Thijs van der Heijden for his help proofreading this chapter.

Chapter 7

Conclusion

In this chapter we return to the original research questions presented in the Introduction. We summarise our main results and conclusions of each chapter. Finally, we reflect on the limitations and the possible developments of the research presented in this thesis and give suggestions for further research.

7.1 Aim of the thesis

Since the introduction of filamentous viruses as model systems of hard rods, we have learned a lot about their self-organisation and dynamics in suspensions. Interesting behaviours are experimentally observed as particle properties such as the particle anisotropy, bending flexibility and “localised” interactions are changed. The contribution of this thesis is to closely investigate some of these behaviours by means of computer simulations. Simulations allow for a better control over some of the variables for testing the relationship between the particle properties and the structure of the various phases that these particles may support, as well as their self-diffusion in these phases. Additionally, in our particle-based simulations we are able to analyse their configurations and relate these with the stability of the phases found.

In most chapters, we support our simulations by simple theoretical models and compare our results with experiments on filamentous viruses. The differences in aspect ratio and interactions between these model particles prevents us to make a quantitative comparison. Nevertheless, we are able to qualitatively compare results and usually good agreement between them is found. Our final goal is to understand the physical principles that are relevant for understanding the structure and dynamics of the suspension of filamentous viruses in the wider context of elongated colloidal particles. Our research questions are recapitulated in the next section. They are followed by our response to them in the light of our main conclusions that are also summarised there. Finally, we give suggestions for further research based on the limitations of our work.

7.2 Summary and conclusions

In this thesis we address four research questions. In Chapter 3, the question we focus on is *how do aspect ratio and flexibility change the stability and structure of the liquid-crystalline phases?* We find that our semi-flexible rods form five distinct phases, namely, in order of increasing particle concentration, isotropic, nematic, smectic A, smectic B, and crystalline phases. In general, on one hand, the phase transitions are shifted to lower particle concentrations as the aspect ratio increases due to the increase in the excluded volume interaction. On the other hand, they usually shift to higher concentrations as the flexibility increases due to the increase of particle entropy. In agreement with previous works, we find that the isotropic-nematic and nematic-smectic A phase transitions are particularly responsive to changes in the aspect ratio and the flexibility of the particles.

In addition, we examine the particle behaviour within the phases in order to

better understand the relationship between the phase stability and the particles flexibility. We find that the end-to-end distance of the particles increasingly approaches their contour length with increasing concentration, which reduces their bending fluctuations. Within our model description, these bending fluctuations are essentially suppressed in smectic B and crystalline phases, explaining the insensitivity of these phases to the changes in persistence length of our particles. Interestingly, we find that the interlayer spacing in the layered phases do not always decrease with increasing concentration of particles. At least in the smectic A phase, depending on aspect ratio and flexibility, the spacing may increase. This is possible provided that the increasing concentration is compensated for by a more than proportional in-layer concentration increase. For the increase in layer spacing going from the smectic A to the smectic B phase, we provide another explanation. This, we believe, is caused by the increase in free volume across the transition.

In Chapter 4, our research question is *what is the effect of a weakly attractive tip on the phase behaviour of elongated colloidal particles?* Our work surprisingly shows that the phase behaviour as well as the structure of the various phases are strongly affected by relatively weak interaction strengths, of the order of the thermal energy. The main effects of the attractive tips on the phase behaviour are the formation of bi-layered anti-ferroelectric phases and a large increase of stability of smectic A at the expense of the nematic phase, and even at the expense of the isotropic phase as we increase the attraction strength between the tips. We discuss that the key factor is the interplay between the interaction energy, polarity of the particles, and the phase microstructure. Here, we also analyse the behaviour of particles within the various phases. We find that the stability of the isotropic and nematic phases is affected by the aggregation of the tips, only if the particles align in response to the local increase in concentration. In the layered phases, the organisation of the particles with the attractive tips results in more strongly ordered microstructures even at very weak attraction energies.

Supported by experimental evidence, we find a shift of the nematic-to-smectic A phase transition to lower volume fractions, which also seems to become more strongly first order with an increase of the attraction strength. We also compare the smectic ordering potential from experiments and simulations. We find for both of them larger values of the height and smaller values of the width as the attraction strength between tips increases. As expected, because the experimental model particles are larger in aspect ratio, their smectic potential height is also larger, increasing the stability of the smectic A phase with increasing aspect ratio. Our study contributes to the understanding of how selective surface functionalisation of colloidal liquid crystals affects their self-organisation by providing a systematic study of the stability and structure of these phases for a wide range

of both volume fractions and attraction strengths. We show that incorporating a single (enthalpic) functionalised end in elongated colloidal particles gives rise to an even more complex and rich phase behaviour than for the purely repulsive ones.

In Chapter 5, we address the question of *how do the anisotropy and the flexibility of elongated particles affect their diffusion in a lamellar background phase?* We show that the in-layer rattling and the diffusion through smectic layers of the guest particle is mostly determined by the ratio between the contour length of the guest and host particles and not so much by the persistence length of the guest particle. This is unexpected as it is reasonable to assume that bending fluctuations of the particle help cage escape, in particular between layers. Nevertheless, it is also possible that there is a suppression of bending modes by the molecular ordering of the host phase that is the root cause of our finding that bending flexibility does not strongly affect diffusion parallel and perpendicular to the director. The in-layer diffusion does not seem to be affected by either the ratio between the contour length of guest and host particles or the guest particle persistence length.

In agreement with experiments, both shorter and longer guest particles of incommensurate contour length in relation to the host particles diffuse faster along the director, in other words, through the smectic layers. As suggested earlier [41], the advantage that a longer guest particle seems to have is the partial penetration into the neighbouring layers, creating the space needed to diffuse along the director. That is not the case for the shorter guests. The advantage that these particles have probably is the larger amplitude of their in-layer rattling in comparison to the other guest particles. Interestingly, it is the shortest and the largest guest particles that we tested that are *more widely spread* around the centre of the smectic layer.

The question of *how long does it take clusters to substitute all particles that initially form it?* is the motivation for the study presented in Chapter 6. This question is not directly addressed. Instead, we evaluate the lifetime that a pair of particles remain connected. The long lifetimes are an indication of the renewal time we are interested in. The distribution of the lifetime that a pair of particles remain connected seems to decay exponentially with two different exponents that, similarly to the critical concentration, do not depend on the simulation box size but do depend on the ratio of the sphere diameter and the connectedness diameter. We associate each of the exponents found to a short and a long time scale. This short time scale we speculate is related to the attachment to and detachment from the cluster of single particles, and the long time scale could be related to similar processes on a larger length scale, involving entire subclusters. Unlike our initial expectation, we do not find a diverging time scale.

In addition, we analyse the cluster size distribution at the percolation threshold. The distribution of cluster sizes seems to decay following a power law with exponent -2 which does not depend on both the box size and the ratio of the sphere diameter to the connectedness diameter. This power law is also found in concentrations below and above the critical concentration. An explanation remains elusive.

7.3 Outlook

Based on our findings, we suggest here some points for further research. In Chapter 3, we indicate that the phase sequences of our semi-flexible particles does not include the columnar phase probably due to their short aspect ratio. A natural but still ambitious next step is to simulate longer semi-flexible rods. Their aspect ratio should be larger than 30 to find this phase, as indicated by experiments [28]. The short aspect ratio of the particles is also an issue for the comparison between experiments and simulations in the next two chapters. The unexpected increase in the interlayer spacing with increasing concentration of particles in the smectic A phases is also another point for further investigation. We have not been able to pinpoint under what conditions this happens and also do not have an explanation for this phenomenon.

In Chapter 4, we present a simple theoretical model for perfectly parallel hard rods with an attractive end based on the Maier-Saupe-McMillan theory. The model presents a fairly good agreement with the simulations but it could be expanded so that it describes the nematic-to-smectic A and the smectic ordering potential more closely to what is found in our simulations. In our model, despite the fact that it does predict a shift to lower volume fractions for the nematic-to-smectic A_2 phase transition, the shift of the nematic-to-smectic A phase transition is independent of the volume fraction. This is not the case in our simulations. (From the experiments, we cannot tell if there is an anti-ferroelectric phase transition in the smectic A phase, but also in this case the nematic phase is destabilised.) In addition, the height and width of the effective smectic ordering potential from our theory does not emulate the smectic ordering potential from our simulations. A possible approach could be representing it as a Gaussian function instead of a cosine function.

In Chapter 5, the overall small effect flexibility has on the several aspects of the diffusion of guest particles in a smectic background could be due to the resolution of our model particles. It is interesting to perform simulations employing model particles that have better resolution for the matter of testing the effect of flexibility in the self-diffusion. As we show, flexibility has a large effect in the

phase behaviour and particle configurations. For this reason, it could well be that the particle persistence length has an effect on the caging time, which impacts on the hopping diffusion.

In Chapter 6, we investigate dynamical percolation of not quite hard spheres. Unlike the simulations of elongated particles, whose dynamic properties are investigated in highly congested phases, we study particles in isotropic solution at quite low packing fraction. For this reason, hydrodynamic interactions could be relevant in this work, not included in our simulations. Because we focus on the data analysis in this chapter, the simulations including hydrodynamic effects are relegated for future developments of this study. The percolation probability that we find is of approximately 0.2 at the percolation threshold. It means that about 1/5 of the configurations contain a (wrapping) system spanning cluster. It may well be that considering only the configurations containing the percolating clusters rather than all clusters reveals features that are not picked up in the type of analysis we perform.

Bibliography

- [1] Kuijk, A., Byelov, D. V., Petukhov, A. V., van Blaaderen, A., and Imhof, A., *Faraday Discussions* **159** (2012) 181.
- [2] Meyer, R. B., Ordered phases in colloidal suspensions of tobacco mosaic virus, in *Dynamics and Patterns in Complex Fluids*, Springer, 1990.
- [3] Furukawa, R., Kundra, R., and Fechheimer, M., *Biochemistry* **32** (1993) 12346.
- [4] Lagerwall, J. P. and Scalia, G., *Current Applied Physics* **12** (2012) 1387 .
- [5] Kim, H. J., Jung, W.-B., Jeong, H. S., and Jung, H.-T., *Journal of Materials Chemistry C* **5** (2017) 12241.
- [6] Liu, Z., Xu, Z., Hu, X., and Gao, C., *Macromolecules* **46** (2013) 6931.
- [7] Nam, K. T. et al., *Science* **312** (2006) 885.
- [8] Tseng, R. J. et al., *Nature Nanotechnology* **1** (2006) 72.
- [9] Steinmetz, N. F. et al., *Advanced Functional Materials* **18** (2008) 3478.
- [10] Lee, Y. J. et al., *Science* **324** (2009) 1051.
- [11] Chaudhary, K., Chen, Q., Juarez, J. J., Granick, S., and Lewis, J. A., *Journal of the American Chemical Society* **134** (2012) 12901.
- [12] de la Cotte, A., Wu, C., Trevisan, M., Repula, A., and Grelet, E., *ACS Nano* **11** (2017) 10616.
- [13] Park, S., Lim, J.-H., Chung, S.-W., and Mirkin, C. A., *Science* **303** (2004) 348.
- [14] Arora, A. K. and Rajagopalan, R., *Current Opinion in Colloid & Interface Science* **2** (1997) 391 .
- [15] Dhont, J. K., *An Introduction to Dynamics of Colloids*, volume 2 of *Studies in Interface Science*, Elsevier, 1996.

- [16] Reichl, L., *A Modern Course in Statistical Physics*, Physics textbook, Wiley, 2009.
- [17] Barrat, J.-L. and Hansen, J.-P., *Basic Concepts for Simple and Complex Liquids*, Cambridge University Press, 2003.
- [18] Barón, M., *Pure and Applied Chemistry* **73** (2001) 845.
- [19] Onsager, L., *Annals of the New York Academy of Sciences* **51** (1949) 627.
- [20] Odijk, T., *Polymer Communications* **26** (1985) 197.
- [21] Odijk, T., *Macromolecules* **19** (1986) 2313.
- [22] Chen, Z. Y., *Macromolecules* **26** (1993) 3419.
- [23] Hidalgo, R. C., Sullivan, D. E., and Chen, J. Z. Y., *Physical Review E* **71** (2005) 041804.
- [24] Shundyak, K., van Roij, R., and van der Schoot, P., *Physical Review E* **74** (2006) 021710.
- [25] Bolhuis, P. and Frenkel, D., *The Journal of Chemical Physics* **106** (1997) 666.
- [26] Grelet, E., *Physical Review Letters* **100** (2008) 168301.
- [27] Grelet, E., *Physical Review X* **4** (2014) 021053.
- [28] Grelet, E. and Rana, R., *Soft Matter* **12** (2016) 4621.
- [29] Dogic, Z. and Fraden, S., *Philosophical Transactions of the Royal Society A* **1782** (2001) 997.
- [30] Barry, E., Beller, D., and Dogic, Z., *Soft Matter* **5** (2009) 2563.
- [31] van der Schoot, P., *Journal de Physique II* **6** (1996) 1557.
- [32] Dogic, Z. and Fraden, S., *Physical Review Letters* **78** (1996) 2417.
- [33] Grelet, E., Lettinga, M. P., Bier, M., van Roij, R., and van der Schoot, P., *Journal of Physics: Condensed Matter* **20** (2008) 494213.
- [34] Dijkstra, M. and Frenkel, D., *Physical Review E* **51** (1995) 5891.
- [35] Wilson, M. R., *Molecular Physics* **81** (1994) 675.

- [36] Bladon, P. and Frenkel, D., *Journal of Physics: Condensed Matter* **8** (1996) 9445.
- [37] Cinacchi, G. and De Gaetani, L., *Physical Review E* **77** (2008) 051705.
- [38] Naderi, S. and van der Schoot, P., *Physical Review E* **88** (2013) 032307.
- [39] Naderi, S. and van der Schoot, P., *The Journal of Chemical Physics* **141** (2014) 124901.
- [40] Egorov, S. A., Milchev, A., Virnau, P., and Binder, K., *Soft Matter* (2016) 4944.
- [41] Alvarez, L., Lettinga, M. P., and Grelet, E., *Physical Review Letters* **118** (2017) 178002.
- [42] Repula, A., Oshima Menegon, M., Wu, C., van der Schoot, P., and Grelet, E., *Physical Review Letters* **122** (2019) 128008.
- [43] Lee, J. H. et al., *ACS Nano* **11** (2017) 3632.
- [44] Pottage, M. J. et al., *Soft Matter* **10** (2014) 4902.
- [45] Sofos, M. et al., *Nature Materials* **8** (2008) 68.
- [46] Zhou, J. et al., *Journal of Applied Physics* **112** (2012) 064102.
- [47] Patti, A., El Masri, D., van Roij, R., and Dijkstra, M., *The Journal of Chemical Physics* **132** (2010) 224907.
- [48] Naderi, S. et al., *Physical Review Letters* **111** (2013) 037801.
- [49] Pouget, E., Grelet, E., and Lettinga, M. P., *Physical Review E* **84** (2011) 041704.
- [50] Plimpton, S., *Journal of Computational Physics* **117** (1995) 1.
- [51] Frenkel, D. and Smit, B., *Understanding Molecular Simulation*, Academic Press, San Diego, 2nd edition, 2002.
- [52] de Braaf, B., Oshima Menegon, M., Paquay, S., and van der Schoot, P., *The Journal of Chemical Physics* **147** (2017) 244901.
- [53] de Gennes, P. G. and Prost, J., *The Physics of Liquid Crystals*, Oxford University Press, 1995.
- [54] Polson, J. M. and Frenkel, D., *Physical Review E* **56** (1997) 6260.

- [55] Nelson, D. R. and Halperin, B. I., *Physical Review B* **19** (1979) 2457.
- [56] Schneider, T. and Stoll, E., *Phys. Rev. B* **17** (1978) 1302.
- [57] Hansen, J. P. and McDonald, I., *Theory of Simple Liquids*, Elsevier, 1990.
- [58] Lettinga, M. P. and Grelet, E., *Phys. Rev. Lett.* **99** (2007) 197802.
- [59] Zanchetta, G., *Liquid Crystals Today* **18** (2009) 40.
- [60] Nakata, M. et al., *Science* **318** (2007) 1276.
- [61] Lagerwall, J. P. F. and Scalia, G., *Journal of Materials Chemistry* **18** (2008) 2890.
- [62] Khokhlov, A. R. and Semenov, A. N., *Physica A: Statistical Mechanics and its Applications* **108** (1981) 546.
- [63] Khokhlov, A. R. and Semenov, A. N., *Physica A: Statistical Mechanics and its Applications* **112** (1982) 605.
- [64] Selinger, J. V. and Bruinsma, R. F., *Physical Review A* **43** (1991) 2910.
- [65] Selinger, J. V. and Bruinsma, R. F., *Physical Review A* **43** (1991) 2922.
- [66] Tkachenko, A. V., *Physical Review Letters* **77** (1996) 4218.
- [67] Vroege, G. J. and Lekkerkerker, H. N. W., *Reports on Progress in Physics* **55** (1992) 1241.
- [68] McGrother, S. C., Williamson, D. C., and Jackson, G., *The Journal of Physical Chemistry* **104** (1996) 6755.
- [69] van Roij, R., Bolhuis, P., Mulder, B., and Frenkel, D., *Physical Review E* **52** (1995) R1277.
- [70] Oyarzún, B., van Westen, T., and Vlugt, T. J. H., *The Journal of Chemical Physics* **138** (2013) 204905.
- [71] Qi, W.-K., Qin, S.-M., Zhao, X.-Y., and Chen, Y., *Journal of Physics: Condensed Matter* **20** (2008) 245102.
- [72] Wensink, H. H., *The Journal of Chemical Physics* **126** (2007) 194901.
- [73] Petukhov, A. V., Tuinier, R., and Vroege, G. J., *Current Opinion in Colloid & Interface Science* **30** (2017) 54 .

- [74] Gao, Y., Romano, F., Dullens, R. P. A., Doye, J. K., and Aarts, D. G. A. L., *Physical Review Materials* **2** (2018) 015601.
- [75] Benguigui, L. and Hardouin, F., *Journal de Physique Lettres* **42** (1981) 381.
- [76] Lagerwall, S., *Ferroelectric and Antiferroelectric Liquid Crystals*, Wiley, 2008.
- [77] Sear, R. P. and Jackson, G., *Physical Review E* **52** (1995) 3881.
- [78] Milchev, A., Nikoubashman, A., and Binder, K., *Computational Materials Science* **166** (2019) 230 .
- [79] Salamonczyk, M. et al., *Nature Communications* **7** (2016) 13358.
- [80] Pashley, R. M. and Karaman, M. E., *Applied colloid and surface chemistry*, J. Wileys, 2004.
- [81] Henderson, D., *Fundamentals of inhomogeneous fluids*, Marcel Dekker, 1992.
- [82] Repula, A. and Grelet, E., *Physical Review Letters* **121** (2018) 097801.
- [83] Maier, W. and Saupe, A., *Zeitschrift für Naturforschung A* **14** (1959) 882.
- [84] McMillan, W. L., *Physical Review A* **4** (1971) 1238.
- [85] Bier, M., van Roij, R., Dijkstra, M., and van der Schoot, P., *Phys. Rev. Lett.* **101** (2008) 215901.
- [86] Cinacchi, G. and De Gaetani, L., *Physical Review E* **79** (2009) 011706.
- [87] Sato, T. and Teramoto, A., Concentrated solutions of liquid-crystalline polymers, in *Biopolymers Liquid Crystalline Polymers Phase Emulsion*, volume 126 of *Advances in Polymer Science*, pages 85–161, Springer, 1996.
- [88] Doi, M. and Edwards, S., *The Theory of Polymer Dynamics*, Comparative Pathobiology - Studies in the Postmodern Theory of Education, Clarendon Press, 1988.
- [89] Fakhri, N., Mackintosh, F. C., Lounis, B., Cognet, L., and Pasquali, M., *Science* **330** (2010) 1804.
- [90] Kaes, J. et al., *Biophysical Journal* **70** (1996) 609.
- [91] Kyrylyuk, A. V. and van der Schoot, P., *PNAS* **105** (2008) 8221.

- [92] Park, S., An, J., Suk, J. W., and Ruoff, R. S., *Small* **6** (2010) 210.
- [93] Grossiord, N., Hermant, M., and Koning, C., *Polymer carbon nanotube composites: the polymer latex concept*, Pan Stanford Publishing, 2012.
- [94] Torquato, S., *Random Heterogeneous Materials: Microstructure and Macroscopic Properties*, Springer, 2005.
- [95] Stankovich, S. et al., *Nature* **442** (2006) 282.
- [96] Otten, R. H. J. and van der Schoot, P., *The Journal of Chemical Physics* **134** (2011) 094902.
- [97] Grossiord, N. et al., *Polymer* **49** (2008) 2866.
- [98] Moradi, M. et al., *Langmuir* **31** (2015) 11982.
- [99] Chatterjee, A. P., *Journal of Physics: Condensed Matter* **20** (2008) 255250.
- [100] Otten, R. H. J. and van der Schoot, P., *Physical Review Letters* **103** (2009) 225704.
- [101] Nigro, B., Ambrosetti, G., Grimaldi, C., Maeder, T., and Ryser, P., *Physical Review B* **83** (2011) 064203.
- [102] Schilling, T. et al., *The European Physical Journal Special Topics* **222** (2013) 3039.
- [103] Alig, I., Skipa, T., Lellinger, D., and Potschke, P., *Polymer* **49** (2008) 3524 .
- [104] Saphiannikova, M., Skipa, T., Lellinger, D., Alig, I., and Heinrich, G., *Express Polymer Letters* **6** (2012) 438.
- [105] Otten, R. H. J. and van der Schoot, P., *Physical Review Letters* **108** (2012) 088301.
- [106] Chatterjee, A. P., *The Journal of Chemical Physics* **140** (2014) 204911.
- [107] Finner, S. P., Kotsev, M. I., Miller, M. A., and van der Schoot, P., *The Journal of Chemical Physics* **148** (2018) 034903.
- [108] Eken, A. E., Tozzi, E. J., Klingenberg, D. J., and Bauhofer, W., *Journal of Applied Physics* **109** (2011) 084342.
- [109] Kwon, G., Heo, Y., Shin, K., and June Sung, B., *Physical Review E* **85** (2012) 011143.

- [110] Dhont, J. K. G. and Briels, W. J., *The Journal of Chemical Physics* **118** (2003) 1466.
- [111] Doi, M., Shimada, T., and Okano, K., *The Journal of Chemical Physics* **88** (1988) 4070.
- [112] Filion, L., Hermes, M., Ni, R., and Dijkstra, M., *The Journal of Chemical Physics* **133** (2010) 244115.
- [113] Lu, P. J. and Weitz, D. A., *Annual Review of Condensed Matter Physics* **4** (2013) 217.
- [114] Stauffer, D. and Aharony, A., *Introduction to percolation theory*, Taylor and Francis, 2nd edition, 1992.
- [115] Miller, M. A., *The Journal of Chemical Physics* **131** (2009) 066101.
- [116] Škvor, J. c. v., Nezbeda, I., Brovchenko, I., and Oleinikova, A., *Physical Review Letters* **99** (2007) 127801.
- [117] Babu, S., Rotterreau, M., Nicolai, T., Gimel, J. C., and Durand, D., *The European Physical Journal E* **19** (2006) 203.
- [118] Stauffer, D., *Physics Reports (Review Section of Physics Letters)* **54** (1979) 1.

Acknowledgments

This thesis is the result of work carried out in the Eindhoven University of Technology, within the group of Polymers and Soft Matter (TPS). The research presented in the thesis is part of a project from the Marie Skłodowska-Curie Innovative Training Network named DiStruc. It was a great opportunity to meet and work with members of these two groups. I thank them all for the interesting meetings and friendly atmosphere. Some of them were directly involved in the research presented here. I thank Bart de Braaf, Stefan Paquay, and Guido Kusters, from TPS, and Andrii Repula and Eric Grelet, from DiStruc, for the collaboration in articles that are the foundation of this thesis. More importantly, I thank my supervisor Paul van der Schoot for his guidance and support throughout my PhD.

Curriculum Vitae

Mariana Oshima Menegon

12 March 1988, São Paulo, Brazil

Education

2015-2019 PhD in Physics

Technische Universiteit Eindhoven, Eindhoven, the Netherlands
Project: Computer simulations of the structure and dynamics of elongated colloidal particles
Supervisor: Paul van der Schoot

2014-2015 Research internship

(6 months) Technische Universiteit Eindhoven, Eindhoven, the Netherlands
Project: Numerical modeling of actin polymeric networks
Supervisor: Cornelis Storm

2013-2015 Master in Physics

Universidade de São Paulo, São Paulo, Brazil
Project: Rheological characterization of actin polymeric networks - measurement and numerical modeling
Supervisor: Adriano Mesquita Alencar

2014-2015 Research internship

(2 months) Università degli Studi di Catania and Istituto Nazionale di Fisica Nucleare, Catania, Italy
Project: Ions detection and the detection system of MAGNEX
Supervisor: Angelo Cunsolo

2006-2009 Bachelor in Physics

Universidade de São Paulo, São Paulo, Brazil
Project: Enlarging the resources of the magnetic spectrograph - analogical and digital treatment of the new position sensitive detectors and applications
Supervisor: Thereza Borello-Lewin

Publication list

Published

- 2019 Self-organization of tip-functionalized elongated colloidal particles**
Mariana Oshima Menegon, Guido Kusters, and Paul van der Schoot
Physical Review E, 100, 042702
- 2019 Directing liquid crystalline self-organization of rodlike particles through tunable attractive single tips**
Andrii Repula, Mariana Oshima Menegon, Cheng Wu, Paul van der Schoot, and Eric Grelet
Physical Review Letters, 122, 128008
- 2017 Self-organisation of semi-flexible rod-like particles**
Bart de Braaf, Mariana Oshima Menegon, Stefan Paquay, and Paul van der Schoot
Journal of Chemical Physics, 147, 244901

In preparation

- 2019 Effect of flexibility on the dynamics of elongated guest particles in the smectic A phase**
Mariana Oshima Menegon and Paul van der Schoot
- 2019 Dynamics of clusters and percolation in fluid dispersions of spherical colloids**
Mariana Oshima Menegon, Shari Finner, and Paul van der Schoot

